Electrochemical Modification & Photoelectronic Properties of Carbon Nanotubes

THÈSE N° 3201 (2005)
PRÉSENTÉE A LA FACULTE SCIENCES DE BASE
Institut de physique des nanostructures
SECTION DE PHYSIQUE
ÉCOLE POLYTECHNIQUE FÉDÉRALE DE LAUSANNE

POUR L'OBTENTION DU GRADE DE DOCTEUR ÈS SCIENCES

PAR

Kannan Balasubramanian

M. Sc. / Diplom Ingenieur, Universität Gesamthochschule Kassel, Allemagne
et de nationalité indienne

acceptée sur proposition du jury:

Prof. K. Kern, directeur de thèse
Dr. M. Burghard, rapporteur
Prof. L. Forró, rapporteur
Prof. L. Schlapbach, rapporteur

Lausanne, EPFL

2005

Abstract

This thesis reports on the investigations performed on electrochemical functionalization and photoelectronic transport properties of individual single-wall carbon nanotubes (SWCNTs).

The first part of the thesis is concerned with the controlled modification of individual nanotubes through electrochemistry. The electrochemical modification has been performed using reductive and oxidative coupling schemes, resulting in thin molecular coatings around the SWCNTs. The former scheme is based on a reactive diazonium salt, while the latter involved a substituted aromatic amine. The characterization methods included electrical transport measurements and confocal Raman spectroscopy, both of which can address selected single SWCNTs or bundles. These studies were performed separately on metallic and semiconducting nanotubes, in both cases comparing the effect of the oxidative and reductive coupling schemes. While the oxidative scheme was found to yield non-covalently attached layers on the nanotubes, the reductive modification led to covalently grafted phenyl groups.

The reductive coupling scheme was utilized to address a fundamental problem in the creation of nanotube field-effect transistors (FETs). The fabrication of FETs using carbon nanotubes has been impeded as all current production procedures yield a mixture of metallic and semiconducting tubes. In this work, a generic approach employing electrochemistry for selective covalent modification of metallic nanotubes was devised, resulting in exclusive electrical transport through the unmodified semiconducting tubes. Towards this goal, the semiconducting tubes were rendered non-conductive by application of an appropriate gate voltage prior to the electrochemical modification. The FETs fabricated in this manner were found to display favourable hole mobilities and a high ratio approaching 10^6 between the current in the *ON* and *OFF* state.

The second part of the thesis deals with electronic transport through individual carbon nanotubes under local photo–illumination. The source of excitation was a diffraction–limited laser spot (diameter $\approx \lambda_{\text{exc}}/2$) generated by a confocal scanning optical microscope. Using this setup, photoconductivity in individual semiconducting

SWCNTs was investigated in detail. The magnitude of the photocurrent was found to increase linearly with the laser intensity, and was maximum for parallel orientation between the light polarization and the tube axis. Larger currents were obtained upon illuminating the tubes at 514.5 nm in comparison to those at 647.1 nm, consistent with the investigated semiconducting tubes having a resonant absorption energy at the former wavelength.

Furthermore, due to the relatively small diameter of the laser spot, the photoresponse could be measured as a function of position, which allowed the acquisition of photoelectronic transport (PET) images of individual nanotubes. During the course of this work, the PET imaging technique was developed into a useful tool to monitor local electronic structure effects, including the observation of Schottky barriers at the contacts with semiconducting SWCNTs. Subsequently, metallic SWCNTs were investigated by recording PET images. The locally induced photocurrents directly reflect the existence of built-in electric fields associated with the presence of depletion layers at the contacts or structural defects along the tubes. These observations have strong implications on the realisation of high-performance electrical devices incorporating carbon nanotubes, which critically depends on the minimisation of charge transport barriers along the tubes and at the contacts.

Résumé

Cette thèse rapporte les investigations effectuées sur la fonctionnalisation électrochimique et les propriétés de transport photoélectrique de nanotubes de carbone individuels à mono-parois (SWCNTs).

La première partie de la thèse traite la modification contrôlée de nanotubes individuels par l'électrochimie. La modification électrochimique a été effectuée en utilisant des réactions de couplage par réduction et par oxydation, donnant lieu à une fine couche moléculaire autour des SWCNTs. La réaction de réduction est faite à partir d'un sel réactif de diazonium, tandis qu'une amine aromatique substituée est utilisée pour la réaction d'oxydation. Les méthodes de caractérisation ont inclu des mesures de transport électriques et de spectroscopie confocale de Raman. Dans les deux cas, il a été possible de choisir d'effectuer sélectivement les mesures sur un unique ou bien un paquet de SWCNTs. Ces études ont été réalisées séparément sur des nanotubes métalliques et semi-conducteurs en comparant l'effet des réactions de couplage par oxydation et par réduction. Tandis que la réaction d'oxydation a créé des couches attachées de manière non covalentes aux nanotubes, la modification par réduction a mené à des groupes phényles liés de façon covalente aux nanotubes.

La réaction de couplage par réduction a été utilisée pour résoudre un problème fondamental dans la création des transistors à effet de champ basé sur les nanotubes (FETs). La fabrication des FETs à partir de nanotubes de carbone s'est heurtée au fait des procédures courantes de production qui donnent lieu exclusivement à un mélange de tubes métalliques et semi-conducteurs. Dans ce travail, une approche générique utilisant l'électrochimie a été conçue pour modifier par oxydation de façon sélective les seuls nanotubes métalliques, ayant pour résultat le transport électrique exclusif par les tubes semi-conducteurs non modifiés. Pour cette réalisation, les tubes semi-conducteurs ont été rendus non-conducteurs par l'application d'une tension gate appropriée avant la modification électrochimique. Les FETs ainsi fabriqués ont montré des mobilités de trou favorables et un rapport élevé approchant 10^6 entre le courant dans l'état de marche et le courant dans l'état d'arrêt.

La deuxiéme partie de la thèse traite le transport électrique par des nanotubes individuels de carbone sous l'effet d'une photo-illumination locale. La source d'excitation fût un faisceau laser à diffraction limitée (diamètre $\approx \lambda_{\text{exc}}/2$) produite par un microscope optique confocal à balayage. En utilisant cette installation, la photoconductivité de SWCNTs semi-conducteurs individuels a été étudiée en détail. L'importance du courant photoélectrique montre une augmentation linéaire avec l'intensité du laser, et devient maximale pour une orientation parallèle entre la polarisation de la lumière et l'axe du tube. De plus grands courants ont été obtenus lorsque les tubes ont été illuminé par une lumière de 514,5 nm de longueur d'onde au lieu de 647,1 nm. Ce résultat est cohérent avec l'énergie résonnante d'absorption à 514,5 nm de longueur d'onde des tubes semi-conducteurs étudiés.

En outre, en raison du diamètre relativement petit du faisceau laser, la réponse photoélectrique peut être mesurée en fonction de la position du faisceau sur le tube, ce qui a permis l'obtention d'images du transport photoélectrique (PET) de nanotubes individuels. Au cours de ce travail, la technique images PET a été développée afin de pouvoir surveiller les effets de structure électronique locale, y compris l'observation de barrières de Schottky au niveau des contacts avec les SWCNTs semi-conducteurs. Par la suite, les images PET des SWCNTs métalliques ont été étudiées avec la même technique. Les courants photoélectriques localement induits reflètent directement la pré-existence de champs électriques liés à la présence de région à densité de charge plus faible au niveau des contacts ainsi qu'à l'effet des défauts structuraux le long des tubes. Ces observations ont d'importantes implications pour la réalisation de dispositifs électriques à rendement élevé incorporant des nanotubes de carbone puisqu'un élément essentiel à leur réalisation est la minimisation des barrières de transport de charge le long des tubes et au niveau des contacts.

Contents

Chapter 1

Introduction

Since the days of the earliest known human civilization, mankind is motivated with a continuous drive for development. First came the invention of the wheel, followed by the ability to use metals and going through a series of Ages there came the Industrial Revolution in the 18th century A.D. This was ensued by the semiconductor era in the 20th century with the invention of the transistor and integrated circuits. This series of developments has brought in comfort and luxury that one could not have imagined of at the dawn of civilization. Apart from these technological developments, one tends to forget the progress that has been made in the development of basic services to humanity. This concerns the advances in medicine that has occured since the Stone Age. We have come a long way from using herbs available in the jungle to drugs that are specifically designed for a particular purpose. The technological advances have always walked hand-in-hand with medicinal research to achieve capabilities as complex as transplanting a heart of one person by that of another.

The human urge to continue along this trend has led to the emergence of a new field towards the end of the last century, namely nanotechnology. This involves – among other objectives – bringing the technological advances one step further by reducing the size of electronic devices by around three orders of magnitude. Carbon Nanotubes (CNTs) are an important element in this rapidly emerging field due to their miniscule diameters of a few nm combined with their promise to function as efficient components of electronic devices. Apart from use in nano-scale devices, due to their biocompatibility arising from their carbonaceous nature, they are being considered for drug delivery and for basic research in medicine. Thus they possess the unique aspect of the ability to merge technological advances with medicinal applications and hence have become one of the most intensively investigated materials. This is reflected, for instance, by the continuously increasing number of publications, which exceeded three thousand in the year 2003 [1].

CNTs can be visualized as being composed of concentric cylinders of a single atomic layer of graphite (graphene sheet). They are classified as single-wall CNTs (SWCNTs) comprising of just a single shell and multi-wall CNTs (MWCNTs) comprising of at least two shells of the graphene layer. The work in this thesis focusses only on SWCNTs. The extraordinary interest in the study of SWCNTs stems from their outstanding structural, mechanical and electronic properties. SWCNTs are ideal candidates as 1D single molecule systems and are intriguing for fundamental studies. Mechanically they possess extraordinarily high tensile strength, which outreaches that of a steel wire of corresponding thickness by around one order of magnitude. This combined with their low density (one-sixth that of steel) makes them highly suited for composites. Electrically, they can be found as both metallic and semiconducting tubes. Due to their microscopic dimensions, they have become one of the most successful materials for the fabrication of molecular-scale electronic devices. These aspects make them highly valuable for applications in electronics, scanning probe microscopy, chemical and biological sensing, reinforced composite materials, and many more. While some of the proposed applications remain still a far-off dream, others are close to a technical realization.

Recent advances in the development of reliable methods for the chemical functionalization of nanotubes provide an additional impetus towards extending the scope of their application spectrum. Through appropriate modification schemes, the surface of the SWCNTs can be imparted with a desired functionality, such as high water solubility, good chemical sensitivity or large photoresponsiveness. Although such possibilities sound indeed promising, reports on controlled chemical modification of SWCNTs are only starting to appear. Due to their curvature introduced by their cylindrical nature, they are more reactive than graphite [2]. The chemical modification schemes that are being devised can be classified into three categories [3] namely thermally activated chemistry, electrochemical modification (ECM) and photochemistry. While thermally activated functionalization procedures have been demonstrated for the attachment of a variety of functional groups onto SWCNTs [4, 5], photochemical modification of SWCNTs is still in its infancy. Electrochemistry is an elegant approach that allows for an effective control over the extent and type of modification.

Work on chemical functionalization of SWCNTs has been until now mostly performed on bulk SWCNT material. However, for a detailed understanding of the mechanism of chemical modification and the resulting properties, molecular-scale studies at a single object level are essential. This thesis describes a first step in this direction, wherein individually addressable SWCNTs have been electrochemically modified and characterized. The characterization has been performed by electronic transport and confocal Raman spectroscopic measurements on the same individual SWCNTs before and after the electrochemical modification. These studies were undertaken separately for individual metallic and semiconducting SWCNTs.

The ECM approach has enabled a novel route to field-effect transistors (FETs). Pristine SWCNTs are themselves prospective components of nanoscale electronic devices [6]. For instance, FETs have been successfully fabricated from single semiconducting nanotubes [7,8]. The overall performance of SWCNT-FETs has been reported to be superior to that of state-of-the-art silicon based MOSFETs, as reflected in the values of the drive current and transconductance being higher by a factor of four [9]. Moreover, devices implementing CVD-grown SWCNTs have shown extremely high hole mobilities [10] of up to 9000 $\mathrm{cm}^2/\mathrm{Vs}$ at room–temperature. With palladium as the electrode material, Schottky barrier-free ballistic FETs [11] have recently been realized, exhibiting high drive currents, good transconductance and switching ratios of 10^6.

However, the use of SWCNTs in the electronics industry is largely limited due to the occurence of a mixture of both metallic and semiconducting SWCNTs. Solution-based techniques for separation of metallic SWCNTs (m-SWCNTs) from semiconducting ones (s-SWCNTs) do not provide a quantitative separation [12–15]. Another approach is based on the fabrication of the FET device with a mixture of m-SWCNTs and s-SWCNTs followed by selective burning of the m-SWCNTs through high voltage ramps [16]. The procedure developed in this thesis extends the scope of the latter technique by using the gate voltage to switch off the s-SWCNTs in an ensemble and selectively modify the m-SWCNTs in a covalent manner. Since the modified m-SWCNTs do not contribute to the transport due to their high resistance, this results in a purely semiconducting network that can function as an FET.

Apart from their exquisite electronic properties, the optical properties of SWCNTs have also attracted great attention. The direct band gap in semiconducting nanotubes combined with their one dimensional electronic structure opens up possibilities for their use as components of future nanoscale optoelectronic devices. The strong 1D confinement in SWCNTs should lead to large Coulombic coupling between photoexcited electrons (e) and holes (h) to create strongly bound excitons [17]. Correspondingly, the absorption intensity should be enhanced because of the increased e–h overlap. Application of a drain-source bias leads to a flow of the photoexcited carriers resulting in the generation of a photocurrent in s-SWCNTs. Photoinduced current modulation was first observed in nanotube films [18]. Illumination of ensembles of very small diameter nanotubes formed within a zeolite pores produced a slight polarization-dependent current enhancement [19]. Filaments of nanotube bundles between two electrodes showed current generation upon light illumination, which was attributed to either a thermoelectric or a photovoltaic effect [20]. Although these experiments indicated that ensembles of carbon nanotubes do respond electronically to light, it is highly desirable to understand this interaction in detail and on a single molecule basis. Using an infrared laser, photoconductivity from a single s-SWCNT incorporated as the channel of an ambipolar FET could be observed [21]. However, in this and all the other previous experiments, a laser spot with a diameter of at least a few μm was used for illumination of the whole sample to observe the photoelectronic effects. This does not allow the investigation of transport barriers at the contacts and other local inhomogeneities along the tube. This thesis describes the first experimental setup of its kind that combines a confocal laser scanning Raman microscope with electronic transport measurements to observe localized photoelectronic transport through individual SWCNTs.

The thesis is organized as follows. The second chapter gives an overview of the fundamental properties of carbon nanotubes. In the third chapter, the experimental techniques used in this work are outlined. Electrochemical modification of individual carbon nanotubes and its ensuing application towards fabrication of FETs is presented in the fourth chapter. Chapter 5 is devoted to the investigations performed on photoelectronic transport properties of individual metallic and semiconducting SWCNTs. The thesis finally ends with a conclusion including a summary of the important achievements attained in this work.

Chapter 2

Carbon Nanotubes: Fundamentals

Carbon nanotubes (CNTs) are cylinder-shaped macromolecules with radius as small as few nm, which can be grown up to 20 cm in length [22]. The walls of these tubes are made up of a hexagonal lattice of carbon atoms analogous to the atomic plane of graphite. They are capped at their ends by a half of a fullerene-like molecule. In the most general case, a CNT is composed of a concentric arrangement of many cylinders (see Fig. 2.1). Such multi-wall nanotubes (MWCNTs) can reach diameters of up to 100 nm. A special case of these multi-wall tubes is the double-wall CNT composed of just two concentric cylinders. Single-wall nanotubes (SWCNTs) possess the simplest geometry, and have been observed with diameters ranging from 0.4 nm to 3 nm.

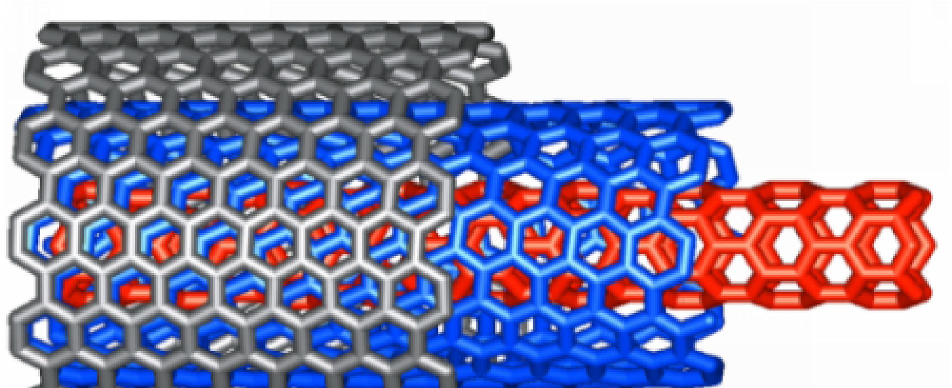

Figure 2.1: A model showing a multi-wall carbon nanotube composed of three shells of differing chirality.

2.1 Physical structure

The formation of a SWCNT can be visualized through the rolling of a graphene sheet. Based on the orientation of the tube axis with respect to the hexagonal lattice, the structure of a nanotube can be completely specified through its chiral vector $\overrightarrow{C_h}$ (see Fig. 2.2), which is given by

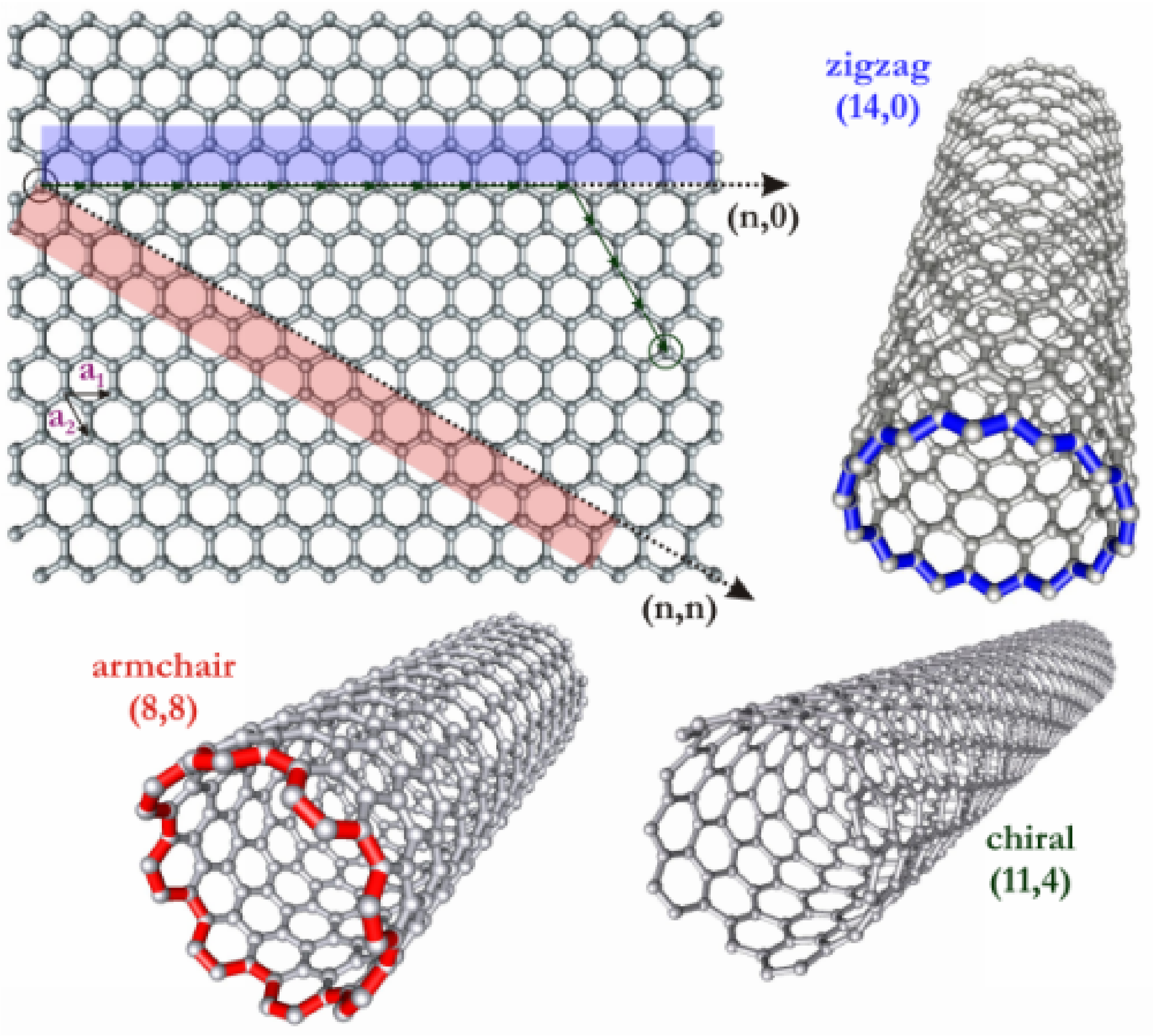

Figure 2.2: Physical structure of a carbon nanotube starting from a graphene sheet. Depending on the way the sheet is rolled-up, the nanotubes are classified into three types namely armchair, zigzag and chiral.

$$\overrightarrow{C_h} = n\overrightarrow{a_1} + m\overrightarrow{a_2} \qquad 0 \leq m \leq n \tag{2.1}$$

n and m are integer chiral indices used to specify a nanotube and $\overrightarrow{a_1}$ and $\overrightarrow{a_2}$ are the real space unit vectors of the hexagonal lattice of 2D graphite. The unit vectors are given by $\overrightarrow{a_1} = a\left(\frac{\sqrt{3}}{2}, \frac{1}{2}\right)$ and $\overrightarrow{a_2} = a\left(\frac{\sqrt{3}}{2}, -\frac{1}{2}\right)$. a is the lattice constant of 2D graphite, which is 2.46 Angstrom. The diameter of an (m, n) SWCNT is then given by $d = \left|\overrightarrow{C_h}\right| / \pi$.

The classification of the nanotubes as armchair $(n = m)$ or zigzag $(m = 0)$ has its origin from the geometric arrangement of the carbon atoms at the seam of the cylinders. While both these types of tubes possess mirror symmetry, nanotubes with $m \neq n$ are chiral. The latter kind of tubes exists as two enantiomers with right- and left-handed helicity. Historically the multi-wall nanotubes were the first to be discovered (1991) [23], followed by their single-wall [24, 25] counterparts (1993).

2.2 Electronic structure

Since the earliest stages of the emergence of carbon nanotubes, their electrical properties have attracted particular interest. The electronic properties of SWCNTs were first calculated using a tight-binding model by applying the zone-folding approach [6], which derives the electronic structure of nanotubes directly from that of graphite. In graphite, the electrons in the π-(valence) band and the π^*-(conduction) band are the ones that are relevant for the electronic transport and other solid state properties. Despite the simplicity of the tight-binding approach, it provides important insight into the electronic strucutre of the π- and π^*-bands of graphite.

To arrive at the electronic structure of carbon nanotubes, one starts with the energy dispersion relation for 2D graphite, which is given by [6]

$$E_g\left(k_x, k_y\right) = \pm t \left\{ 1 + 4 \cos\left(\frac{\sqrt{3} k_x a}{2}\right) \cos\left(\frac{k_y a}{2}\right) + 4 \cos^2\left(\frac{k_y a}{2}\right) \right\}^{1/2} \tag{2.2}$$

where k_x and k_y are the x and y components of the wave vector in the reciprocal lattice and t is the tight-binding transfer integral signifying the interaction between nearest neighbour carbon atoms. For the purpose of calulations t takes a value of -2.9 eV. However, from experiments that are used to measure the electronic structure, differing values around -3 eV have been found. The energy dispersion relations given by (2.2) are plotted in Fig. 2.3. The upper half of the energy dispersion curves in Fig. 2.3(a) describes the π^*-(conduction) bands while the lower half the π-(valence) band. The π^* and the π bands are degenerate at the K point through which the Fermi energy passes. The shaded hexagon corresponds to the first Brillouin zone. In Fig. 2.3(b) a color-coded projection of the dispersion relations is depicted, with the marked hexagon again describing the first Brillouin zone. The high symmetry points are marked by K, Γ and M.

The electronic structure of a SWCNT can now be directly obtained from that of

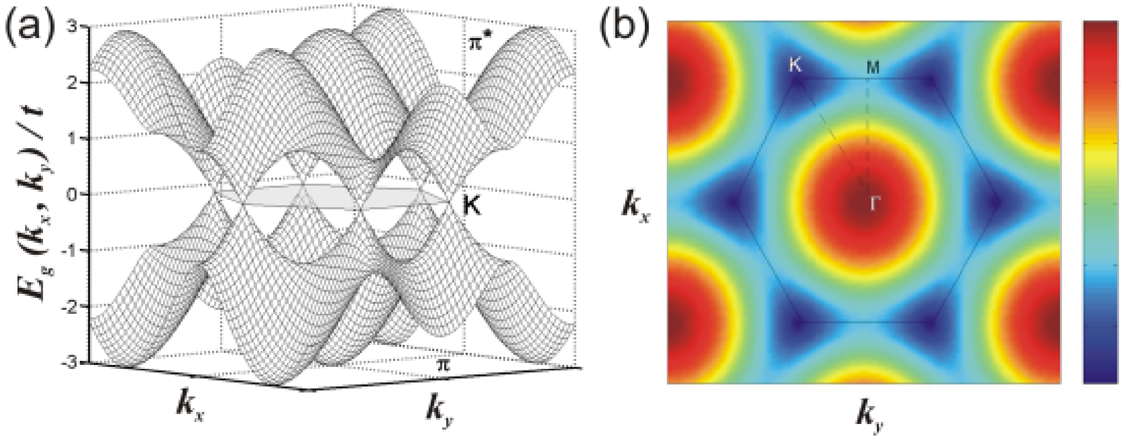

Figure 2.3: Dispersion relations for a 2D graphene sheet, obtained by the tight binding model: (a) 3D plot of the energy dispersion relations for 2D graphite given by (2.2). (b) Color-coded plot of the same function with blue regions having values close to minima and the red regions having values close to maxima. The vertices of the hexagon correspond to those points where the π and π^* bands are degenerate.

two-dimensional graphite. By using periodic boundary conditions along the circumferential direction denoted by the chiral vectior $\overrightarrow{C_h}$, the wave vector associated with the circumferential direction gets quantized, while the translational wave vector that runs along an infinitely long nanotube remains continuous. As a result of this, the energy bands consist of a set of one-dimensional energy dispersion relations, which are cross sections of those for 2D graphite. When performing this procedure, if one of the cutting lines passes through the K point of the 2D Brillouin zone, the one-dimensional energy bands will have a zero energy gap and the density of states at the Fermi level will be finite. Such nanotubes are metallic. Armchair tubes ($m = n$) and zigzag and chiral tubes with $m - n$ being a multiple of 3 belong to this category. On the other hand, if the intersecting lines does not pass through a K point, then the carbon nanotube is semiconducting with a finite energy gap between the valence and conduction bands. Zigzag and chiral tubes with $m-n$ not being a multiple of 3 are semiconducting [26,27].

Explicit expressions for the energy dispersion relations for SWCNTs can be obtained by imposing appropriate boundary conditions into the 2D dispersion relations of (2.2), depending on the type of tube under consideration. The relations for the armchair and zigzag tubes are the simplest to obtain in this manner. The one-dimensional energy dispersion relations for armchair SWCNTs with $\overrightarrow{C_h} = (n, n)$ is given by [28]

$$\begin{aligned} E_q(k) = \quad & \pm t \quad \left\{1 \pm 4\cos\left(\frac{q\pi}{n}\right)\cos\left(\frac{ka}{2}\right) + 4\cos^2\left(\frac{ka}{2}\right)\right\}^{1/2} \\ & \left(\frac{-\pi}{a} < k < \frac{\pi}{a}\right), (q = 1, \cdots, 2n) \end{aligned} \tag{2.3}$$

Thus all armchair tubes possess $4n$ energy subbands with $2n$ conduction and $2n$ valence bands and of the $2n$ bands, two are nondegenerate and $(n-1)$ are doubly degenerate. In a similar manner, the energy dispersion relations for zigzag nanotubes with $\overrightarrow{C_h} = (n, 0)$ have been derived as [28]

$$E_q(k) = \pm \quad t \quad \left\{ 1 \pm 4\cos\left(\frac{q\pi}{n}\right)\cos\left(\frac{\sqrt{3}ka}{2}\right) + 4\cos^2\left(\frac{q\pi}{n}\right) \right\}^{1/2}$$
$$\left(\frac{-\pi}{\sqrt{3}a} < k < \frac{\pi}{\sqrt{3}a}\right), (q = 1, \cdots, 2n) \tag{2.4}$$

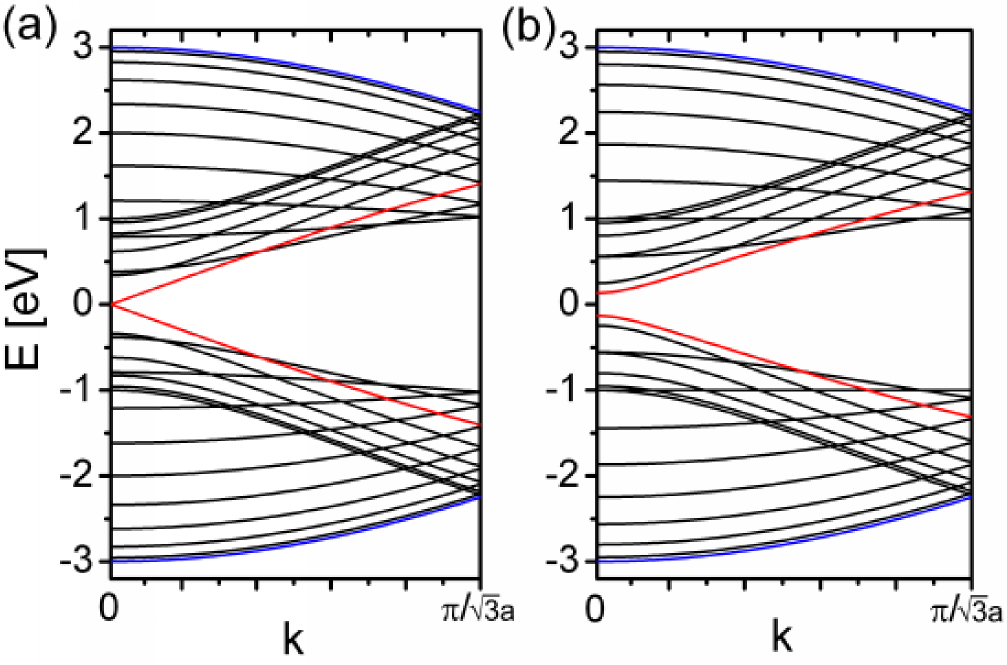

Figure 2.4: Calculated energy dispersion relations for SWCNTs: (a) (15,0) metallic SWCNT. (b) (14,0) semiconducting SWCNT.

Figures 2.4(a) and (b) show respectively the energy dispersion relations for a (15,0) SWCNT and a (14,0) SWCNT. There is no energy gap at $k = 0$ for the (15,0) metallic nanotube, while the (14,0) semiconducting SWCNT shows an energy gap. The (14,0) SWCNT has a diameter of ≈1.1 nm and the (15,0) tube 1.3 nm. Thus both these tubes are representative of a sample from the arc discharge process.

Obtaining the electronic density of states (EDOS) from the dispersion relations is rather straightforward. For this purpose, the inverse slopes of the energy dispersion curves are integrated at each energy point [29]. The resulting EDOS for the (14,0) and (15,0) SWCNT is shown in Fig. 2.5. The metallic (15,0) nanotube exhibits two bands at the Fermi energy. The semiconducting (14,0) nanotube has zero density of states at the Fermi level with a band gap of around 0.7 eV. For both tubes, the EDOS exhibits

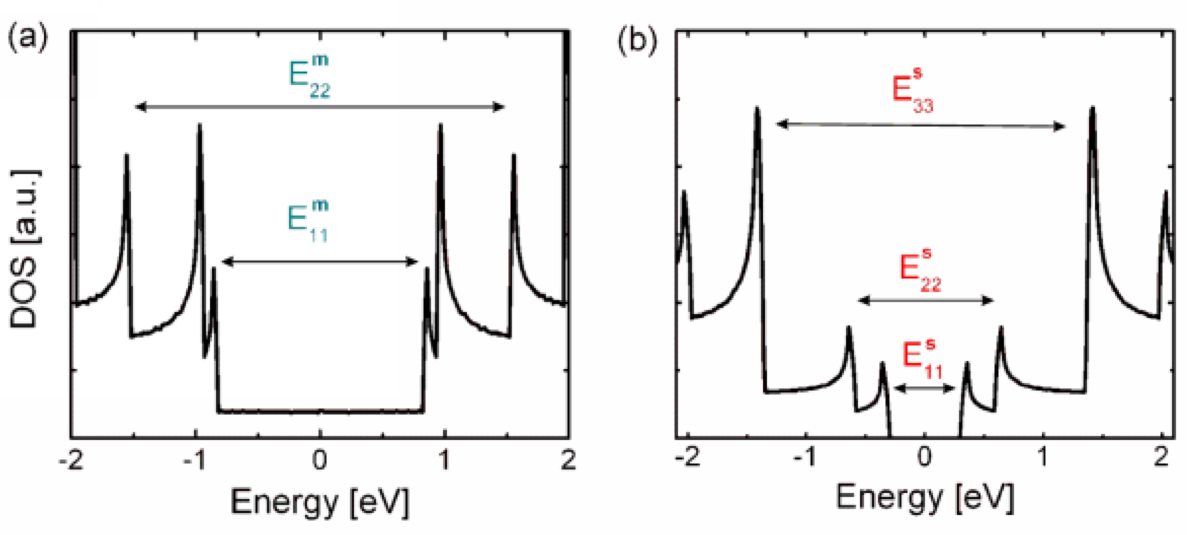

Figure 2.5: Calculated Electronic Density of States (EDOS) of Carbon Nanotubes: (a) EDOS of a (15,0) metallic SWCNT. (b) EDOS of a (14,0) semiconducting SWCNT.

pronounced peaks at certain energy levels, which is characteristic of their quasi-1D structure. These peaks are referred to as van Hove singularities. Various material properties such as optical absorption, optical emission, electronic transport etc. are closely related to the spacing between these van Hove singularities. The series of relatively sharp interband transitions each of them comprising the energy difference between a pair of van Hove singularities is represented by E^x_{ii} as shown in Fig. 2.5, where i denotes the number of EDOS peak starting from the Fermi energy and x is either 'm' or 's' for m-SWCNTs or s-SWCNTs respectively. It is noteworthy that in Fig. 2.5(a) the E^m_{11} for the (15,0) tube is found to undergo a splitting due to the trigonal warping effect [30].

The one-dimensional nature of SWCNTs confine the electrons to move only along two directions of the tube axis – namely, forward and backward. Accordingly, the requirements for energy and momentum conservation leads to a reduced "phase-space" for scattering processes that are responsible for the electrical resistance of SWCNTs [31]. Because of the reduced scattering, m-SWCNTs can carry high current densities of up to 10^9 A/cm^2 without being burnt-off [32]. This density is about 2-3 orders of magnitude higher than what is possible in metals such as Al or Cu.

2.3 Optical absorption and photoluminescence

The detailed study of the optical properties of SWCNTs has been mainly impeded by the bundling of the tubes. In initial experiments, it was observed that the absorption spectrum in the near infrared and visible wavelengths was composed generally of three peaks corresponding to the interband transitions between the first van Hove singularities [33]. The peaks were broadened because of a broad distribution of diameters present in the bundles. No photoluminescence could be observed in such samples due to the fact that the luminescence efficiency is greatly reduced due to quenching by metallic tubes. Debundling of the tube bundles could be achieved by ultrasonication in a surfactant solution followed by centrifugation [34]. This resulted in the formation of micelles around individual nanotubes preventing them to rebundle. The micelle-suspended nanotube solutions had richly structured absorption spectra and exhbited measurable photoluminescence. An example of such an absorption spectrum in the UV/Vis–IR range is depicted in Fig. 2.6. The series of peaks originate from the superposition of distinct electronic transitions from a variety of different SWCNTs isolated within the micelles. The three broad peaks which were initially observed in samples containing bundles can now be better resolved and the positions of the peaks agree with the expectation that the first van Hove transitions of s-SWCNTs fall in the range of 0.78 to 1.55 eV, slightly overlapping with their second van Hove transitions in the range of 1.38 to 2.25 eV. The lowest energy of van Hove transitions for m-SWCNTs appear between 2.10 eV and 3.10 eV [30]. Upon excitation of such a solution with a laser of wavelength 532 nm, bright photoluminescence could be observed in the near-infrared associated with radiative recombination over the band gap of isolated s-SWCNTs [34].

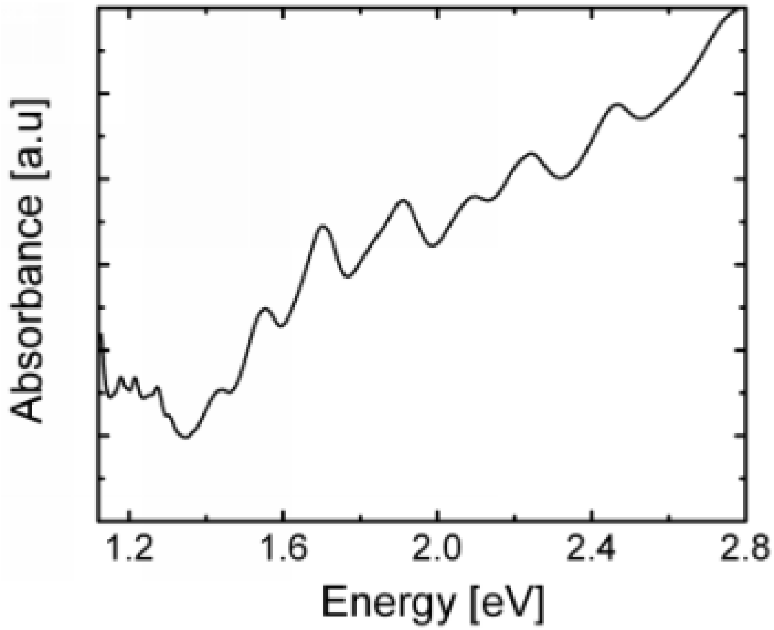

Figure 2.6: Absorption spectrum of micelle-suspended HiPco SWCNTs in an aqueous sodium dodecyl sulphate solution. Sharp absorption peaks can be identified indicative of individually suspended SWCNTs in solution.

2.4 Phonon structure

2.4.1 Resonant Raman scattering

The main technique for probing the phonon spectra has been Raman spectroscopy. Raman spectroscopy is a powerful tool that provides insight into the physical properties as well as the material quality of an investigated system. A first order Raman scattering process involves the absorption of an incoming photon with a certain frequency ω_{exc} that generates an electron-hole pair, which then scatters inelastically under the creation or annihilation of a phonon (of frequency ω_{ph}). The scattered photon has a frequency ω_{sca} different from that of the incident photon. Energy and momentum are conserved in a Raman process with $\hbar\omega_{\mathrm{exc}} = \hbar\omega_{\mathrm{sca}} \pm \hbar\omega_{\mathrm{ph}}$. The $\pm$ signs refer to Stokes (phonon creation) and anti-Stokes (phonon annihilation) scattering. In a typical Raman experiment, the sample is irradiated with a laser source of a certain wavelength λ_{exc} and the scattered light is recorded over a range of wavelengths very close to λ_{exc}. If λ_{exc} is such that the incident photon energy is close to any transition energy, then resonant Raman scattering occurs. In the case of SWCNTs, sharp van Hove maxima exist at certain energies. Thus when they are excited by a laser wavelength with an energy close to their transition energies, Raman scattering is remarkably enhanced [35].

The Kataura plot [36] can be used to illustrate the principle of resonant Raman scattering in SWCNTs from the arc discharge and HiPco processes. The plot shows the distribution of allowed transition energies E_{ii}^{x} for SWCNTs in a range of diameters as displayed in Fig. 2.7. For the purpose of excitation of the SWCNTs, laser radiation in the visible region is utilized. The common wavelengths available with an Argon-Krypton laser that were used in this work are the green (λ_{exc} = 514.5 nm) and red (λ_{exc} = 647.1 nm) lines corresponding to energies of 2.41 eV and 1.92 eV respectively, marked appropriately in the figure. The diameter range of the arc discharge and HiPco SWCNTs are also marked as rectangles in the figure. It can be observed from the figure that within the range of arc-discharge tubes (1.1–1.4 nm) a laser excitation using the green line would excite exclusively the s-SWCNTs and the red line only the m-SWCNTs. On the other hand, for samples fabricated using HiPco tubes, the red line would excite only the s-SWCNTs and the green line the m-SWCNTs.

2.4.2 Phonon modes and Raman spectra

The phonon dispersion relations in SWCNTs can be obtained from those of the 2D graphene sheet by using the same zone folding approach as used to derive the 1D elec-

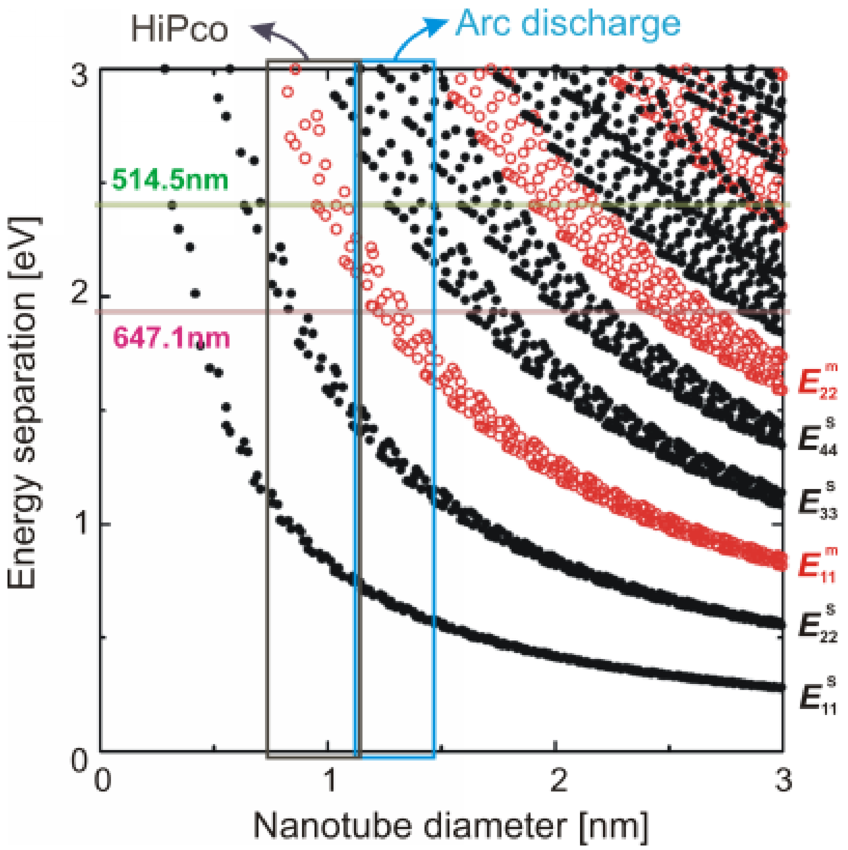

Figure 2.7: Calculated energy separations E_{ii}^{x} as a function of nanotube diameter between 0.7 and 3 nm(Kataura plot). The red circles refer to m-SWCNTs and the black ones to s-SWCNTs. The laser wavelengths used in this work are marked by the red and green lines corresponding to $\lambda_{\text{exc}} = 647.1$ nm and $\lambda_{\text{exc}} = 514.5$ nm respectively. The diameter range of the arc discharge SWCNTs is represented using a blue rectangle while that of HiPco SWCNTs using a brown rectangle.

tronic dispersion relations [35]. The phonon dispersion relations for SWCNTs depend on the indices (n, m), since the phonon wave vector in the circumferential direction becomes discrete in accordance with the periodic boundary conditions of the chiral vector $\overrightarrow{C_h}$. The number of hexagons N in a unit cell of an (m, n) SWCNT is $N = 2\left(m^2 + n^2 + nm\right)/d$. Since there are $2N$ carbon atoms in the unit cell, each of them with three degrees of freedom, the phonon dispersion relations consist of $6N$ branches. For example, a $(10, 10)$ SWCNT has 40 carbon atoms in the unit cell and correspondingly 120 vibrational degrees of freedom. But because of mode degeneracies there are only 66 distinct phonon branches, of which 12 are non-degenerate and 54 are doubly degenerate.

Although the zone folding approach can compute the phonon branches of SWCNTs that are similar to that of the graphene sheet, new modes occuring due to the curvature of the nanotube are not predicted. For this, one has to introduce additional physical concepts or use ab initio calculations. For example, the out-of-plane tangential acoustic mode of a graphene sheet shown in Fig. 2.8(a) gives rise to the radial breathing mode (RBM) in nanotubes and the resulting vibration does not have $\omega \rightarrow 0$ as $k \rightarrow 0$. Hence, the RBM is not an acoustic mode, but rather an optical mode with a non-zero frequency at $k = 0$. In addition, in a graphene sheet, the in-plane and out-of-plane modes are decoupled from each other. However, when the graphene sheet is rolled up into a nanotube, the graphite-derived in-plane and out-of-plane modes do couple to each other to form the acoustic mode of the nanotube as shown in Fig. 2.8(b).

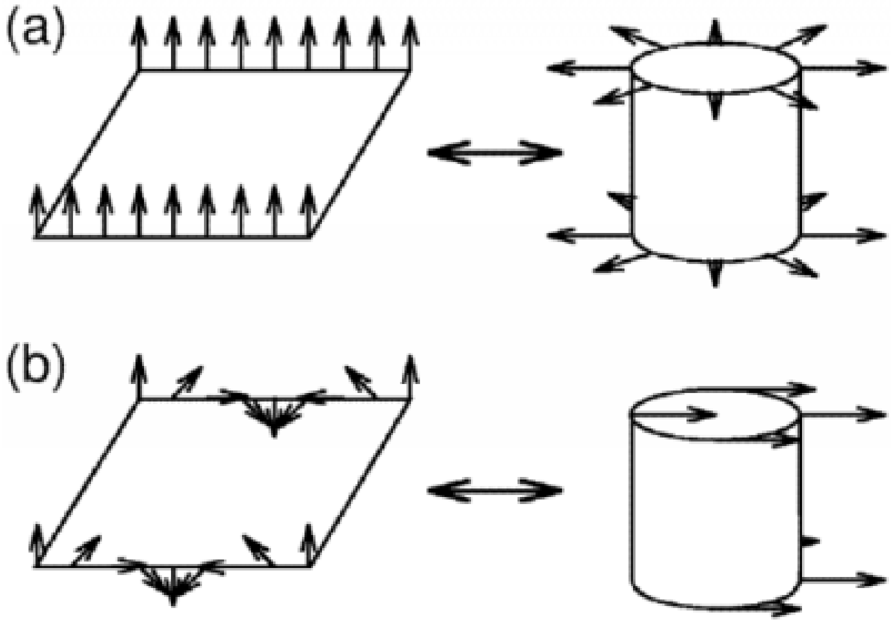

Figure 2.8: (a) The out-of-plane tangential mode in a graphene sheet gives rise to the radial breathing mode (RBM) in a SWCNT. (b) The in-plane and out-of-plane modes do not couple in a graphene sheet while they indeed do upon rolling up of the sheet giving rise to a vibrational mode perpendicular to the tube axis.

The special symmetry properties of 1D SWCNTs results in only a few of the $6N$ vibrational modes being Raman-active or infrared (IR)-active. Since only k vectors very close to $k = 0$ are coupled to the incident light because of the energy-momentum conservation requirements for the photons and phonons, only the modes close to the Γ point are relevant. The numbers of Raman-active and IR-active modes can be obtained by using group theory. Although group theory predicts the presence of 15 to 16 Raman-active modes, only a few of them have sufficient cross-section to be detectable through Raman spectroscopy. Among these, several modes close to 1600 cm^{-1} can be detected that arise due to tangential vibrations of the carbon atoms. Since this set of modes has its origin from the graphene sheet, they are referred to as the G-line in the Raman spectrum. Another high frequency mode that can be detected by Raman spectroscopy is the D-line occuring at about 1300 cm^{-1}, which is related to the amount of defects within the nanotubes that lower the crystal symmetry of the sp^2–bonded framework. The RBM is also a Raman-active mode and occurs in the low frequency regime of around 100 to 300 cm^{-1}. Apart from these a multitude of higher order modes can be identified in the Raman spectra at frequencies higher than 1600 cm^{-1} arising due to a combination of the RBM, D and G lines. A typical Raman spectrum from an individual bundle showing the various lines is presented in Fig. 2.9. Two RBM peaks, the D-line and G-line can be easily identified in the spectrum. The D-line is very weak indicative of the bundle being almost free of defects. Additionally, two higher order modes (marked by the asterisk signs) can be recognized. The experimental setup for obtaining such a spectrum from an individual SWCNT is detailed in the next chapter.

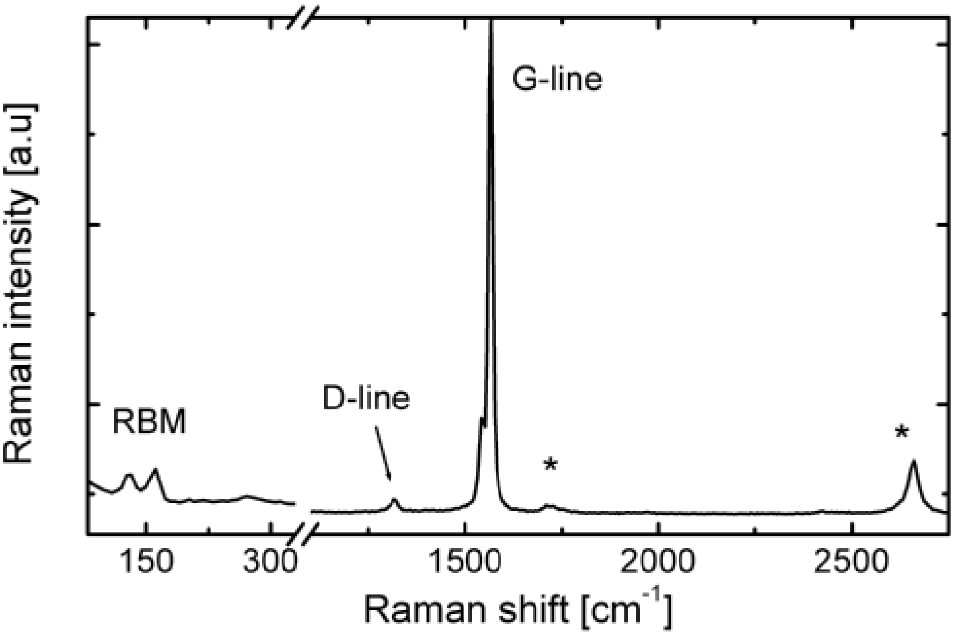

Figure 2.9: A typical Raman spectrum of a bundle of SWCNTs obtained with λ_{exc} = 514.5 nm. Two RBM peaks can be identified at ≈ 129 cm^{-1} and 163 cm^{-1}, in addition to the D-line at 1318 cm^{-1} and the G-line at 1566 cm^{-1}. There are two higher modes appearing in this tube bundle at 1717 cm^{-1} (attributed to RBM/G-line combination) and at 2655 cm^{-1} (second order D-line).

2.5 Chemically functionalized carbon nanotubes

On top of their excellent electrical and optical properties, nanotubes possess high mechanical and chemical stability. While the latter is certainly advantageous from an application point of view, at the same time it imposes a severe hurdle for the development of methods allowing for the selective and controlled functionalization of the nanotubes. This explains why it was only within the past 3-4 years that a wider range of reliable functionalization schemes became available. In this section, following a short discussion of the chemical nature of SWCNTs, different functionalization schemes are summarized. Specifically three different approaches have been undertaken for the chemical modification of SWCNTs namely thermally activated chemistry, electrochemical modification and photochemical functionalization.

2.5.1 Chemical nature of carbon nanotubes

Ideal SWCNTs possess two distinct regions of differing reactivity towards covalent chemical modification. The presence of 5-membered rings at the caps leads to a relatively higher reactivity there, which is comparable to that of fullerenes [37]. By comparison, functionalization of the sidewall comprising the regular graphene framework is more difficult to accomplish. In general, addition reactions to the partial carbon-carbon double bonds cause the transformation of sp^2- into sp^3-hybridized carbons, which is associated with a change from a trigonal-planar to a tetrahedral local bonding geometry. This process is energetically more favorable at the caps due to their pronounced curvature in two dimensions, in marked contrast to the sidewall with its comparatively low curvature in only one dimension. On the other hand, the non-zero curvature makes the sidewall more reactive than the planar graphene sheet. Correspondingly, the binding energy of atoms or functional groups on the sidewall should increase with decreasing tube diameter. This tendency is supported by theoretical studies, as has been reported for instance for the bonding of alkyl radicals to the SWCNT sidewall [38]. On the contrary, the concave curvature of the inner surface of the nanotube imparts a very low reactivity towards addition reactions [39], so that carbon nanotubes have been proposed as nanocontainers for reactive gas atoms, in analogy to fullerenes encapsulating nitrogen atoms (e.g., N@C60).

In reality, however, nanotubes are no ideal structures, but rather contain defects formed during synthesis. Typically around 1-3% of the carbon atoms of a nanotube take part in a defect site [40]. A frequently encountered defect type is the so-called Stone-Wales defect that comprises of two pairs of 5-membered and 7-membered rings, and is hence referred to as a 7-5-5-7 defect (see Fig. 2.10). A Stone-Wales defect leads to a local deformation of the graphitic sidewall and thereby introduces an increased curvature in this region. The strongest curvature exists at the interface between the two five-membered rings, because of which an addition reaction is the most favored at the C=C double bond there [41].

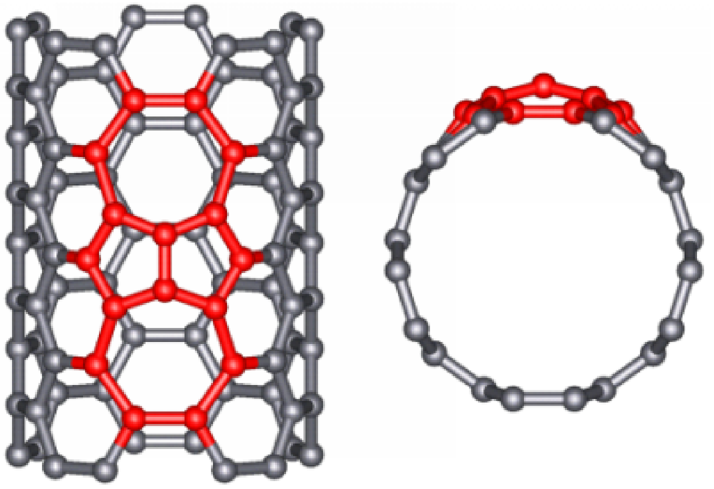

Figure 2.10: A SWCNT incorporating a Stone-Wales or 7-5-5-7 defect displaying the increased curvature resulting due to the occurence of the defect.

2.5.2 Thermally activated chemistry

Oxidation and carboxyl based coupling

A major milestone in the emerging area of nanotube chemistry was the development of an oxidation process for SWCNTs involving extensive ultrasonic treatment in a mixture of concentrated nitric and sulfuric acid [42]. Such drastic conditions lead to the opening of the tube caps as well as the formation of holes in the sidewalls, followed by an oxidative etching along the walls with concomitant release of carbon dioxide. The final products are nanotube fragments with lengths in the range of 100 to 300 nm, whose ends and sidewalls are decorated with a high density of various oxygen containing groups (mainly carboxyl groups). Under less vigorous conditions, such as reflux in nitric acid, the shortening of the tubes can be minimized. The chemical modification is then limited mostly to the opening of the tube caps and the formation of functional groups at defect sites along the sidewalls. Nanotubes functionalized in this manner basically retain their pristine electronic and mechanical properties [43]. The oxidatively introduced carboxyl groups represent useful sites for further modifications, as they enable the covalent coupling of molecules through the creation of amide and ester bonds (see Fig. 2.11). This allows one to provide the nanotubes with a wide range of functional moieties, for which purpose bifunctional molecules (e.g., diamines) are often utilized as linkers. Illustrative examples are nanotubes equipped with dendrimers, nucleic acids, enzymes, metal complexes or semiconductor and metal nanoparticles [44].

The presence of (modified) carboxyl groups leads to a reduction of van-der-Waals interactions between the CNTs, which strongly facilitates debundling of the nanotube bundles into individual tubes. Additionally, the attachment of suitable groups renders

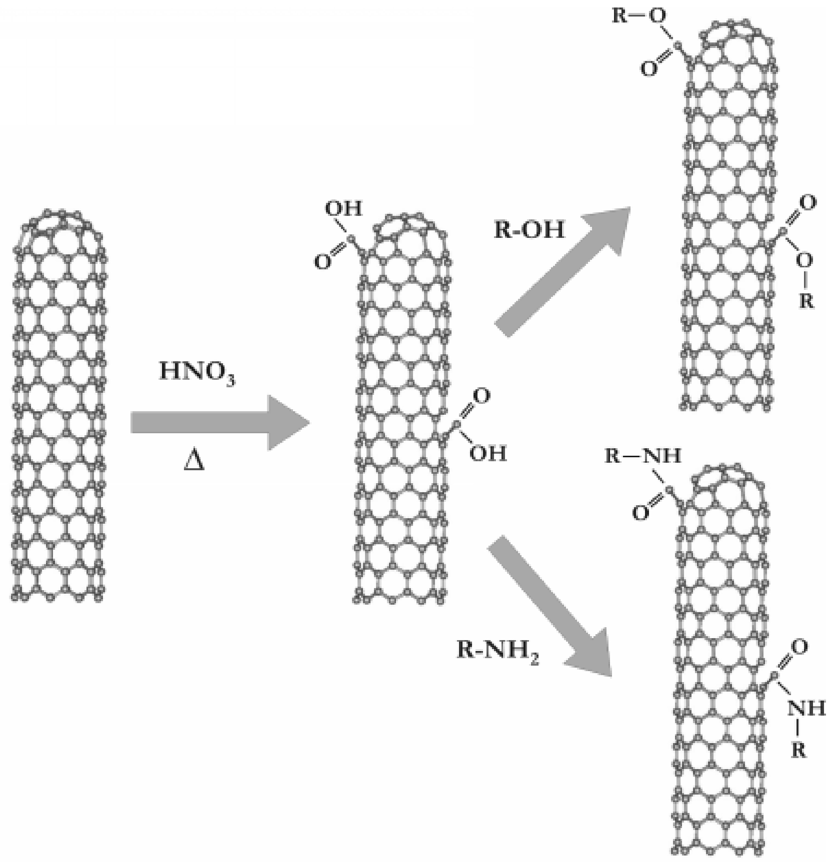

Figure 2.11: Chemical modification of nanotubes through solution-phase oxidation, followed by subsequent esterification or amidation of the carboxyl groups.

the tubes soluble in aqueous or organic solvents, opening the possibility of further modifications through subsequent solution-based chemistry. A high water-solubility of a few tenths of a gram per ml has recently been achieved on the basis of carboxyl-based coupling of hydrophilic polymers like polyethyleneglycol (PEG) [45]. SWCNTs with a good solubility in organic solvents can be obtained by covalent [46] or ionic [47] attachment of long-chain aliphatic amines onto the carboxyl groups.

Addition reactions at the sidewall

While the two–step–functionalization of nanotubes through oxidative introduction of carboxyl groups followed by the formation of amide– or ester–linkages does allow for a stable chemical modification, it has only a relatively weak influence on the electrical and mechanical properties of the nanotubes. By comparison, addition reactions enable the direct coupling of functional groups onto the π–conjugated carbon framework of the tubes. The required reactive species (atoms, radicals, carbenes or nitrenes) are in general made available through thermally activated reactions, and small-diameter tubes are preferred as they show higher chemical reactivity due to their increased curvature [48].

In the meanwhile, a series of addition reactions are well documented, the most important of which are listed in Fig. 2.12. While in the initial experiments aiming at addition reactions to the sidewall only one to three functional groups were found per 100 carbon atoms [49], the procedures developed more recently have reached functionalization degrees of at least 10% [50]. At the present stage, however, the addition mechanisms are not yet completely understood. In principle, the addition reaction could be initiated exclusively on the intact sidewall, or in parallel at defect sites from where the reaction could proceed further. For most of the reactions shown in Fig. 2.12 it is a matter of actual investigations to which extent these two possibilities contribute. One exception is nanotube fluorination, for which direct addition to the defect-free sidewall appears viable [51]. Nonetheless, the fluorine addition has a noticeable activation barrier due to which the reaction requires slightly elevated temperatures (T > 150°C). Analogous to nanotube functionalization with carboxyl groups, the direct covalent attachment of functional moieties to the sidewalls strongly enhances the solubility of the nanotubes. The good solubility of nanotubes modified with organic groups has been exploited for their effective purification [52]. In this procedure, small particles are first separated from the solution through chromatography or filtration, and then the covalently attached groups

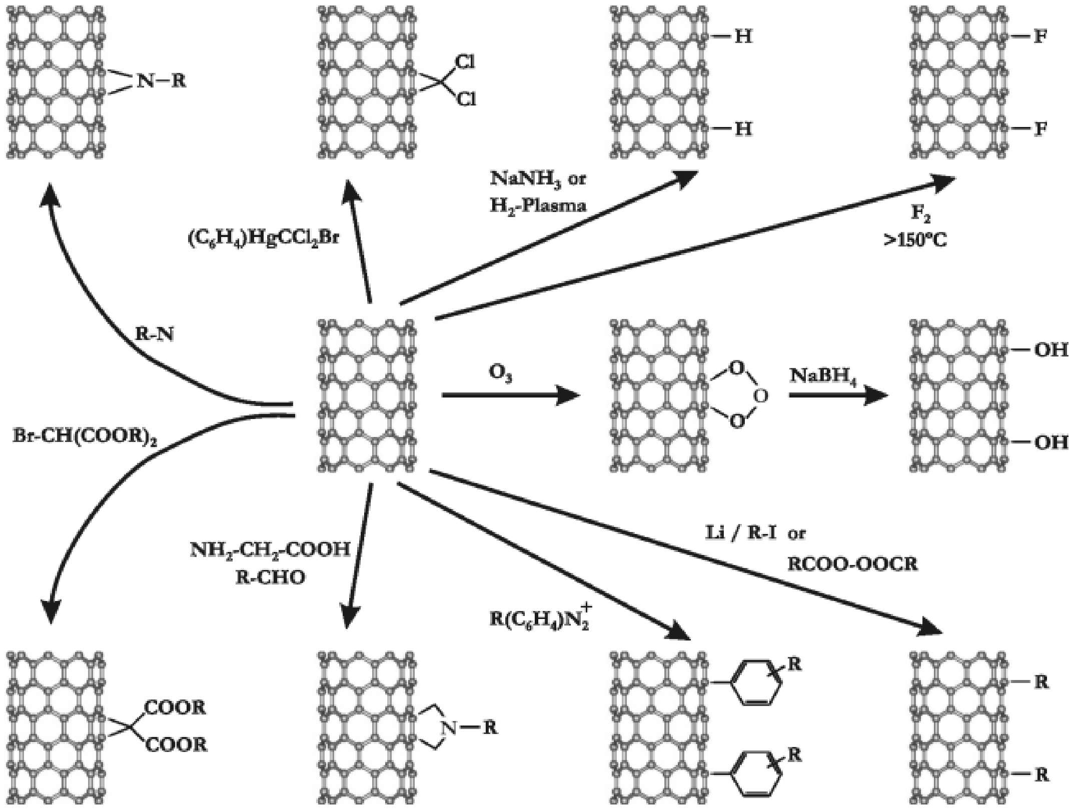

Figure 2.12: Overview of possible addition reactions for the functionalization of the nanotube sidewall.

are removed through thermal annealing (T > 250°C).

Substitution reactions on fluorinated nanotubes

The fluorine atoms in fluorinated carbon nanotubes can be replaced through nucleophilic substitution reactions with relative ease, thus opening a flexible approach for providing the sidewalls with various types of functional groups, as illustrated by Fig. 2.13. As nucleophilic reagents, alcohols, amines, Grignard reagents and alkyl lithium compounds have been successfully employed, which resulted in up to 15% of carbon atoms of the sidewall bearing a functional group [53]. Moreover, by using a bifunctional reagent, such as an α,ω-diamine with a sufficiently long carbon chain, the nanotubes can be covalently cross-linked with each other [54].

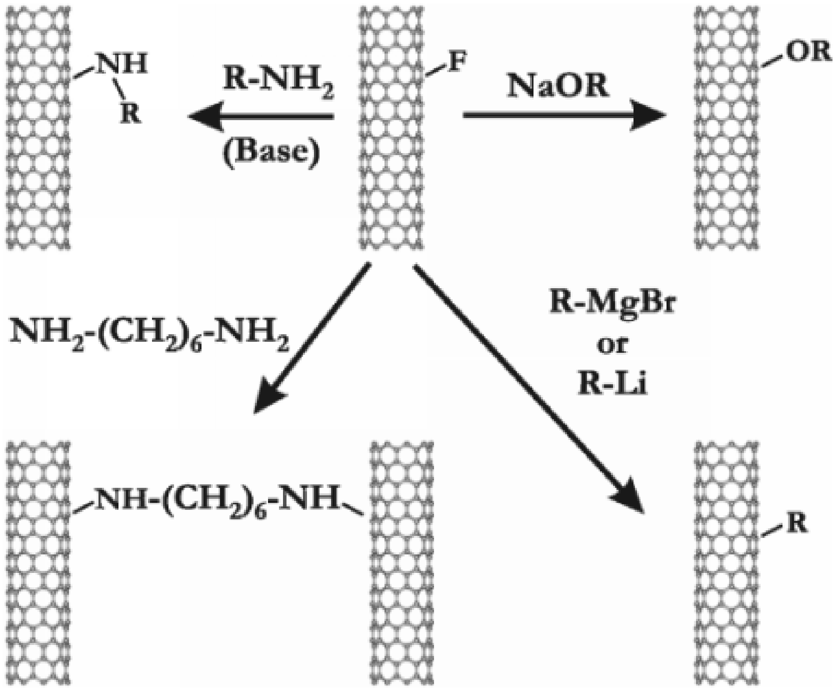

Figure 2.13: Functionalization of the sidewall through nucleophilic substitution reactions in fluorinated nanotubes.

2.5.3 Electrochemical modification

The electrochemical modification (ECM) of CNTs has until now been performed only in bulk. Depending on the precursor used in the reaction, the modification can result in a covalent or non-covalent attachment of molecular residues onto the nanotubes. Here, a short summary of the available ECM methods on bulk SWCNTs are presented.

Covalent ECM of SWCNTs in bulk

Covalent modification of SWCNTs has been successfully employed to attach organic (aromatic) residues, as well as oxygen (oxidation) and halogen atoms (halogenation). In these cases, the formation of covalent bonds has been concluded from changes in the optical absorption or Raman spectra of the tubes. As the chemical reactivity of SWCNTs increases with increasing curvature of their sidewalls [48], small diameter tubes have often been used for covalent functionalization. Especially the HiPco SWCNT material was frequently chosen, since it has a low minimum diameter of 0.7 nm. However, it should be noted that the chemical reactivity of SWCNTs is not fully explored, and there is some evidence obtained during the course of this work that also larger diameter tubes (from the arc dicharge process) are sufficiently reactive, at least towards highly active species [55].

Aromatic groups can be covalently linked to SWCNTs via reductive coupling of diazonium salts. The diazonium-based attachment of (substituted) phenyl rings to SWCNT paper electrodes represents the first example of covalent ECM of SWCNTs [56]. Pronounced changes have been observed in the Raman spectra after modification, specifically an increase in the relative intensity of the disorder mode peak (D-line) at $\approx$ 1290 cm^{-1}, and a lowering of the intensity of RBM. While the former change directly indicates an increased amount of sp^3-hybridized carbons, the latter signifies the disturbance in the carbon framework of the sidewalls. Chemical analysis of the modified products revealed that the extent of modification depends on the type of aryl diazonium salt. Functionalization degrees of up to 0.05 have been found, which corresponds to one in 20 carbon atoms bearing an aromatic residue. In the simplest scenario, the diazonium salt is reduced by accepting an electron from the SWCNT, followed by loss of nitrogen to form an aryl radical, and covalent binding of this radical to the intact sidewall via addition to the partial double bonds. On the other hand, there are experimental indications that the preferred attachment sites are defects [57]. Once started at such an initiation site, the locally enhanced curvature would enhance the attachment of further radicals, thus enabling the reaction to spread along the tube.

Noncovalent ECM of SWCNTs in bulk

The attachment of molecules onto the SWCNTs in a non-covalent manner is of interest for some applications, since the carbon framework of the tubes remains intact, and therefore their electronic properties are largely preserved. Non-covalent ECM has been utilized to coat SWCNTs with a polymer consisting of polypyrrole or polyaniline, which allows one to combine the specific properties of carbon nanotubes and electrically conducting polymers (ECP) in a novel composite material [58]. High-resolution SEM images revealed the presence of SWCNTs incorporated within the polypyrrole matrix, and the formation of dense, high-quality composite films. It is possible to control the thickness of the polymer coating on the tubes through the magnitude of the applied potential and the duration of electropolymerization.

2.5.4 Photochemical functionalization

In contrast to the chemical functionalization routes based upon thermally activated chemistry or electrochemistry, photochemical approaches have been employed to a much lesser extent until now. Photo-irradiation has been used to generate reactive species such as nitrenes in the course of sidewall addition reactions [59]. However, here the photo-activation involves exclusively the azido compound employed as nitrene precursor. Only one case of "true" photochemical modification of SWCNTs has been reported to date, which is sidewall osmylation [60,61] Initially, it has been observed that SWCNTs exposed to osmium tetroxide (OsO_4) under UV-light irradiation show a pronounced increase in electrical resistance (see Fig. 2.14). This change has been ascribed to the photo-induced cycloaddition of OsO_4 to the partial carbon/carbon double bonds, as a result of which the π–electron density in the nanotubes is decreased. It is interesting to note that when humidity is carefully avoided, the OsO_4 addition is reversible, i.e. the cycloadduct can be cleaved by photo-irradiation, whereby the original resistance is restored. In a later stage, UV-light induced osmylation of SWCNTs has been studied also in organic solvents [61]. Under these conditions, OsO_4 appears to react preferentially with the metallic tubes contained within the sample. This selectivity may originate from the availability of electronic states at the Fermi level in the metallic tubes, which facilitates the formation of an intermediate charge-transfer complex. As distinguished from the reactions performed by exposure to gaseous OsO_4, the major product in the organic medium are SWCNTs decorated with OsO_2 particles, resulting in the formation of extended tube aggregates. This difference most likely arises from the fact that in the latter case, the cycloadduct is readily hydrolyzed by the presence of water traces.

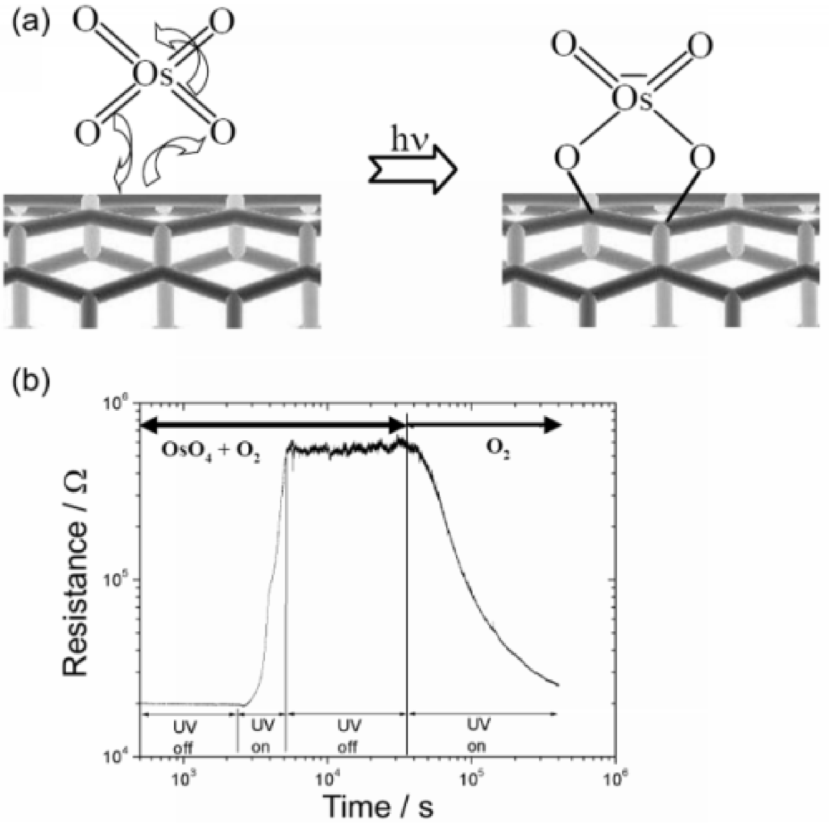

Figure 2.14: (a) Reaction scheme for sidewall osmylation of a SWCNT using UV light. (b) Resistance change of an individiual m-SWCNT upon exposure to OsO_4 and O_2 under UV light irradiation [60].

Chapter 3

Experimental

3.1 Sample preparation

For the experimental investigation of the nanotubes and for the fabrication of devices, the SWCNTs have to be brought onto a substrate. There are two different methods to perform this. The first method is based on the use of commercially available SWCNT raw material obtained by arc-discharge. In the second method, the tubes are directly grown on the substrate and are subsequently used for experiments. These two methods are outlined in this section.

Arc discharge

The arc discharge method was first invented by Ebbesen and Ajayan [62] who achieved growth and purification of MWCNTs at the gram level. This method, initially used for producing fullerenes is the most common and easiest way to produce nanotubes. However, the nanotubes obtained in this manner usually contain a large amount of unwanted impurities. This method creates nanotubes through arc-vaporisation of two carbon rods placed end to end in an inert atmosphere at low pressure. SWCNTs are obtained in the presence of a metal catalyst [25,63]. In the current work, SWCNTs from two different arc discharge processes have been used – Carbolex (Lexingtion, KY) [64] and MER (Tucson, AZ) [65]. The diameter of the SWCNTs is in the range of 1.1 to 1.4 nm.

Procedures for the synthesis of large quantities of nanotubes invariably deliver bundles (see for e.g. Fig. 3.1) that are composed of up to hundreds of single nanotubes bound together by van der Waals interactions. It is advantageous, however to have individually dispersed nanotubes instead of bundles for applications. This is important, for example, in the fabrication of nano-scale devices where nanotubes of uniform properties are a necessary prerequisite. Also while devising chemical functionalization schemes for nanotubes, it is important to provide for easy access to chemical reagents. For this purpose, ultrasonic treatment of the CNTs in an aqueous surfactant solution has turned out to be effective [34], which leads to the enclosure of the individual tubes in a detergent shell. It should be stressed that the experimental conditions have to be carefully controlled, since intensive ultrasonication may otherwise cause noticeable damage of the tube walls [66].

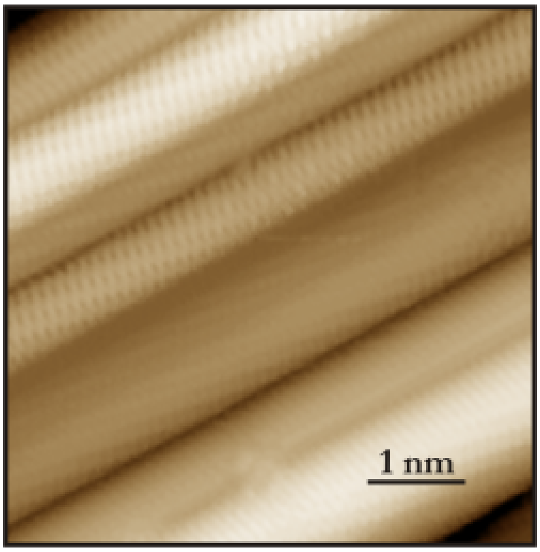

Figure 3.1: A low temperature scanning tunneling microscope (STM) image showing an atomically resolved SWCNT bundle composed of at least 8 individual tubes. *(Courtesy: Dr. Lucia Vitali)*

A 1 wt.% aqueous solution of sodium dodecylsulphate (SDS) or lithium dodecylsulphate (LDS) is used to disperse the SWCNTs using an ultrasonic stick mixer. This solution is then left in an ultrasonic bath for a few minutes to enable further debundling. Upon centrifuging this dispersion, the heavy catalyst particles and big bundles are sedimented out at the bottom. The supernatant of the resulting suspension is placed on a substrate, after the surface is treated for 2 m in an aqueous solution of 0.1 vol.% 3–(aminopropyl)triethoxysilane. After an adsorption time of 30 m, the substrate surface is dried in a stream of nitrogen and then rinsed in ultra-pure water and dried again. This procedure yields a random distribution of the nanotubes on the surface. Based on the specific application for which the samples are produced and depending on the raw material used, the parameters of ultrasonication, the speed of centrifuge and the time of deposition need to be carefully controlled. For example, a high fraction of single tubes are obtained with a strong ultrasonication and a short deposition time, while dense networks require a rather weaker ultrasonication with a longer deposition time.

Chemical Vapor Deposition

Alternatively, isolated and relatively pure SWCNTs can be directly synthesized by chemical vapor deposition (CVD) on solid support, albeit in smaller quantities (Fig. 3.2). In this approach, catalyst particles are deposited onto a substrate, and individual SWCNTs with almost uniform diameters are grown at elevated temperature (> 600°C) from the catalyst particles, using for instance methane [67] or alcohol vapor [68] as carbon source. The catalyst particles themselves are obtained from a precursor. In the present work, dendrimers containing iron deposited onto a substrate served as precursors. Upon heating in air at 800°C (calcination), the surrounding organic residues are removed and clusters of Fe_2O_3 are formed on the substrate. Such samples are then introduced into the oven at 900°C with a flow of methane in the presence of hydrogen. The Fe_2O_3 clusters are reduced to iron in the presence of hydrogen, which act as catalysts for the formation of SWCNTs. An appealing feature of this method is the possibility to control the diameter of the produced tubes through the size of the catalyst particles [69]. With the help of lithographic techniques, isolated SWCNTs grown in this manner can then directly be contacted by electrodes, and their electrical properties investigated in detail [70].

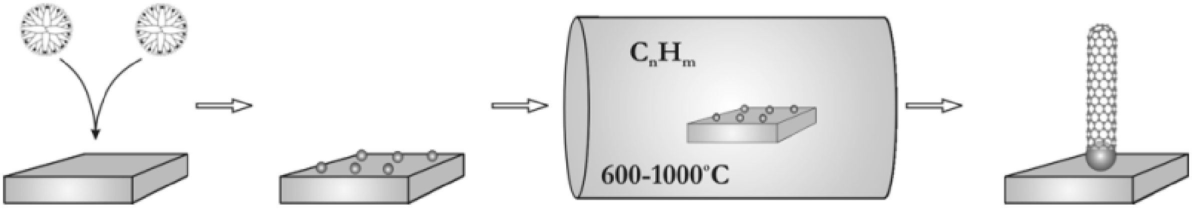

Figure 3.2: Schematic block diagram of the Chemical Vapor Deposition (CVD) procedure.

Another successful method that delivers a high yield and purity of nanotubes is the so-called HiPco process. This is a gas-phase CVD procedure [71], and tubes grown using this method have been procurred commercially and used in this work. Specifically, the CVD was performed by letting a mixture of $Fe(CO)_5$ as precursor and carbon monoxide into an oven at high pressure and elevated temperatures. Under such conditions, the catalytic production of SWCNTs is induced by the decomposition of $Fe(CO)_5$ in the presence of CO. The diameter of these tubes range roughly from 0.7 nm to 1.1 nm. Later a purification method was devised for such SWCNTs and they could be purchased only in this purified form. The purified HiPco tubes were almost completely free of amorphous carbon and catalyst particles. However, due to the defects and inhomogeneities introduced during the purification procedure, their electrical performance was quite poor as observed in our electronic transport investigations on such tubes.

Characterization by AFM

For the experiments performed in this work, SWCNTs obtained by either the arc discharge or HiPco or the CVD process have been used. The substrate comprised of n^+-Si with a thermally grown SiO_2 layer on top. The oxide thickness was either 100, 200 or 500 nm. A commercially available Atomic Force Microscope (AFM) from Digital Instruments Inc. (Multimode SPM Nanoscope III) was used for the purpose of surface characterization of these samples. AFM height images were used to obtain an idea about the density of the deposited tubes and the diameter of any specific tube. Fig. 3.3 compares the AFM images of samples obtained from the three different methods. High resolution AFM images showed that a high proportion of arc discharge SWCNTs was coated with an amorphous carbon layer, apart from the catalyst impurities on the substrate (Fig. 3.3(a)). In Fig. 3.3(b) showing the HiPco sample, the SWCNTs are more homogoeneous with a smaller density of the catalyst particles. The background dirt is due to the processing procedure, which does not originate from the HiPco raw material. It is also noteworthy that a higher fraction of the tubes appear to be single, as inferred from a height analysis of various tubes in this sample. The CVD grown tubes (Fig. 3.3(c)) on the other hand are perfectly straight and completely free of the bundle problem. They are all individual tubes of fairly uniform diameter. Again the background contains some impurities arising due to the processing steps. Thus for the purpose of fabrication of molecular electronic devices, the CVD grown tubes seem to be the most promising. This process is however still under optimization.

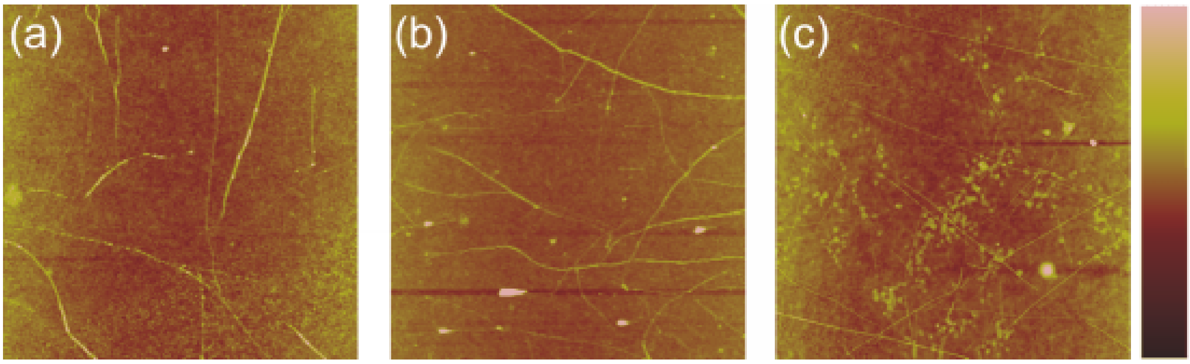

Figure 3.3: Comparison of atomic force microscope (AFM) height images of SWCNTs grown by three different methods: (a) Arc-discharge (MER) (b) HiPco and (c) Chemical Vapor Deposition (CVD). The colorbar corresponds to a height scale of 10 nm.

3.2 Electronic transport measurements

Contacting nanotubes

The predicted electronic structure of SWCNTs has been verified by a series of Scanning Tunneling Microscopy (STM) and Spectroscopy (STS) experiments [72, 73]. In these studies, the SWCNTs are deposited onto a metallic substrate and individual SWCNTs are investigated at very low temperatures of down to 4 K. However, for device applications it is essential to have the nanotubes on an insulating substrate. For this reason, silicon substrates with a thermally grown oxide layer are utilized here. The substrate itself has a metallization layer at the bottom, which functions as the gate electrode. A block diagram of the sample composition is shown in Fig. 3.4. The substrate, after deposition of the nanotubes, is coated with an electron beam resist namely polymethylmethacrylate (PMMA). Then, electrodes are defined using electron beam lithography and the desired metal is subsequently deposited. After this, the remaining PMMA is removed during the lift-off procedure. By controlling the density of the nanotubes on the substrate, a reasonably high fraction of the randomly lying nanotubes can be contacted by the electrodes. Typically, three-fourths of the electrode structures are contacted by at least a single SWCNT. The fabrication of the samples in this manner results in a field-effect transistor configuration of the device with the nanotube acting as the transistor channel that is contacted by drain and source electrodes.

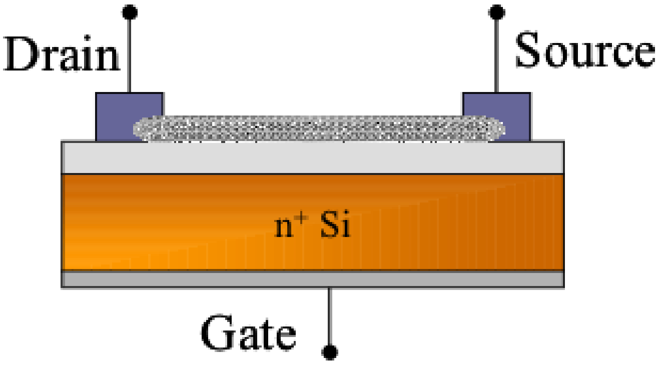

Figure 3.4: A model of the samples used in the experiments. The substrate comprises of n^+-Si with a thermally grown oxide layer acting as the insulating gate oxide. A single SWCNT or a bundle of SWCNTs contacted between source and drain electrode forms the channel to yield a field-effect transistor configuration.

Different electrode structures have been used as part of this work. The most common of them is the 4-finger structure useful for the measurement of 4-probe electronic transport through individual nanotubes. The electrodes are ≈100 nm wide and the spacing between them is around 150 nm. An AFM image of a representative sample with a

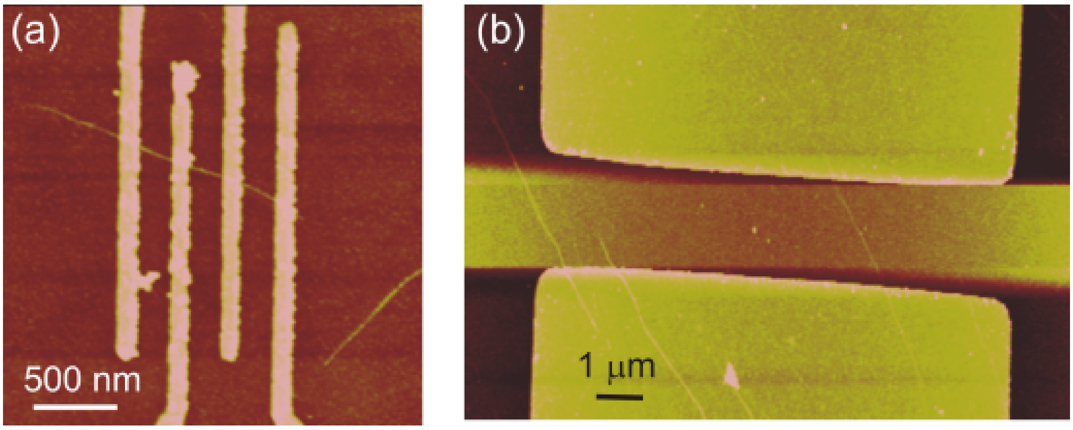

Figure 3.5: AFM images of typical samples obtained after the deposition of electrodes by electron beam lithography. (a) 4-finger structure with a single nanotube contacting all the 4 electrodes. (b) Gap structure showing another single contacted SWCNT.

nanotube contacted by all the four electrodes is shown in Fig. 3.5(a). The electrodes travel outwards to huge bondpads, which are approximately 200 μm x 200 μm in size. These bondpads serve as the interface to the outside world and are either contacted by probe needles or by bond wires that are further hooked up to the measurement system. Another electrode architecture used in this thesis is the gap structure with two electrodes that are 10 μm wide and separated by $\approx$1.3 μm (see Fig. 3.5(b)).

The measurement setup for electronic transport comprises of a voltage source (Keithley 2400) that supplies the drain voltage V_{ds} through a buffer. The current at the source end (I_{d}) is first fed into a current-to-voltage (I-V) converter to amplify the signal and the output voltage is recorded by a multimeter (Keithley 2000). The gate voltage (V_{G}) is applied through a second voltage source (Keithley 2400) with the capability to measure the leakage current (I_{G}) through the insulating oxide layer. Two sets of measurements are performed on any sample. The first one involves obtaining a current-voltage (I-V) curve of the device, where the bias V_{ds} is varied over a certain voltage range (typically $\leq$ 100 mV) and the current I_{d} measured at every voltage point. The slope of such an I-V curve gives the resistance of the contacted nanotube. This resistance when measured across two contacts is the 2-probe resistance, which includes the resistance of the contacts between the electrode and the nanotube. In samples made in the 4-finger architecture, when the nanotube is contacted by all 4 electrodes, the 4-probe resistance of the contacted nanotube can be measured. This measurement accounts for the contact resistances and one obtains the intrinsic resistance of the nanotube independent of the contacts. This set of measurements are taken at $V_{\mathrm{G}} = 0$ V. The second set of measurements is performed to obtain the gate dependence of conductance (GDC) of the device. Here V_{G} is varied over a certain voltage range and the conductance (G) of the tube is measured at every value of V_G at small drain-source bias, providing information about the switching capability of the device.

Room-temperature measurements

Room-temperature electronic transport measurements are used to find out if a specific contacted nanotube is metallic or semiconducting. Following the fabrication of the device, AFM images are used to determine if a certain electrode structure incorporates a contacted SWCNT. The diameter of the SWCNT can be obtained from the AFM height images. Subsequently the resistance and the GDC of the device are measured at room temperature. With the same electrode material and the same type of SWCNT raw material, m-SWCNTs show room-temperature resistances that are at least one order of magnitude lower than that of s-SWCNTs. As-prepared s-SWCNTs that are not subjected to specific treatments principally behave as *p*-type semiconductors [7], where holes are the majority carriers. They exhibit a strong modulation of conductance upon varying the gate voltage (see Fig. 3.6, red curve). By comparison, the conductivity of m-SWCNTs is barely influenced by the application of a gate voltage (see Fig. 3.6, black curve). GDC curves are thus routinely used to distinguish between a metallic and

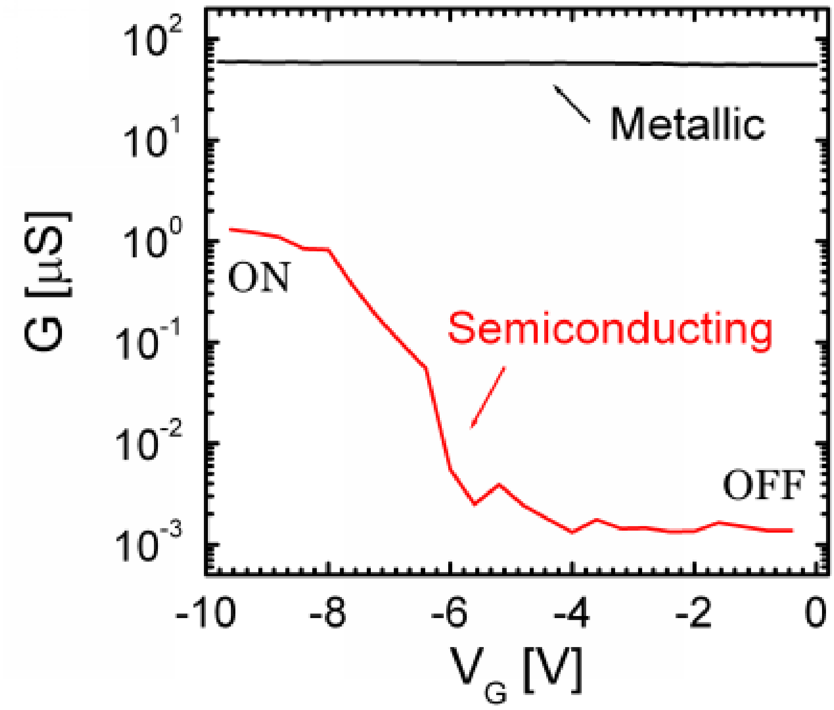

Figure 3.6: Gate dependence of conductance (GDC) for a single m-SWCNT (black curve) and a single s-SWCNT (red curve). Whereas the GDC for a m-SWCNT remains constant over the measured range of V_G, the GDC for a s-SWCNT shows a variation of around 3 orders of magnitude.

a semiconducting nanotube. The high conductance state is referred to as the *ON* state and the low conductance the *OFF* state. For the purpose of quantifying the switching ability, it is worthwhile introducing a unitless quantity called the Gate Dependence Ratio (GDR), which is the ratio of the *ON* conductance to the *OFF* conductance. Purely m-SWCNTs have a GDR between 1 and 2, while s-SWCNTs show a GDR of at least 10^3.

The measurements carried out at room-temperature in ambient conditions display a pronounced hysteresis in the GDC curves as shown in Fig. 3.7. The gate voltage scan

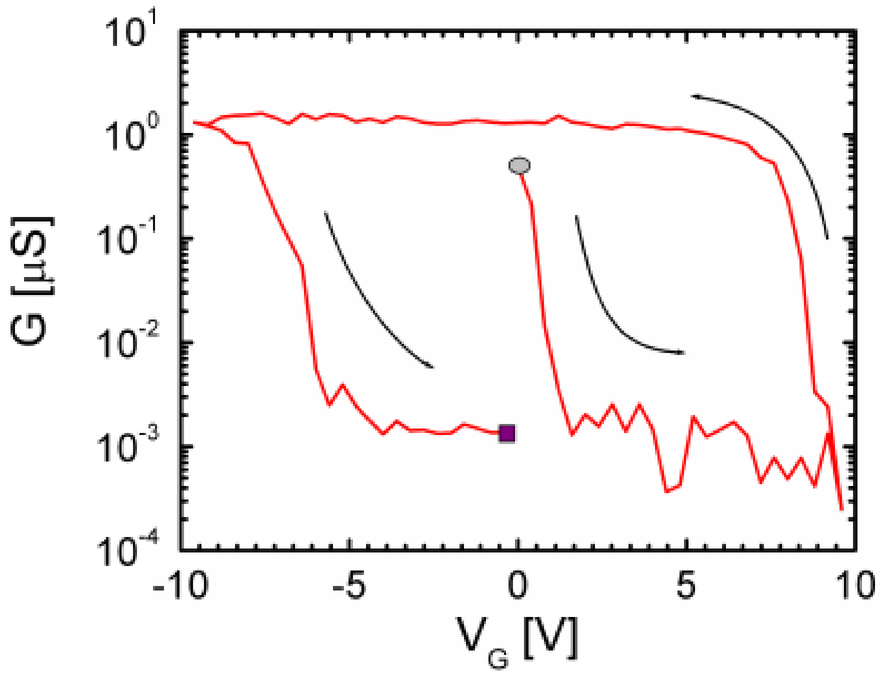

Figure 3.7: Gate dependence of conductance for a single s-SWCNT showing the hysteresis arising due to charge traps present in the vicinity of the SWCNT.

was started at the point marked with the solid circle and stopped at the point marked with the solid square. going through the positve maximum first at $V_G = +10$ V and then through -10 V. The orgin of this hysteresis has been attributed to defect-related charge traps either in the SiO_2 dielectric [10] or very close to the nanotube [74, 75]. Moreover, under ambient conditions, it is reasonable to expect the surface of the device to be covered by a layer of water molecules. Recent experiments have shown that such surface-bound water molecules act as trap sites inducing hysteresis in such devices [76]. These experiments have furthermore demonstrated that one can get rid of the hysteresis by heating over a long period of time to remove the water molecules from the surface. Alternatively, one could also use a thick PMMA coating over the fabricated device to obtain a hysteresis-free SWCNT device. The latter method has however the disadvantage that the surface of the nanotube is no more accessible after perfoming this coating.

Metallic SWCNTs

The coherence length of electrons travelling in carbon nanotubes is of the order of 500 nm [77]. Thus in short nanotube fragments, electrons can travel from one end to the other without any appreciable scattering. In such cases where the transport is ballistic, the conductance of a nanotube is given by Landauer's equation [78] as $G = (2e^2/h)\sum_i^N T_i$, where $2e^2/h$ is the conductance quantum and T_i is the transmission probability of each subband (conduction channel) that is contributing to transport. As shown earlier, there are two subbands crossing at the Fermi energy for a metallic nanotube and hence $N = 2$. In the absence of scattering ($T_i = 1$, ballistic transport), the conductance of a m-SWCNT at low electron energies is $4e^2/h$. Alternatively, the two-terminal resistance of a m-SWCNT in the ideal case is $\approx 6.5\ k\Omega$. This resistance is a contact resistance arising due to the mismatch between the number of conduction channels in the SWCNT and the macroscopic metal leads [79]. In addition to this mismatch, poor coupling between the leads and the SWCNT can increase the two-terminal resistance of a m-SWCNT.

The type of the metal used to contact the SWCNTs determines the coupling between the leads and the SWCNT. Ohmic contacts with minimum contact resistance are important to achieve the best coupling. Such ohmic contacts to individual m-SWCNTs have been possible by Cr [80] and pure Pd [77]. This has enabled the observation of quasi-ballistic transport at low-temperatures, with conductances of the order of $3e^2/h$ at 4 K. Although ballistic transport has been observed with Ti ($G_{4K} \approx 2e^2/h$) [81], such contacts are less reliable and their reproducibility has been found to be quite poor [82]. In these experiments, the low-temperature conductance was greater than $2e^2/h$ implying that at least one transport channel was intact and the coupling was near optimal. Upon cooling from room-temperature, the resistance of such samples decreased due to the suppression of phonon-scattering at lower temperatures [83]. On the other hand, individual defect-free m-SWCNTs contacted by other metals show in general $G < 2e^2/h$ at room-temperature. The resistance of such samples increases upon lowering the temperature [84, 85], signifying that potential barriers at the contacts formed due to sub-optimal coupling have a strong impact on the transport.

In this work mainly two types of contacts have been used. In the first category of samples, a Ti adhesion layer (typically less than 1 nm) was evaporated onto the SWCNTs followed by 15 nm of AuPd. The second set of samples was fabricated with AuPd electrodes directly contacting the SWCNTs. In both of these types of samples the room-temperature conductances were much lower than $2e^2/h$. The conductance decreased upon lowering the temperature indicating that the transport in these samples was strongly restricted by the barriers at the contacts. The reduction in conductance upon cooling could also be explained by the presence of structural defects such as vacancies, pentagon-heptagon pairs and Stone-Wales defects [31]. However, in such a case a weak gate dependence of conductance would be observed [86]. The GDC curves of such defective tubes exhibit gate dependence ratios in the range of 3 to 100. Thus the GDC curves, apart from being able to distinguish between m-SWCNTs and s-SWCNTs, can also be effectively used to identify if a contacted tube is defect-free or not.

Semiconducting SWCNTs

Similar to the case of m-SWCNTs, the electrical characteristics of s-SWCNTs is dependent to a large extent on the type of metal used to contact them. s-SWCNTs contacted by gold electrodes in general exhibit a *p*-type behavior due to the Fermi level of gold aligning with the valence band of the s-SWCNT, making a barrier for the injection of electrons [87]. It was found that this *p*-type behaviour in s-SWCNT-FETs is due to the formation of Schottky barriers at the contacts, rather than an intrinsic effect [88]. Later experiments [89] confirmed that the electrical performance of such FET devices was restricted by the existence of these Schottky barriers and their response to the applied electric fields. Thermionic emission and tunneling are involved in transport across the barriers, which limit the *ON* state conductance of a nanotube FET to well below the $4e^2/h$ limit at room temperature [88, 90]. The use of Ti as the contacting metal followed by a rapid thermal annealing procedure helped in the achievement of ambipolar transport in SWCNTs [91] exhibiting relatively low resistance for the injection of both *p*-type and *n*-type carriers. However, ballistic transport could still not be observed in the Ti-contacted SWCNT FETs. Only recently, it has been shown that contacting short segment s-SWCNTs (of length < 500 nm) by Pd greatly reduces or eliminates the barriers for transport yielding ballistic s-SWCNT-FETs [11]. In the samples used in this work, s-SWCNTs contacted by AuPd/Ti electrodes have been found to exhibit lower *ON* conductances than those contacted by AuPd, signifying that the Schottky barriers in the former case is higher and/or wider than that in the latter.

3.3 Confocal laser scanning microscopy

Initial experiments on Raman spectroscopy of carbon nanotubes used focussed laser beams of μm spot sizes and generally probed a sample containing a large amount of SWCNTs in solution. A spectrograph was used to collect the scattered light from the whole solution. Due to the presence of a large number of tubes in such samples, a superposition of RBMs, whose relative intensities are strongly affected by the resonant conditions [92] is observed in these Raman spectra. Furthermore, the occurence of bundles leads to a broad G-line in the Raman spectrum as shown in Fig. 3.8. The successful use of Raman spectroscopy as a characterization tool for nanotubes requires the observation of Raman spectrum on individual tubes. For this purpose, confocal laser scanning micrsocsopy is used, which has the ability to obtain spectroscopic information from individual nano-scale objects. In this section the principle of confocal microscopy will be described, and then the experimental setup used in this work will be presented.

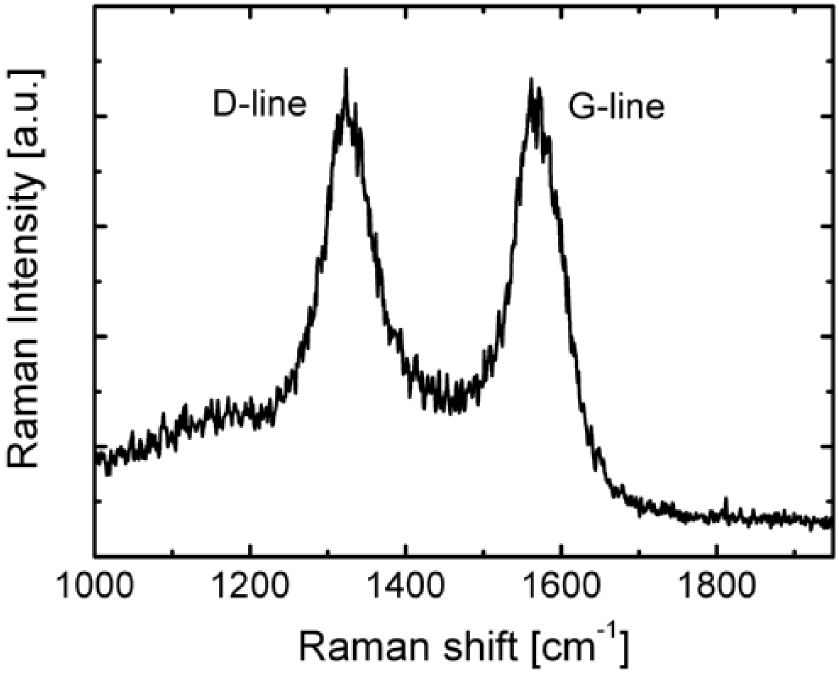

Figure 3.8: A typical Raman spectrum of an ensemble of SWCNTs. Due to intertube interactions and tube bundling, the G-line is broadened in this spectrum.

Principle of confocal laser scanning microscopy

The intensity of the signal delivered by the detector of a spectrograph analyzing a given Raman line at the wavelength λ can be expressed [93] by $S \approx I_0 \sigma_\lambda N \Omega T_\lambda s_\lambda$, where I_0 is the laser intensity falling on the sample (W/cm^2), σ_λ is the differential cross-section for the Raman line analyzed (cm^2 sterad^{-1} molecule^{-1}), N is the number of molecules in the probed volume V, Ω is the solid angle of collection of the Raman light, and T_λ and s_λ are the throughput of the instrument and the sensitivity of the detector at λ, respectively. To be able to analyze individual objects, just a small volume of the target needs to be illuminated. In such a situation, only a few parameters can be modified to compensate for the large reduction in the number of molecules N that are present in the probed volume V. These are the incident light intensity I_0 and the solid angle of collection Ω. It was found that the use of the same microscope objective for both illuminating the sample and collecting the scattered light (and hence the name *confocal* microscopy) was the best way to decrease V while simultaneously increasing Ω and I_0. Indeed, high magnification microscope objectives, which have high-numerical aperture (NA) optics are able to focus the laser beam into a very small volume and to collect, under a wide angle, the light scattered by this volume. Thus both the enormous increase of the local laser intensity I_0 and the wide angle of collection Ω compensate for the decrease of the number of molecules N. The smallest size of the illumination spot that can be achieved in this manner is diffraction-limited, and the diameter of such a spot that is obtainable with a very good objective is $\approx \lambda_{\mathrm{exc}}/2$.

Confocal microscopy thus enables the maximum possible resolution in the optical far-field through a combination of optical excitation onto and detection from a diffraction-limited volume of the sample. The microscope is based on the use of a highly focussed laser beam for illuminating the sample combined with the use of a pin-hole as a spatial filter for detection. The pin-hole ensures that only scattered light from the illuminated volume passes through to the detector and thus delivers a huge enhancement in resolution along the axial direction. Since this light contains no spatial information, a point detector is sufficient to analyze the scattered light. To be able to still obtain an image of the sample, the excitation volume in connection with the detection volume must be continuously shifted with respect to the sample. This can be done in two different ways. In the first method that has been implemented in the confocal microscope used in this work, the sample is raster-scanned below the stationary focal spot of the microscope. The second method utilizes a scanning laser beam with a stationary sample to obtain an image of the sample. In contrast to the usual far-field imaging using a conventional microscope where the imaging is done at once, confocal imaging is a sequential procedure. It is possible to obtain images in various planes of a thick sample and obtain a 3D reconstruction of the analyzed data. The scattered light that is collected by the microscope constitutes the Rayleigh, fluorescence and Raman components. Through appropriate optical instrumentation the desired component can be filtered and recorded as a function of position of the sample. This results in confocal reflection, confocal fluorescence or confocal Raman images, respectively.

Instrumentation

The experimental setup of the confocal laser microscope used in this work [94] is depicted in Fig. 3.9. It comprises of an Argon-Krypton ion laser (Coherent, Innova 70

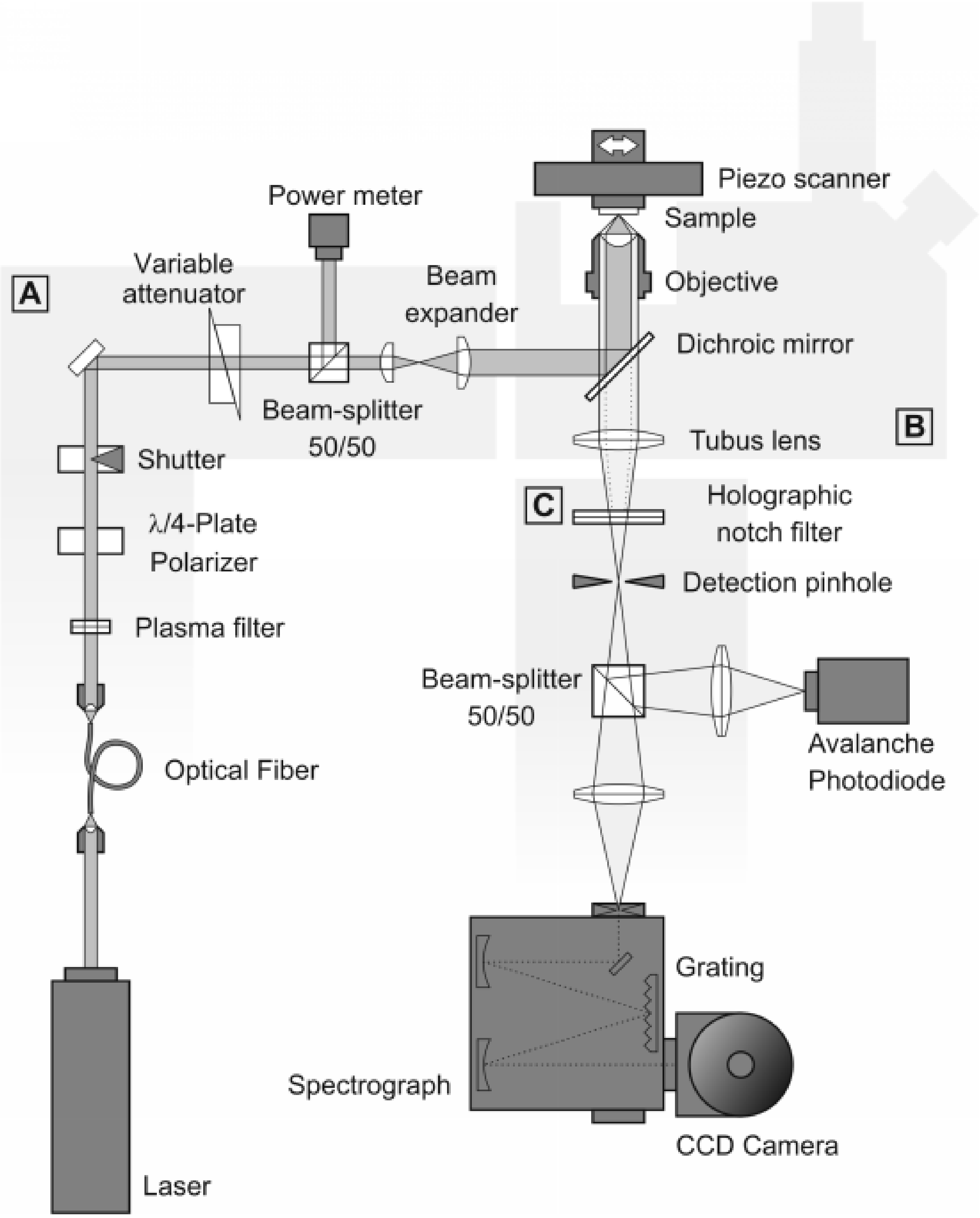

Figure 3.9: A block diagram of the experimental setup for confocal laser scanning Raman microscopy [94].

Spectrum) that is used as the source of linearly polarized monochromatic light with wavelengths of 647.1 nm and 514.5 nm. To avoid the spatial drift of the laser beam (lateral displacement during adjustment and thermal drift of the laser resonator), the laser light is first passed through a monomode glass fiber and then through a plasma filter, which allows light of just the desired wavelength to pass through. This is followed immediately by a polarizer and a $\lambda/4$-plate that produces circularly polarized light. This is important to ensure that SWCNTs of various orientations lying on the substrate can all be uniformly excited, since the efficiency of excitation is dependent on the relative orientation of the nanotube axis with respect to the light polarization. For performing polarization-dependent measurements, a motorized polarizer was additionally introduced, which enabled to continuously modulate the polarization of the incident light beam with a specified frequency. The beam is then guided through various mirrors into a variable attenuator with the help of which the intensity of the laser beam could be varied between 0.3 mW and 15 mW. Before entering the microscope (Zeiss Axiovert 135 TV), the beam is conditioned through a system of lenses to enable maximum illumination of the microscope objective. The objective then focusses the beam down to a spot that is diffraction-limited in size. For performing the Raman experiments, a 100X objective ($f = 1.645$ mm) with an NA of 0.9 and a working distance of 0.27 mm was used. The lateral resolution that is achievable mainly depends on the NA of the objectives, and is given by $0.4\lambda_{\mathrm{exc}}/\mathrm{NA}$. Usually a power of 1 mW is used in the experiments that corresponds to a light intensity of $\approx$0.5 MW/cm^2 at the center of the focussed diffraction-limited spot. As discussed earlier, this value of I_0 is quite high, which helps in compensating for the reduction in the volume V of the sample that is illuminated. The SWCNTs can withstand such high light intensities for a reasonable period of time (in the order of a few hours). But upon prolonged exposure for more than 6 hours, defects were found to be introduced in the nanotubes.

The scattered light from the sample collected by the same objective lens passes through a 50:50 semi-transparent mirror and is then focussed onto a pinhole through a convex lens. This detection pinhole is responsible for filtering the stray light arising from sources that are out of the illumination volume, and hence to improve the signal-to-noise ratio. The filtered beam contains a strong Rayleigh component due to the high intensity of the incident laser beam. To suppress this component, a holographic notch filter (Super-Notch-Plus) centered at the laser wavelength is used. This filter attenuates the incoming signal strongly in a small band of $\pm$100 cm^{-1} around the specified wavelength. The Raman components in the scattered light are normally around 30 orders of magnitude weaker than the Rayleigh component. Thus the attenuated light still contains a reasonable amount of detectable Rayleigh component that can be used for obtaining a reflection image. At the same time, the signal-to-background ratio of the Raman components is considerably enhanced through the use of this notch filter. After the notch filter, the light passes through a 50:50 beam-splitter, which guides 50% of the light into an Avalanche Photo Diode (APD) for measurment of the reflected light and the remaining half into a spectrograph. The spectrograph consists of a grating that disperses the incident light and detects the resulting spectrum with the help of a CCD camera. Three different gratings were used in the experiments – the first two of them having 150 and 300 lines per mm, with a low resolution to cover a broad range of wavenumbers and the third having 1800 lines per mm for high resolution spectra. To obtain Raman images, a specific band of the diffracted light from the grating at a desired wave number could be chosen to fall on a second APD. For example, G-line Raman images were obtained by using the 300-line grating and filtering the light at 1590±10 cm^{-1} through to the APD. The signal from the APD is then recorded as a function of position to obtain the desired Raman image. An example of such a Raman image is shown in Fig. 3.10 along with the corresponding AFM image, where the SWCNTs lying close to the electrodes can be clearly identified in the Raman images. In principle, this procedure could be performed also by using the D-line and the RBM. But since the signal-to-noise ratio at these frequencies are much lower, such images are seldom acquired.

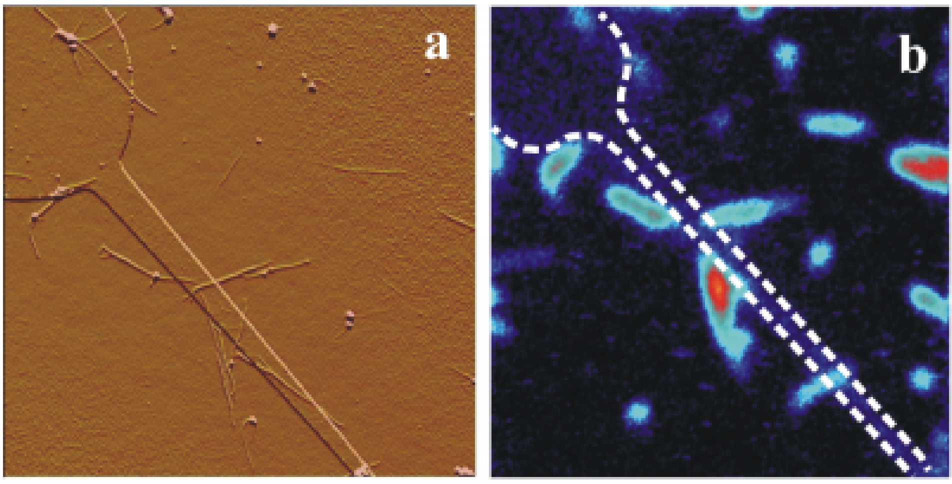

Figure 3.10: Confocal Raman Imaging of individual SWCNTS: (a) AFM image of a sample showing an electrode with adjacent lying SWCNTs (8 μm x 8 μm). (b) A confocal G-line Raman image (10 μm x 10 μm) of the same sample taken with $\lambda_{\text{exc}} = 647.1$ nm. The electrode structure is drawn in white, the background appears dark blue and the SWCNTs appear as light blue to red regions.

Confocal Raman spectra of individual SWCNTs

Utilizing the above confocal imaging setup, individual nanotubes lying on the substrate can be located from the Raman images, as exemplified by Fig. 3.10. With the help of such a Raman image, the confocal spot can be positioned on top of a specific SWCNT and its Raman spectrum acquired. According to the resonance property of the SWCNTs, the Raman signals are best obtained using $\lambda_{\text{exc}} = 514.5$ nm for arc-discharge s-SWCNTs and $\lambda_{\text{exc}} = 647.1$ nm for arc-discharge m-SWCNTs. Examples of such spectra in the high-frequency regime obtained from a single m-SWCNT and from a single s-SWCNT are shown in Fig. 3.11. The G-line has the strongest intensity in both the spectra, while the intensity of the D-line is quite low suggesting that the tubes are free of structural disorder. The Raman spectrum for the m-SWCNT shows an additional broad band whose maximum is around 30 cm^{-1} below the G-line, which results from the coupling of the free electron gas in a m-SWCNT with the phonon modes of the CNT framework [95]. This feature enables one to ensure that the observed SWCNT is indeed metallic. In this work, confocal Raman spectra are used concomitantly with electronic transport measurements to routinely identify a specific individual SWCNT as being metallic or semiconducting.

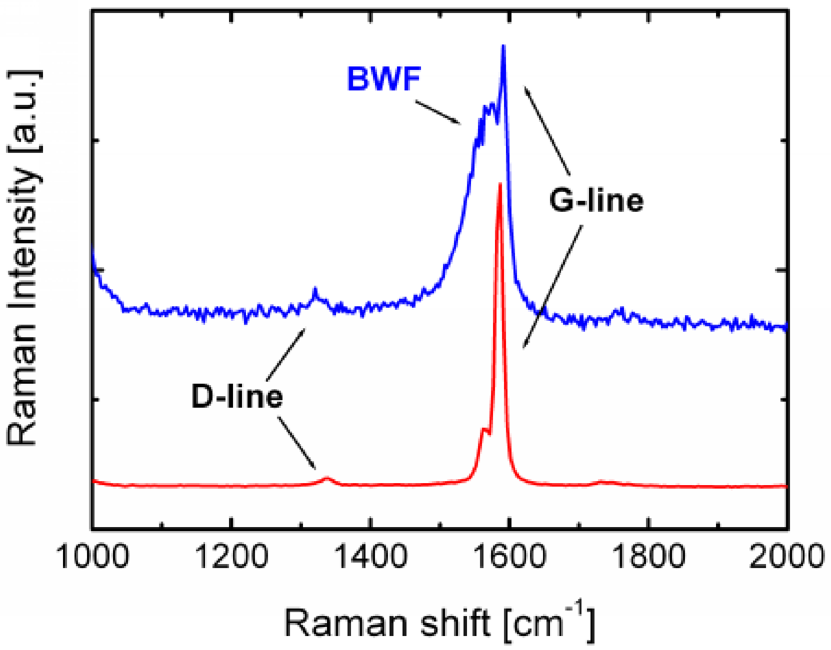

Figure 3.11: Resonant Raman spectra from an individual m-SWCNT using a laser wavelength of $\lambda_{\text{exc}} = 647.1$ nm (blue curve) and from an individual s-SWCNT with a laser wavelength of $\lambda_{\text{exc}} = 514.5$ nm (red curve). Apart from the D- and G-lines in both the tubes, the m-SWCNT exhibits a pronounced band called the Breit-Wigner-Fano (BWF) line.

Chapter 4

Electrochemical modification of individual nanotubes

Inspired by the available electrochemical modification (ECM) schemes on carbon nanotubes in bulk, the work in this thesis was focussed on the investigation of such schemes on individual SWCNTs. ECM is normally performed potentiostatically (at contstant potentials) or galvanostatically (at constant currents) in a solution containing a molecular agent as precursor for an active species (e.g., a radical or a radical ion) that will be formed through electron transfer with the nanotube electrode. A schematic of such a process is shown in Fig. 4.1. Since many organic radical species have a tendency to react with the precursor or to self-polymerize, a polymer coating is formed on the tubes. Such polymer deposition may or may not be accompanied by the formation of covalent bonds to the carbon framework of the nanotubes. As a general advantage, electrochemical deposition procedures, in addition to being simple, clean, and efficient, also allow for good control over the rate and extent of film deposition by the application

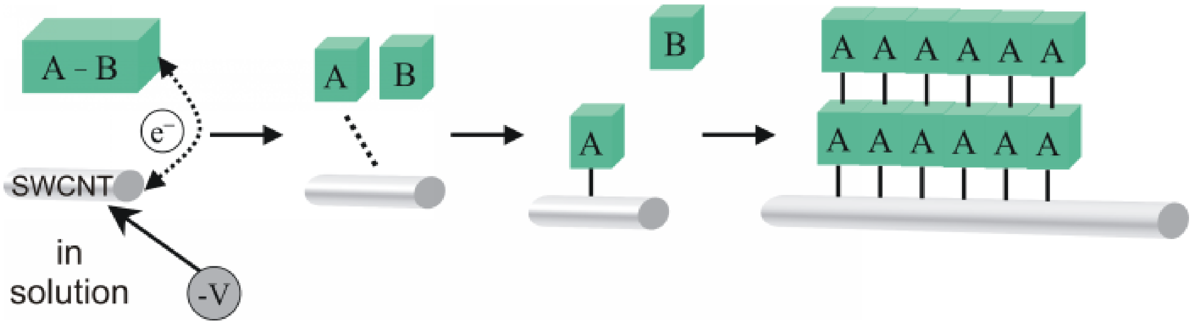

Figure 4.1: A simplified scheme depicting the electrochemical modification process. Application of an electric potential onto a contacted SWCNT within a solution containing precursor molecules (AB) leads to a charge transfer resulting in the covalent or non-covlent coupling of the generated reactive species (A) on to the nanotube. Polymerization of the radical leads to a multilayer coating.

of appropriate electrochemical conditions such as duration and magnitude of the applied potential. Furthermore, the use of a suitable agent containing the required substituent enables one to tailor the chemical and physical properties of the resulting film.

This chapter starts with a short description of the experimental setup used for electrochemical modification. This is followed by a discussion of two different coupling schemes used in this work, namely oxidative and reductive ECM. The characterization of individual SWCNTs modified by these two schemes is then presented. The next section details the selective electrochemical modification of exclusively the m-SWCNTs in an ensemble to obtain all–semiconducting networks that can be operated as FETs. The chapter concludes with a collection of potential experiments for future work.

4.1 Instrumentation

The electrochemical experiments were carried out in a micro cell of capacity ≈ 500 μL (see Fig. 4.2). The cell is made of teflon and comprises of platinum counter and pseudoreference electrodes. A tungsten needle probe was used to make contact with the electrodes on the substrate surface, which enabled the functioning of SWCNTs as the working electrode. For the control of the potential that is applied to the SWCNTs through the working electrode and for monitoring the resulting current through the electrochemical cell a Solartron 1285 potentiostat was used.

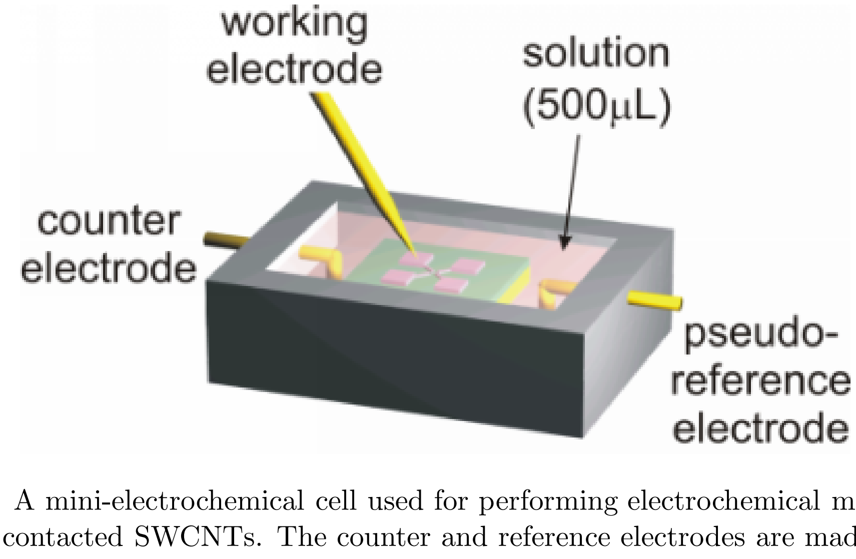

Figure 4.2: A mini-electrochemical cell used for performing electrochemical modification on individually contacted SWCNTs. The counter and reference electrodes are made of platinum and a tungsten probe needle is used to contact the electrodes connected to the SWCNT. The cell has a capacity of 500 μL.

4.2 Electrochemical modification

4.2.1 Coupling schemes

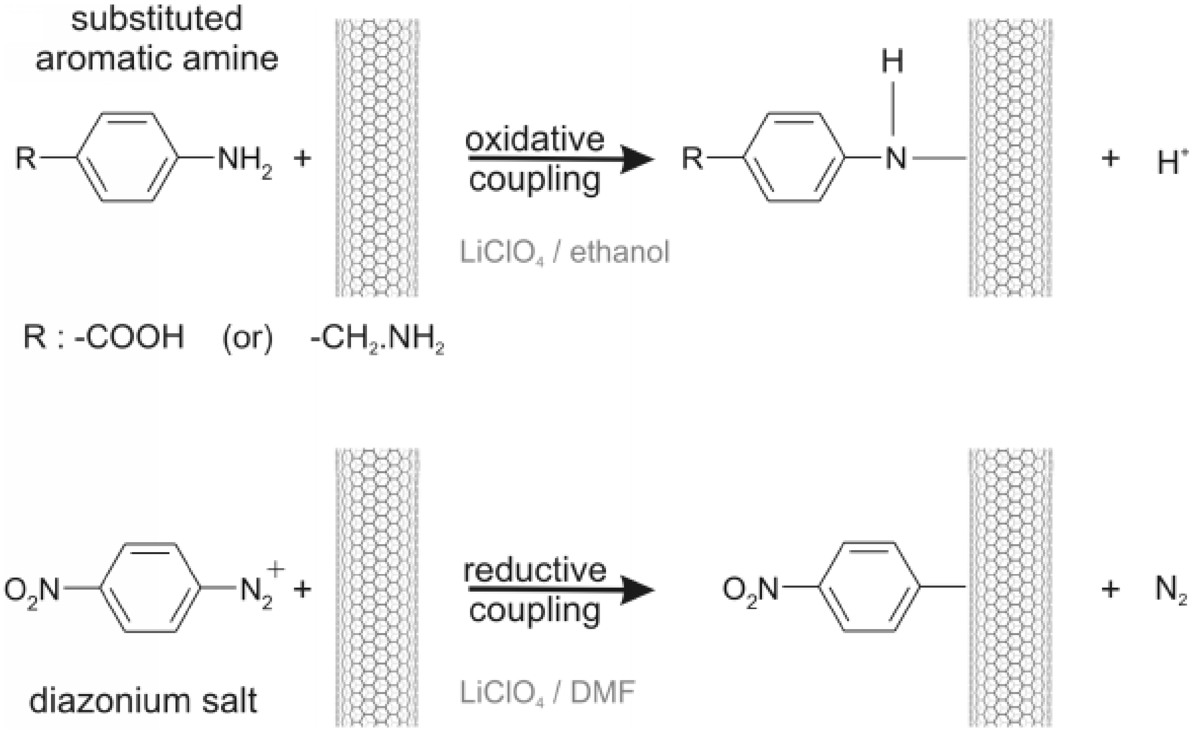

Figure 4.3: Proposed coupling schemes for ECM of individual SWCNTS. Above: Oxidative electrochemical attachment of a substituted aromatic amine. Below: Reductive electrochemical coupling of a diazonium salt.

The main goal here was to study the effect of two different coupling schemes on the structural and electronic properties of SWCNTs. These two reaction schemes are outlined in Fig. 4.3. The first scheme is based on the electrochemical oxidation of a substituted aromatic amine at anodic (positive) potentials, while the second reaction utilizes the reductive coupling of a diazonium salt at cathodic (negative) potentials. Specifically, the anodic coupling was tested on the oxidation of 10 mM 4-aminobenzylamine, $H_2N(C_6H_4)CH_2NH_2$ (**A**), with 0.1 M $LiClO_4$ as the supporting electrolyte in ethanol. In a bulk electrochemical cell, the peak of the irreversible oxidation wave of **A** caused by the formation of the radical cation, was observed at +0.75 V versus Pt. The same voltage was applied to the SWCNTs for a fixed period of 120 s. The cathodic coupling was accomplished by the reduction of 10 mM 4-nitrobenzene diazonium tetrafluoroborate $O_2N(C_6H_4)N_2^+BF_4^-$ (**B**), with 0.1 M $LiClO_4$ as the supporting electrolyte in N,N-dimethylformamide (DMF). The peak of the irreversible reduction wave of **B** which signifies the formation of the phenyl radical, was observed at -1.3 V versus Pt in the bulk electrochemical cell. This potential was applied for 120 s onto the SWCNTs. In both cases, the modification resulted in thick and reproducible coatings around the SWCNTs that was easily detectable by the AFM.

The ECM was performed on arc-discharge (Carbolex) SWCNTs contacted in the 4-finger architecture by AuPd electrodes. The electrodes served as an interface enabling the SWCNTs to act as a working electrode in the mini-electrochemical cell. AFM height images were obtained before and after ECM to determine the height increase upon modification. Furthermore, the SWCNTs were characterized before and after ECM through electronic transport measurements and confocal Raman spectroscopy, with both the techniques having the ability to address selected single SWCNTs or bundles. While transport measurements give information about the electronic properties of an individual SWCNT, confocal Raman spectroscopy on individual nanotubes can detect changes of the vibrational properties and hence the disturbances in the lattice structure of an isolated nanotube. These studies were performed separately on m-SWCNTs and s-SWCNTs, in both cases comparing the effect of the oxidative and reductive coupling schemes.

4.2.2 Oxidative electrochemical modification

Fig. 4.4 summarizes a typical observation made on m-SWCNTs after oxidative ECM. The AFM image in Fig. 4.4(a) shows an individual metallic nanotube contacted underneath four separately addressable electrodes. After modification of the nanotube with **A** by applying a positive potential (+0.75 V vs. Pt for 120 s) on electrode 3, its height is homogeneously increased as can be seen from the AFM image in Fig. 4.4(b). The specific conditions used in the electrochemical modification resulted in a thickness increase of $\approx$3 nm, which is determined from the difference in the height profiles (Fig. 4.4(c)) taken along the lines marked in the AFM images between electrodes 3 and 4. The I-V curves measured between electrodes 3 and 4 are compared before and after ECM in Fig. 4.4(d). It is apparent that even though the nanotube is clearly coated with a layer of **A**, the initial resistance of 17kΩ is essentially preserved after modification.

The electrical transport studies were complemented by Raman spectra obtained using the confocal microscope on the same individual SWCNTs before and after ECM. In this case, the changes in the intensity and frequency of the RBM, D-line and G-line upon ECM were studied. Since the D-line intensity is sensitive to the introduction of defects within the nanotubes, we concentrated on the changes of this line. However, the absolute intensity of the D-line in the Raman spectra cannot be used directly for comparison, because the amount of light falling on the SWCNT can be different at different instances, due to the finite size of the diffraction-limited spot. Hence, we focussed on the effect

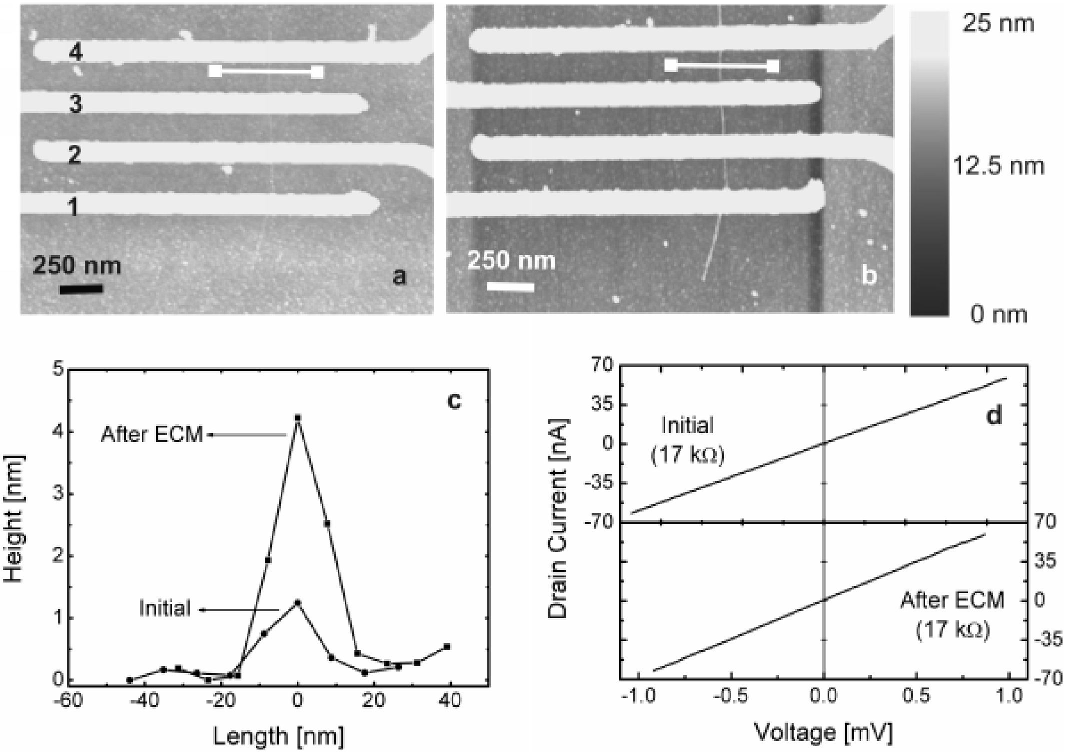

Figure 4.4: Oxidative ECM of an individual m-SWCNT with 4-aminobenzylamine (**A**): (a) AFM image of the SWCNT lying below the electrodes numbered 1 to 4 before ECM (b) AFM image of the same region after ECM with **A** on electrode 3 (+0.75 V vs. Pt, 120 s) (c) Comparison of the height of the SWCNT before and after ECM along the line marked in the AFM images (d) I-V curves of the m-SWCNT before and after ECM between electrodes 3 and 4.

of ECM on the relative intensity of the D-line with respect to the G-line to gain a qualitative measure of the structural disturbance of the SWCNTs. As explained in section 3.3 on page 39, confocal Raman images were recorded and used in connection with the corresponding AFM images to obtain Raman spectra from the same contacted SWCNT before and after ECM. Figs. 4.5(a) and (b) show respectively the AFM and confocal G-line Raman images of the same SWCNTs (-bundles) before ECM. Since the Raman image was obtained by excitation with 647.1 nm, at which wavelength the Carbolex m-SWCNTs are resonant, the visible objects correspond to either individual metallic nanotubes or bundles that contain at least one metallic nanotube. After ECM and topological characterization by AFM, the confocal Raman imaging was repeated and the spectra were taken at the same locations as before. The Raman spectra of the m-SWCNT marked "x" in Figs. 4.5(a) and (b) are compared before and after modification in Fig. 4.5(c). It is clearly observable that there is only a negligible change in the relative intensity of the G- and D-lines. Moreover, within the accuracy of the experimental setup, no shift in the Raman frequencies was observable.

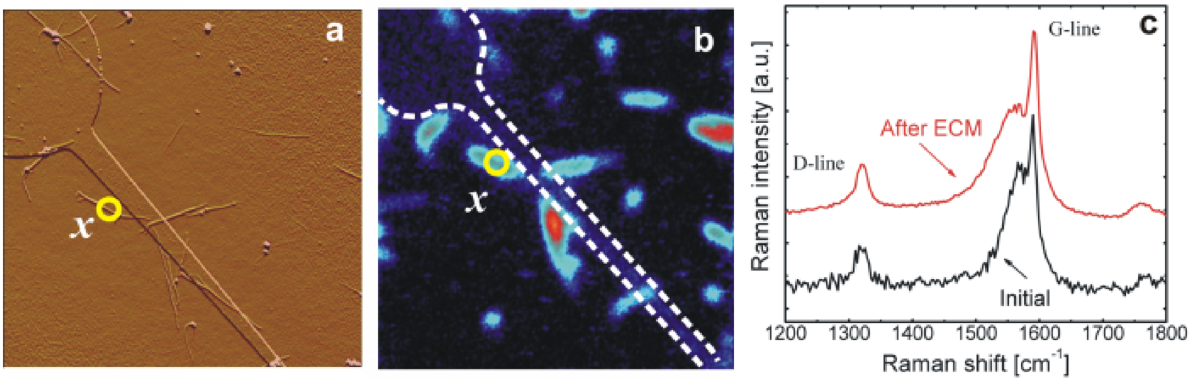

Figure 4.5: Characterization of m-SWCNTs modified by oxidative ECM through confocal Raman spectroscopy (a) AFM image of the sample showing an electrode and the SWCNTs (8 μm x 8 μm) (b) A confocal G-line Raman image (10 μm x 10 μm) of the same sample taken with an excitation wavelength of 647.1 nm. The electrode structure is drawn in white, the background appears dark blue and the SWCNTs appear as light blue to red regions. (c) Raman spectra showing the D-line and G-line of the SWCNT marked x before and after ECM. The changes in the intensity and shift in the frequency of these two features are negligible in this case.

The same series of measurements have also been carried out on semiconducting SWCNTs ($\lambda_{\text{exc}} = 514.5$ nm). Also in this case neither a change in the D- to G-line intensity ratio, nor a shift in the frequency could be observed. This is illustrated by Fig. 4.6(a), where the Raman spectra for the specific s-SWCNT shows no marked changes before and after ECM. However, the oxidative coupling of **A** to s-SWCNTs was found to increase the resistance. Fig, 4.6(b) shows the I-V curves before and after the deposition of a 4 nm thick layer on an individual s-SWCNT, which leads to a resistance change of the nanotube by one order of magnitude.

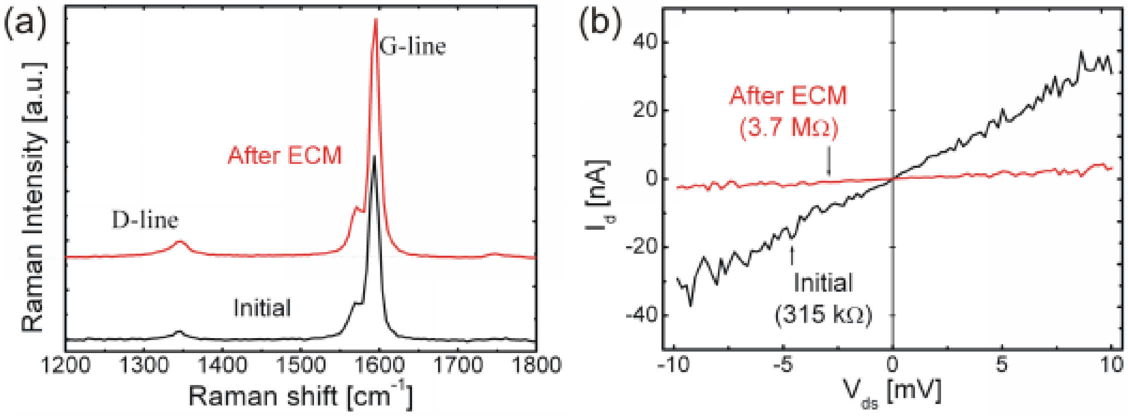

Figure 4.6: Oxidative ECM on s-SWCNTs: (a) Confocal Raman spectra of an individual s-SWCNT obtained at $\lambda_{\text{exc}} = 514.5$ nm before and after oxidative ECM with **A**. (b) I-V curves before and after ECM with **A** on an individual s-SWCNT.

4.2.3 Reductive electrochemical modification

A representative example of reductive ECM on SWCNTs is displayed in Fig. 4.7. The AFM image in Fig. 4.7(a) before ECM shows a series of bundles of SWCNTs contacted by an electrode. Upon ECM with **B** at a potential of −1.3 V versus Pt for 120 s, the nanotubes appear thicker as can be seen in the AFM image in Fig. 4.7(b). The line profiles along one of the contacted SWCNTs shows a height increase of around 3–4 nm (see Fig. 4.7(c)) resulting from the modification.

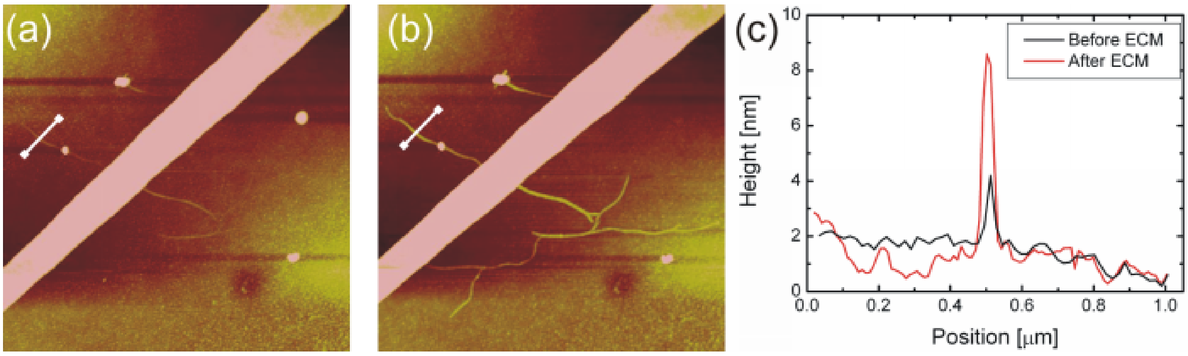

Figure 4.7: Reductive ECM on contacted SWCNTs: (a) AFM image of a number of bundles contacted by an electrode (b) AFM image of the sample after reductive ECM with **B** at −1.3 Vvs. Pt for 120s. (c) Line profiles from the height images of (a) and (b) along the white line.

Electrical transport measurements and confocal Raman spectroscopy were performed on individual SWCNTs before and after reductive ECM in a manner similar to that used for the characterisation of oxidatively modified samples. Fig. 4.8 summarizes the I-V curves and Raman spectra measured in this case. The I-V curves of an individual m-SWCNT and of an individual s-SWCNT are respectively shown in Figs. 4.8(a) and (b). In contrast to the electrical behavior of SWCNTs modified by **A**, the I-V curves of nanotubes modified by **B** show resistance increases of around three orders of magnitude. The confocal Raman spectra on individual tubes obtained at $\lambda_{\mathrm{exc}} = 647.1$ nm for m-SWCNTs and $\lambda_{\mathrm{exc}} = 514.5$ nm for s-SWCNTs are displayed in Figs. 4.8(b) and (d) respectively. It is clear that the relative intensity of the D-line is strongly increased upon chemical modification in both m- and s-SWCNTs. As control experiments, ECM was performed on selected SWCNTs in the pure electrolyte solution in the absence of **A** or **B**. In both cases, neither an increase in height nor a change in the resistance could be detected after modification.

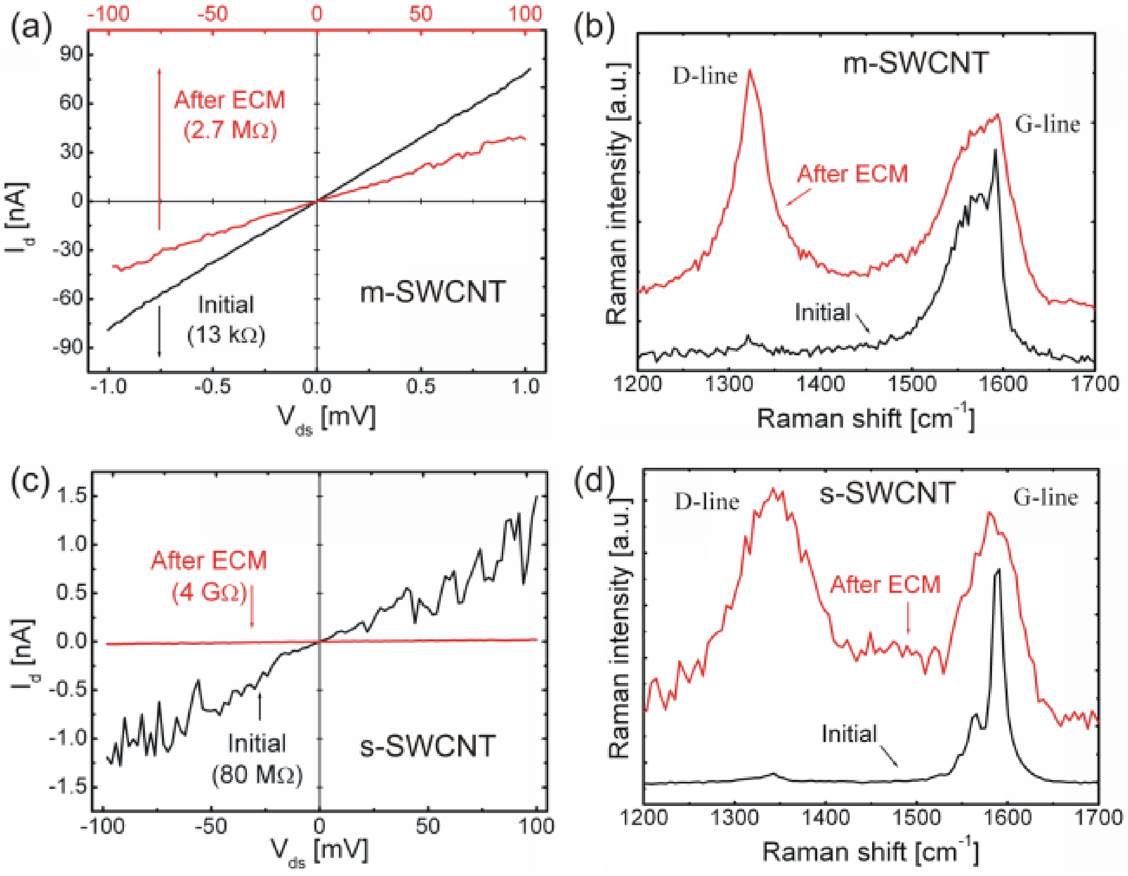

Figure 4.8: Characterization of SWCNTs modified by reductive ECM with **B**: (a) I-V curves of an individual m-SWCNT before and after reductive ECM. (b) Confocal Raman spectra of an individual m-SWCNT obtained using $\lambda_{\text{exc}} = 647.1$ nm before and after ECM. (c) I-V curves of an individual s-SWCNT before and after reductive coupling of **B**. (d) Raman spectra obtained on an individual s-SWCNT using a laser wavelength of $\lambda_{\text{exc}} = 514.5$ nm before and after ECM. The resistance is found to be higher upon ECM and the D-line is found to be stronger after the modification for both m-SWCNTs and s-SWCNTs.

4.2.4 Discussion

In order to obtain a more detailed overview of the effect of the two types of ECM on the various SWCNTs, a statistical analysis of the changes in the relative D-line intensities was carried out. For that purpose, we calculated the Raman intensity quotient by dividing the relative D-line intensities after and before ECM ($[I_D/I_G]^{\text{after}} \,/\, [I_D/I_G]^{\text{before}}$; where I_D and I_G are the intensities of the D-line and G-line respectively). For the sake of comparison, we have also analysed the intensity quotients of several non-contacted nanotubes, which have been exposed to the same chemicals without applying a potential. The resulting histograms are shown in Fig. 4.9. The intensity quotients of the non-contacted SWCNTs (Fig. 4.9(a)) had a mean value close to 1. For the SWCNTs modified by oxidative amine (**A**) coupling, a narrow distribution around a mean value of ≈1.5 was observed (see Fig. 4.9(b)). The reductive diazonium (**B**) coupling, in contrast, resulted

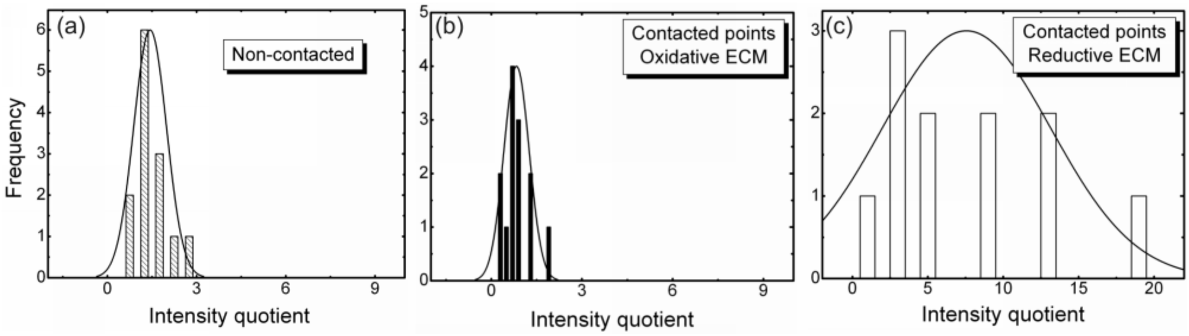

Figure 4.9: Statistical analysis of the relative Raman D-line intensities: A histogram of the intensity quotient (see text for details) for (a) non-contacted SWCNTs (b) contacted SWCNTs modified oxidatively by **A** and (c) contacted SWCNTs modified reductively by **B**.

in a broad distribution of intensity quotients, ranging between 1 and 20 centred around a mean value of ≈8 as shown in Fig. 4.9(c). Such a statistical analysis of the Raman D-line intensities gives additional confirmation that the diazonium modified SWCNTs show indeed a strong D-line relative to the G-line.

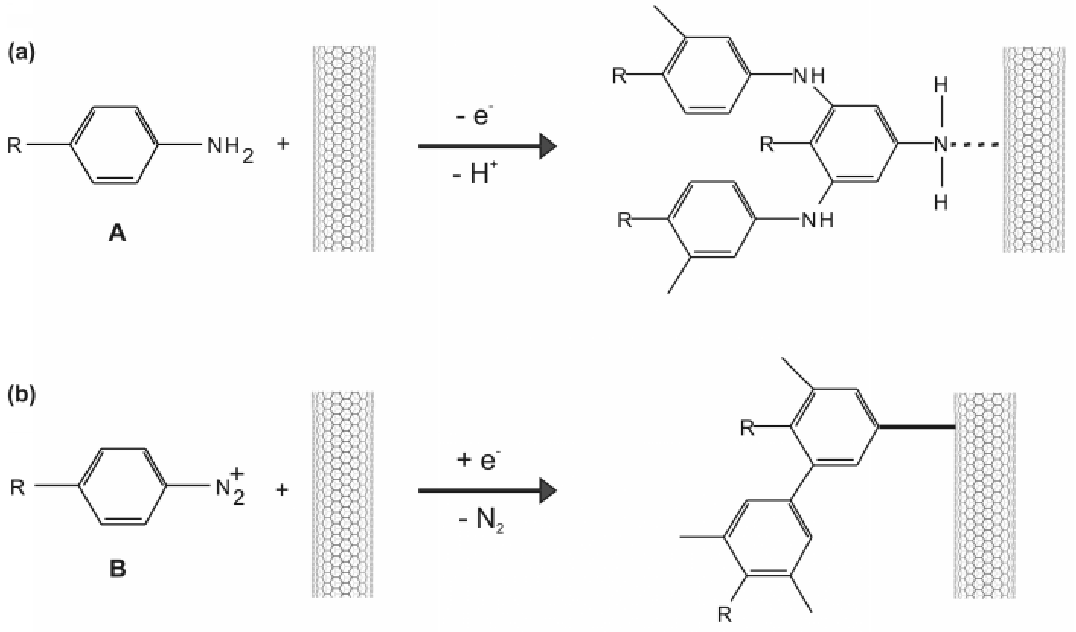

Figure 4.10: Reaction schemes for (a) oxidative ECM with **A** and (b) reductive ECM with **B** as inferred from the electrical transport and confocal Raman measurements. The broken line in (a) indicates the formation of electropolymerized layers of **A** on the SWCNT without the creation of a chemical bond. In case of ECM with **B**, the experimental data give a strong indication of the formation of a chemical bond with the nanotube (solid line).

In view of the results presented above, we conclude that upon oxidative ECM with **A** the SWCNTs remain electronically unchanged, which suggests that no bonds of the tube are broken upon modification. Hence, we conclude that the coating by the grafted films takes place via electropolymerization of the amine [96], without the formation of covalent bonds between the oxidatively created radicals and the nanotubes, as pictured in Fig. 4.10(a). In agreement with the preserved electrical properties, the unaffected Raman spectra of the modified m-SWCNTs reveal that no structural deterioration of the nanotube occurs under the oxidative grafting of the layers. The increase in resistance upon oxidative ECM of s-SWCNTs – which is not observed for the m-SWCNTs – can be explained by considering the fact that SWCNTs contacted by noble metal electrodes behave as *p*-type semiconductors [7] where the conductivity can be reduced by applying a positive gate voltage. Since the polymeric layer formed on the SWCNTs is positively charged as a consequence of charge transfer during ECM, the hole concentration should be decreased (corresponding *n*-type doping), which increases the nanotube resistance. Similar surface charge effects have been observed in sensors based on inorganic semiconductor nanowires [97].

In the case of reductive ECM with **B**, the pronounced increase of both the electrical resistance and the intensity of the D-line indicates that the reductively created phenyl radicals form covalent (C-C) bonds to the nanotube (see Fig. 4.10(b)), associated with the introduction of a sizeable density of sp^3-hybridized carbon atoms. The observed spread in the Raman intensity quotients may be explained by the fact that the reactivity of SWCNT side-walls decreases with increasing tube diameter [48, 98]. Accordingly, the diazonium-modified tubes that showed only minor changes in the D-line could belong to the largest diameter tubes within the present sample (d $\approx$ 1.3 nm).

4.3 Field-effect transistors through selective ECM

In contrast to the remarkable achievements made with devices based upon individual SWCNTs, the use of nanotubes in large-scale electronics is still facing severe limitations, which arise from the fact that all fabrication procedures developed to date yield mixtures of metallic and semiconducting tubes. In addition, the SWCNTs produced by bulk methods like the arc discharge or HiPco process are entangled in bundles. As a consequence, the electrical transport through such SWCNT ensembles is usually dominated by metallic pathways, and therefore only weak electric field effects on the conductance are attainable.

4.3.1 Motivation - Separation techniques

For the goal of fabrication nanotube FETs, two strategies have been followed to overcome this problem. In the first case, techniques have been devised to separate metallic nanotubes from semiconducting ones in solution, i.e. before they are adsorbed onto the substrate. Dispersing a SWCNT soot with octadecylamine (ODA) in tetrahydrofuran is expected to result in a physisorbed coating of ODA onto the sidewalls of s-SWCNTs due to the higher affinity of the latter to ODA [12]. The m-SWCNTs could then be separated by precipitation. In a similar experiment, SWCNTs have been dispersed with single stranded DNA yelding nanotubes wrapped with DNA molecules [15]. Anion exchange chromatography has been subsequently used to extract an enriched fraction of metallic tubes utililizing the difference in surface charge between the DNA-metallic and the DNA-semiconducting SWCNTs. Another method relies on the increased capability of charge-transfer complex formation by bromine with the m-SWCNTs, resulting in the ability to separate one type from the other just by using centrifugation [13]. Recently, it has been demonstrated that the varying dielectric constants of the metallic and semiconducting tubes could be utilized in separating the m-SWCNTs alone from a suspension through alternating current dielectrophoresis [14]. However, in all these cases, no quantitive separation could be achieved.

The second kind of strategy utilizes the fact that the s-SWCNTs can be turned to the insulating (*OFF*) state by applying a positive gate voltage. By ramping the drain-source voltage to sufficiently high potentials under the presence of oxygen, it is possible to burn off the metallic nanotubes [16]. This approach, which has until now successfully been applied to individual SWCNT bundles, has the disadvantage that the Joule heat produced in the m-SWCNTs may strongly affect adjacent s-SWCNTs.

4.3.2 Selective ECM on bundles of SWCNTs

In this work, a novel method has been designed to fabricate SWCNT-FETs in a generic manner, which extends the scope of the selective-destruction-approach. Specifically, ECM is used to eliminate the current carrying capability of the m-SWCNTs within an ensemble. As detailed in the previous section, this task is performed by electrochemically generating reactive phenyl radicals that are able to covalently attach in high densities to the nanotube sidewall, leading to an increase in resistance by several orders of magnitude. Selective reaction of the metallic tubes can be achieved after gate-induced switching of the s-SWCNTs to the *OFF* state. This results in a purely semiconducting SWCNT channel between source and drain electrodes. The major advantage of the electrochemical approach is the creation of a reactive species directly at the surface of the conducting tubes, which enables a highly localized functionalization.

The samples were fabricated using tubes from the HiPco process and contacted by AuPd electrodes on top in the 1.3 μm gap configuration. The density of tubes was chosen such that between 1 and 10 individual tubes or thin bundles connected the two

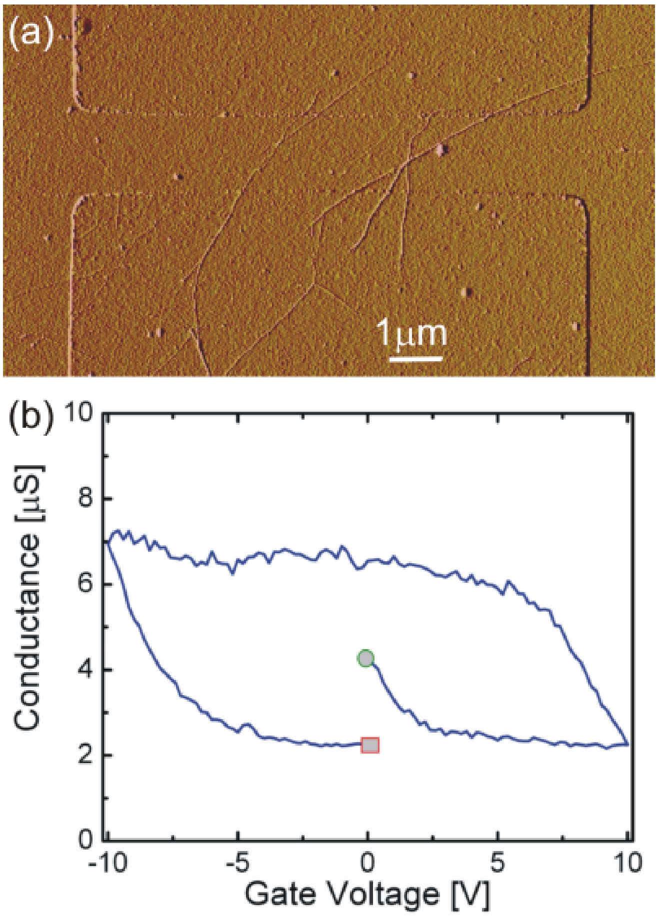

Figure 4.11: (a) AFM phase image of a typical sample used for selective ECM leading to the fabrication of a field-effect transistor. A number of SWCNT bundles can be found contacted between the electrodes with 1.3 μm separation. (b) Typical GDC curve from such a sample measured at $V_{\text{ds}} = 10$ mV. The curve exhibits a weak gate dependence in addition to a slight hysteresis both together strongly signifying the presence of a mixture of m-SWCNTs and s-SWCNTs.

electrodes. The samples could then be classified into three categories depending on their GDC: While m-SWCNTs displayed almost no GDC, s-SWCNTs exhibited GDC of at least four orders of magnitude A third set of samples showed a weak GDC with a small hysteresis characteristic of the presence of a mixture of both m-SWCNTs and s-SWCNTs contacted between the electrodes. An AFM amplitude image of the latter type of sample with the corresponding GDC curve is shown in Fig. 4.11. To selectively modify the metallic tubes by ECM, advantage has been taken of the hysteresis in the gate dependence in the following manner. After sweeping the gate potential to a positive value ($\geq +20$ V) and returning to zero, devices comprising of only s-SWCNTs were found to remain in the *ON* state. Similarly, the devices could be switched to the *OFF* state by sweeping the gate voltage to a negative value (≤ -20 V) and going back to zero. The stability of the *ON* or *OFF* state was found to be of the order of 10 to 15 minutes, sufficient to perform ECM with the semiconducting tubes in the *OFF* state without the need for in-situ gate control.

In order to optimize the parameters of the ECM (for e.g. the concentration of the diazonium salt, the magnitude and duration of the applied potential) with respect to maximal preservation of the semiconducting nanotubes, control studies were initially carried out with pure semiconducting and pure metallic tubes after gate tuning. It is noteworthy that in order to obtain reproducible results, the samples were heated at 100°C for 2 h immediately after ECM, to ensure removal of physisorbed solvent molecules. The application of -280 mV versus Pt for 30 s in a 10 mM 4-nitrobenzene diazonium salt (**B**) solution in N,N-dimethylformamide (DMF), with 0.1 M $LiClO_4$ as background electrolyte was found to cause only minor changes in the conductance of an individual semiconducting nanotube in the *OFF* state, as demonstrated by Fig. 4.12(a).

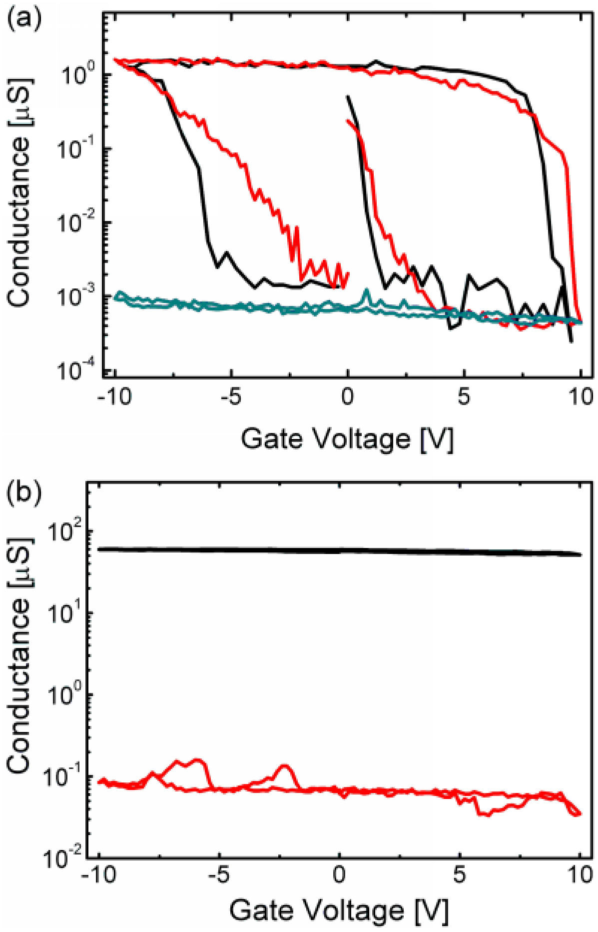

Figure 4.12: Room-temperature GDC curves of (a) a pure s-SWCNT: initial (black line), after *OFF* state ECM (red line) and after *ON* state ECM (blue line). (b) a m-SWCNT bundle: initial (black) and after *OFF* state ECM (red). The parameters of ECM were: -280 mV vs. Pt for 30 s in 10 mM **B**. $V_{\mathrm{ds}}$was 100 mV in (a) and 1 mV before ECM and 100 mV after ECM in (b).

Here the black curve is the initial gate dependence of conductance, while the red curve corresponds to the gate dependence after ECM in the *OFF* state. On the contrary, after subjecting the same semiconducting SWCNT in the *ON* state to ECM (blue line in Fig. 4.12(a)), the conductance reduced by four orders of magnitude for all gate voltages. To test whether the metallic SWCNTs are indeed modified under the *OFF* state conditions of the semiconducting tubes, the same parameters were applied to a purely metallic SWCNT bundle. In general, the modified metallic tubes showed a strong increase in resistance, as exemplified in Fig. 4.12(b) where the conductance is seen to drop by four orders of magnitude.

The same methodology was then applied to ensembles of SWCNTs containing a mixture of both m- and s-SWCNTs. For this purpose, a sample with few contacted bundles was taken. This bundle displayed a weak gate dependence of conductance, as apparent from Fig. 4.13 (black curve). After ECM in the *OFF* state, the bundle thickness was found to be slightly increased, which results from the formation of a molecular coating due to polymerisation of the electrochemically generated phenyl radicals at the SWCNT/electrolyte interface. Most strikingly, the gate dependence of conductance of the modified bundle (shown by the red line in Fig. 4.13) displays a significant increase in the *ON* to *OFF* ratio from 3 before modification to ≈10^6 afterwards. The shape of

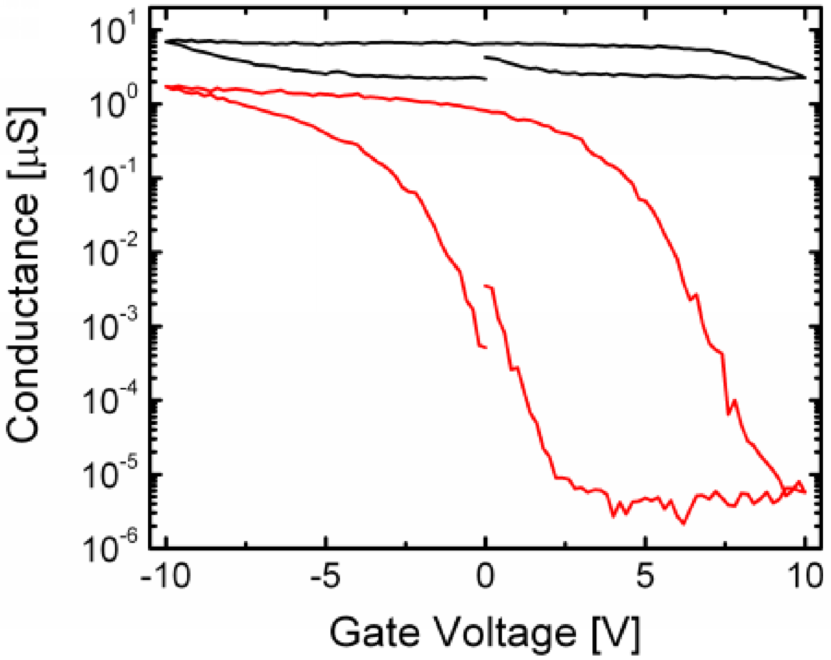

Figure 4.13: Creation of an FET through selective ECM of SWCNT bundles: Room-temperature GDC curves of the sample before ECM (black curve) showing a weak gate dependence (*ON*/*OFF* ratio) of 3, indicating the presence of both m-SWCNTs and s-SWCNTs. The red curve is obtained after *OFF* state ECM and the device now exhibits a switching ratio of 8 x 10^5. V_{ds} was 10 mV before ECM and 50 mV after ECM.

the curve after ECM, as well as the magnitude of the *ON* current, are comparable to those of the individual s-SWCNT shown in Fig. 3.6, indicating that the contribution of the m-SWCNTs to the transport has been completely eliminated and the device now acts as a purely semiconducting FET.

Since it has recently been reported that aromatic diazonium salts in aqueous solutions react selectively with metallic tubes under certain conditions [99], control experiments have been performed by exposing individual m- and s-SWCNTs to **B** separately in DMF and in water for up to 15 hours without applying a potential. This was followed by heating the sample to 100°C for 2 hours, again to remove physisorbed solvent molecules. Such a procedure did not introduce any changes in conductance for both types of tubes. Furthermore, the selective burn–off approach [16] was experimented on samples containing bundles of SWCNTs. Although this method has been successfully used to burn–off m-SWCNTs in an ensemble of individual SWCNTs (grown by CVD for e.g.), the procedure becomes complicated when extended to bundles, due to the fact that m-SWCNTs and s-SWCNTs lie very close to each other. Control experiments on such samples have indeed shown that the burn–off approach is less efficient in the elimination of m-SWCNTs in the bundle. One example of such an experiment is shown in Fig. 4.14. It is clear that even after repetitive burn–off cycles only a relatively low GDR of maximally two orders of magnitude could be attained.

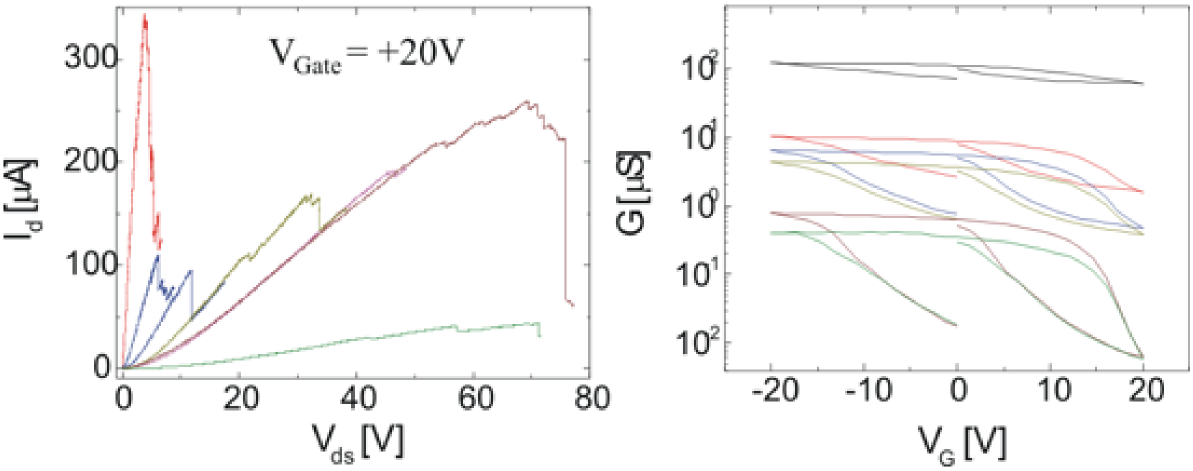

Figure 4.14: (Left) Application of a voltage ramp on an ensemble of SWCNTs with an applied gate voltage of +20 V with the aim of eliminating the m-SWCNTs in the bundle. This process was carried out in a sequence of steps, wherein in each step a the drain-source bias was ramped to a higher voltage. (Right) Gate dependence of conductance at room–temperature after each of the ramp step associated with appropriate colors (V_{ds}= 10 mV).

4.3.3 Selective ECM applied to nanotube networks

Although the present FETs likely contain more than one electrically active semiconducting tube, it is instructive to compare their device characteristics with those of single nanotube FETs. While the former exhibit a room temperature transconductance of ≈10 S/cm, values of up to 23 S/cm [100] are documented for the best single-tube FET until now. This difference can largely be attributed to the compact architecture of the latter devices, wherein a very thin gate oxide of ≈15 nm has been utilized. The switching ratio obtained in our devices is of the order of 10^6, similar to ratios obtained in other devices [11, 91]. The field–effect mobility using a classical FET model [101] is given by $\mu_{\mathrm{FE}} = (dG/dV_{\mathrm{G}})\,(L^2/C_{\mathrm{G}})$, where dG/dV_{G} is the slope of the GDC curve, L is the channel length and C_{G} is the gate capacitance. Assuming a model of a cylindrical conductor for the nanotube, the gate capacitance is given by $C_{\mathrm{G}} = 2\pi\epsilon_0\epsilon_r L/ln\,(2h/r)$, where ϵ_r is the dielectric constant of the insulating $\mathrm{SiO_2}$ (2.5), h is the thickness of the gate oxide and r is the radius of the nanotube. In this manner, the maximum hole mobility is found to be ≈1000 $\mathrm{cm^2/Vs}$ at room temperature for the ECM-based FETs, whereas the best device fabricated [10] using single nanotubes showed a mobility of 9000 $\mathrm{cm^2/Vs}$. The higher mobility in the latter case is suggestive of the superior structural quality of SWCNTs grown from solid-supported catalyst particles via chemical vapor deposition (CVD).

Towards optimization of the device performance, a number of steps could be undertaken. The field-effect mobilitiy in FETs is proportional to the length of the channel that is used. For this purpose, the electrode spacing could be increased. The transconductance of a device is a measure of the speed with which the device can work. A higher value of transconductance corresponds to a higher value of *ON* current. This could be attained by increasing the number of channels connecting the source and drain electrodes. In other words, the use of dense networks should in principle result in a higher number of contacted s-SWCNTs and thereby provide a higher *ON* current. An example of such a sample and the resulting field-effect characteristics after selective ECM are displayed in Fig. 4.15. This sample was fabricated using HiPco tubes with AuPd/Ti electrodes. Although it is apparent that field-effect switching can be achieved in these samples, the *ON* current is still of the same order of magnitude as in the case of FETs with a few bundles. This is due to the presence of Ti in the contacting electrodes, which increases the contact resistance. Further investigations on the effect of the contacting metal, the density of networks and the type of SWCNT raw material are under progress.

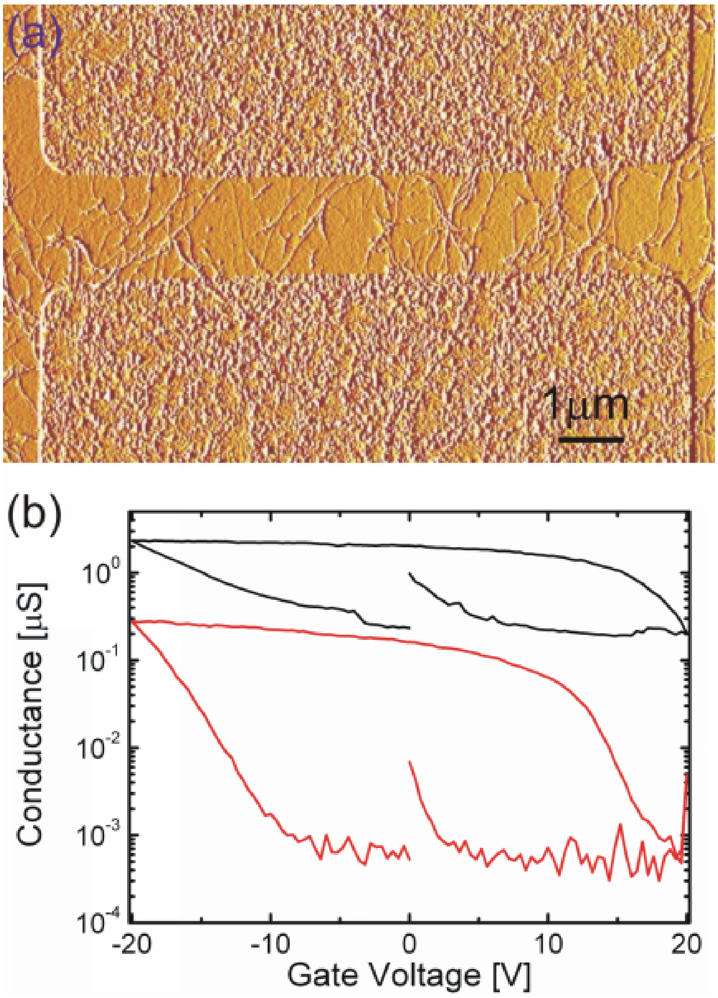

Figure 4.15: Fabrication of an EC-FET using nanotube networks: (a) AFM amplitude image of a sample with electrodes contacting a network of SWCNTs. The electrodes are AuPd/Ti. (b) GDC curves before (black curve) and after (red curve) after *OFF* state ECM. V_{ds} is 10 mV before ECM and 50 mV after ECM.

4.4 Outlook

Electrochemical modification of individual SWCNTs has been developed into a versatile tool for the attachment of desired functional moieties in a covalent or non-covalent manner. By appropriate choice of the precursor, a spectrum of different molecules ranging from simple substituted aromatic rings to larger supramolecular structures could be attached to the SWCNTs. Although, the simultaneous use of room-temperature electronic transport measurements and confocal Raman microscopy has provided insights into the coupling mechanism, more experiments are needed to understand the effect of such an attachment on the electronic structure of the nanotubes. Electrochemical STM investigations and low-temperature transport measurements could be used to for this purpose. The former method could deliver information on the distribution of functional groups on tubes with sub-monolayer coatings.

On the other hand, from an application point of view, ECM is an elegant tool for the fabrication of nano-scale electronic devices, as has been demonstrated in this work by the selective electrochemical functionalization of m-SWCNTs contained within a nanotube network. ECM is also promising for the fabrication of chemical sensors. Due to their large surface to volume ratio, individual pristine nanotubes show high sensitivites for certain gases at room temperature [102]. However, for the detection of molecules that are only weakly adsorbed (e.g. carbon monoxide and hydrogen), the change in resistance is often too small. A possible workaround is accomplished by the modification of the nanotube sidewalls through nanoparticles made of a suitable metal. For instance, sensitive hydrogen sensors operating at room temperature have been fabricated via electro-deposition of palladium nanoparticles [3]. Individual SWCNTs modified electrochemically by appropriate functional groups are also attractive for detecting ions (pH) in aqueous solutions. One strategy that could be employed here is the introduction of covalently bonded molecules containing pH-sensitive groups. The moieties introduced in such a manner may behave as pH-dependent scattering sites, so that the resistance of the nanotube would be a direct indicator of the pH of the solution. Future studies could also involve the attachment of ligand- or receptorlike functionalities that offers the potential of producing nanowires that are compatible with biological structural motifs for applications such as the contacting of nerve cells on a solid support.

Chapter 5

Photoelectronic transport properties of individual nanotubes

SWCNTs are evolving to be a promising candidate as components of nano-scale electronic devices. Towards fabrication of such molecular electronics devices, a detailed understanding of the electronic transport through SWCNTs is essential. The effect of the environment, the type of the contacts, the presence of structural inhomogeneities as well as the type of raw material used all have a crucial impact on the electronic transport behaviour of the nanotubes. A complete understanding of the influence of these factors on the electrical properties of SWCNTs is, however, still in its infancy. While various techniques have been utilized in the study of the transport properties in dark, much less is known about their photoelectronic transport (PET) properties. The investigation of electronic transport under the influence of photo-illumination helps in understanding these effects to a great extent. Thus a study of the PET properties of individual nanotubes has important implications for future nano-scale optoelectronic and photovoltaic devices. This chapter starts with a short description of the current status of investigations on photoelectronic transport in SWCNTs. This is followed by a short sketch of the two experimental setups that have been used during this work. Subsequently the PET investigations on individual s-SWCNTs and m-SWCNTs are presented separately and the chapter concludes with an outlook of potential future experiments.

5.1 Photoelectronic transport – Background

The first ever experiments on the PET properties of SWCNTs were performed by Fujiwara *et al.* [18], who used thin films of SWCNT bundles obtained from the arc discharge process. The thickness of the films ranged from 300 to 500 nm and were contacted directly by gold electrodes separated 10 μm apart. The whole sample was illuminated with a pulsed laser whose energy could be tuned in the range of 0.5 eV to 2.8 eV. The photocurrent at room temperature showed two strong peaks for excitation at 0.7 eV and 1.2 eV, in agreement with the first two interband transitions E^s_{11} and E^s_{22} for arc-discharge tubes having a diameter of $\approx$ 1.4 nm. The effect of the presence of other metallic tubes in such a film was not discussed here, probably because the fraction of s-SWCNTs in the film was quite high due to the sharp diameter distribution of these samples. In another experiment with SWCNT films of similar thickness and electrode spacings varying from 15 to 300 μm, photoconductivity could be observed at near infra-red wavelengths corresponding to an energy of $\approx$ 1.46 eV [103]. The diameters of the SWCNTs were however in a broader range of 0.8 to 1.1 nm. The samples exhibited a slow response of the photocurrent towards illumination, which they attributed to the sorption of oxygen onto the SWCNT films.

The mechanism of photoconductivity observed in the above experiments was not really clear due to the investigation of a mixture containing both m-SWCNTs and s-SWCNTs. The PET properties of an individual s-SWCNT was first studied by Chen *et al.* [42], who used a CVD–grown tube with a diameter of 1.5 nm and contacted by electrodes spaced by $\approx$1.5 μm. An ultraviolet (UV) light source with a wavelength of $\lambda_{\mathrm{exc}} = 254$ nm (4.9 eV) and a low power intensity of 2 mW/cm^2 was utilized here. A *decrease* in conductance was observed upon global illumination of these samples, which was traced back to photoinduced desorption of oxygen from the surface of the s-SWCNT. It has been shown previously that under ambient conditions, oxygen adsorbs onto the SWCNTs and dopes them by withdrawing one tenth of an electron per oxygen molecule [104, 105], as a result of which s-SWCNTs behave as p-type semiconductors in air. Under UV illumination, oxygen photodesorption causes a reduction of hole carriers, thus lowering the sample conductance. Furthermore, the high energy of illumination (4.9 eV) is quite close to the work function of the s-SWCNT ($\approx$ 5 eV for a s-SWCNTof diameter 1.5 nm), as obtained by first principles calculations [106]. Thus, the photoexcited electrons have a high probability of inducing such a desorption process. A wavelength dependence of this photoeffect indicated that photodesorption is maximum at high energies and reduces drastically when moving down to lower excitation energies. They also observed such a phenomenon using a SWCNT film sample. Ruling out the possibility of photocurrent generation, they attributed photoinduced excitation of plasmons as the cause for the photodesorption of adsorbed molecules. There appear two plausible reasons why photoconductivity could not be observed in this experiment. The first one probably relates to the chosen wavelength where molecular photodesorption effects are dominant. The second reason could be the illumination of the sample at a high current state of the s-SWCNT. At $V_G = 0$ V, the s-SWCNT was in its high conductance state. In such a situation, the holes in the valence band contribute to the flow of current through the device. The photoinduced carriers then form only a small fraction of the current-carrying holes and hence it was not possible to measure the photogenerated current in this experiment.

Incorporating this aspect and switching the device to the low conductance or *OFF* state, it was indeed possible to measure true photoconductivity through an individual s-SWCNT [21]. Here, the ambipolar device comprised of an individual s-SWCNT of diameter $\approx$ 1.3 nm obtained using the laser ablation procedure. The electrodes were made of Ti spaced $\approx$ 800 nm apart and the device was protected from the effect of surroundings by a 10 nm SiO_2 layer. The s-SWCNT was also illuminated globally using a laser tunable in the energy range of 1.27 to 1.59 eV and a maximum power intensity of 10 kW/cm^2. The photocurrent showed a linear dependence on the power intensity and was maximum for the polarization of light being parallel to the orientation of the tube. At 0.6 V, $\approx$ 3pA/(kW/cm^2) of photocurrent could be observed corresponding to a photoconductance of $\approx$ 5pS/(kW/cm^2). The authors proposed a mechanism wherein the incident infrared light excited the second exciton state E_{22}^s of the s-SWCNT followed by the decay of the excited state to an electron hole pair at the band edge which then drifts under application of an electric field. Although this experiment enabled the observation of photoconductivity the local origin of the generation of the photocurrent could not be explored. The experiments performed in this work show for the first time the effect of localized photo-excitation on the electronic transport through individual SWCNTs.

5.2 Instrumentation

The heart of the experimental setup comprises of a focussed laser beam from the confocal microscope (refer to section 3.3) to enable local illumination of an individual SWCNT. This setup has been coupled with the arrangement for electronic transport measurement, which in turn facilitates the investigation of photoinduced electronic transport at a local scale. A block diagram of the measurement setup is displayed in Fig. 5.1. The relatively small extension of the laser spot opens up the possibility to record the photocurrent signal that originates from illumination at different locations along a contacted SWCNT. When this photocurrent is plotted as a function of position, an image of the photocurrent similar to a confocal reflection or Raman image is obtained. This image is termed as a

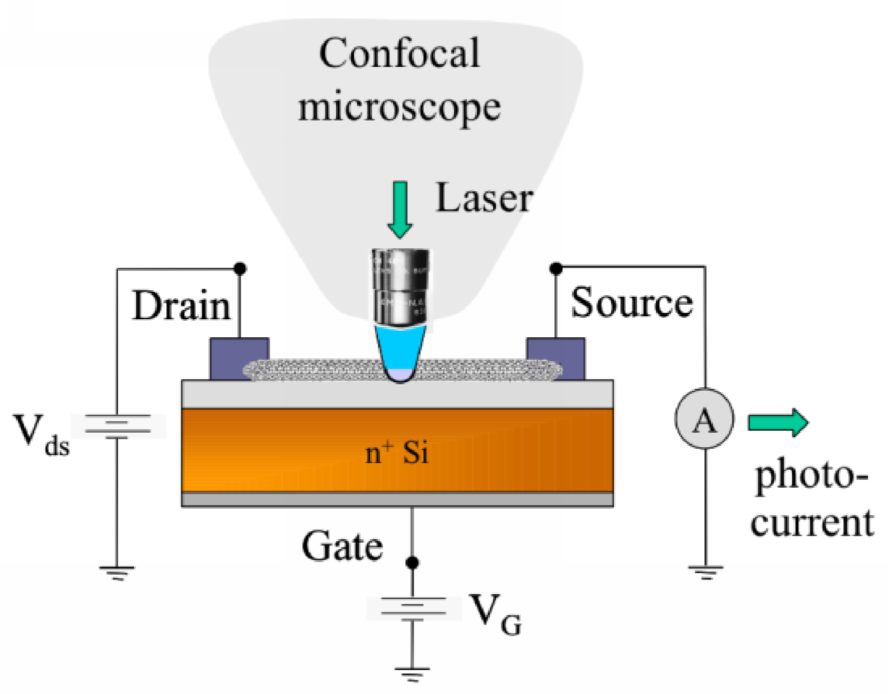

Figure 5.1: A simplified view of the setup used for investigation of photoelectronic properties of individual SWCNTs. The nanotube is locally illuminated by a diffraction-limited spot from a confocal laser microscope and the electronic transport through the nanotube is investigated simultaneously.

photoelectronic transport image (PETI) and gives valuable information about the origin of the photocurrent. Two different microscopes have been used for this purpose in this work. The details of these two arrangements are presented in the following.

5.2.1 Inverted Zeiss confocal microscope

The first setup was an extension of the confocal Raman microscope that is described in section 3.3. Initially, one could investigate just bare samples by mounting them below the objective of the microscope. During the course of this work, an additional capability of mounting a bonded chip containing a contacted SWCNT was added to this microscope. As a result of this, objectives with longer working distances different from the one used normally for confocal Raman imaging had to be introduced. Specifically, two different objectives – one with a magnification of 50X and NA of 0.6 and the other with a magnification of 10X and an NA of 0.25 were used. The voltage $V_{\rm ds}$ was supplied from a voltage source and the current $I_{\rm d}$ through the device measured by an electrometer. The gate voltage $V_{\rm G}$ could be controlled through a second voltage source. The electrometer had the capability of outputing an analog channel containing a scaled value of the measured current. This output was then directly fed into a free input channel of the controller for the XY piezo scanner. In this manner, it was possible to acquire confocal reflection, confocal Raman and PET images simultaneously with one-to-one spatial correspondence between the three images. The ability to acquire these images parallely is essential to distinguish the orgin of photocurrent as coming from different regions along the individual SWCNTs. Additionally, the use of the motorized polarizer was helpful in the measurement of the photoinduced current as a function of the polarization of the incident light. Furthermore, the microscope was fit with a special arrangement to measure the photoresponse in various environments like in oxygen, water vapor or argon. For this purpose, the desired gas was led through a thin covering around the objective that focussed the gas onto the sample that eventually flooded the whole surroundings of the nanotube with the gas that was fed in.

5.2.2 Leica confocal microscope

The need for the performance of PET measurements on a routine basis led to the construction of a second setup based on a commercially available confocal scanning laser microscope (Leica TCS SP2). In this microscope, the laser beam scans with the sample being kept in a fixed position. The TCS SP2 is used mainly for fluorescence imaging with an in-built prism for dispersing the scattered light, followed by the use of a mechanical shutter to allow light of a desired wavelength to pass through. The detector is a photo-multiplier tube (PMT). Up to two channels of different wavelength regions can be acquired with the aid of the ready-to-use microscope. The TCS SP2 has three different laser sources and one of the 6 different laser lines (458 nm, 476 nm, 514 nm, 532 nm, 568 nm, 633 nm) or a combination of them can be selected as the source of excitation. Due to the analog scanning mechanism of the mirrors in the microscope, it cannot be directly used to acquire images. To accomplish this, an external piezo scanner had to be integrated into the system. The sample containing the contacted SWCNT was mounted onto this piezo scanner and connected to an electronic transport measurement system similar to the one described in section 3.2. Images could be acquired by keeping the scanning mirrors at a fixed position, displacing the sample relative to the focal spot and recording the photocurrent as a function of position. The versatility of this system has delivered the possibility of routine PET imaging with the ability to obtain a quasi-wavelength dependence of the photocurrent using a quick sequential switch of the 6 different laser lines.

5.3 Photoelectronic transport in semiconducting SWCNTs

The electronic transport through s-SWCNTs under photo-illumination has been found to be strongly influenced by the type of metal that is used to contact them. When using pure AuPd, the contact is more ohmic and the band alignment between the SWCNT and the metal leads is roughly mid-gap. The use of Ti as an adhesion layer on top of the SWCNTs produces a pronounced Schottky barrier at the contact, but imparts a smaller sensitivity to the surroundings. By contrast, the thickness of the thermally grown SiO_2 layer that serves as the gate insulator has only a negligible effect on the photoelectronic transport through individual SWCNTs. In the following, the observation of photoconductivity in individual SWCNTs using a focussed beam of visible laser light is presented. Then, the use of PET imaging to identify the local origin of photoconductivity and the effect of Schottky barriers at the contacts is described. The observations reported here concern only the devices containing arc-dicharge SWCNTs contacted by AuPd/Ti electrodes.

5.3.1 Photoconductivity in s-SWCNTs

Individual s-SWCNTs were identified with the help of AFM height images and their strong gate dependence of conductance. In total, 12 different s-SWCNT devices were investigated in this work and all of them exhibited p-type behavior with a GDR exceeding 10^3 in a V_G range of ± 5 V. A representative example of such a device is depicted in Fig. 5.2. Fig. 5.2(a) shows an AFM amplitude image with a single s-SWCNT contacted between the two electrodes. The GDC curve for this device is shown in Fig. 5.2(b), which displays a GDR of $\approx 10^4$ and a pronounced hysteresis. A confocal Raman image of the G-line intensity, acquired using the green line ($\lambda_{exc} = 514.5$ nm, 0.5 MW/cm^2) overlaid above a simultaneously acquired reflection image is shown in Fig. 5.2(c). The combination of the reflection image and the Raman image helps in identifying the exact location of the contacted s-SWCNT, which subsequently enables positioning of the incident laser spot exactly above the specific SWCNT bridging the electrode gap. A Raman spectrum of this s-SWCNT could then be obtained, which is displayed in Fig. 5.2(d). The Raman spectrum ensures additionally that this tube is semiconducting, as is apparent from the absence of the BWF line characteristic of m-SWCNTs.

Before performing the PET experiments, the devices were switched to the *OFF* state by performing one full gate voltage cycle. Specifically, the gate voltage is scanned to

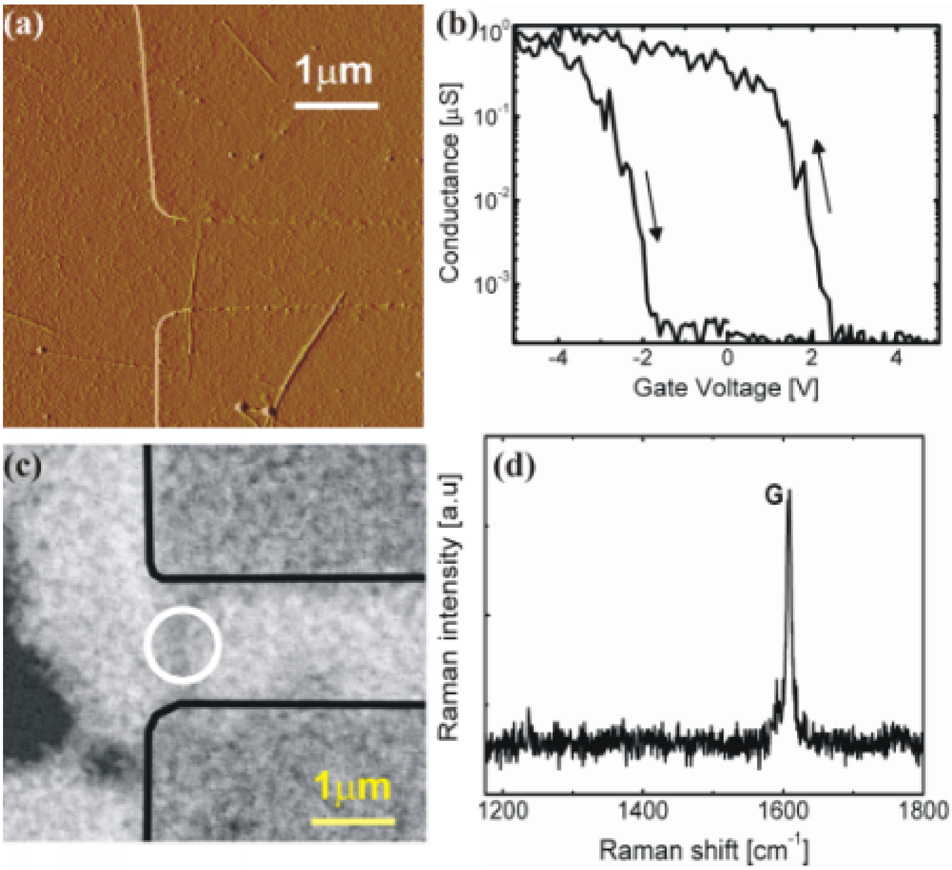

Figure 5.2: Locating an individual s-SWCNT for PET measurements: (a) AFM amplitude image of a device comprising a single s-SWCNT (height ≈ 1.3±0.3 nm). (b) Gate dependence of conductance for the same sample with $V_{\mathrm{ds}} = 0.1$ V. The arrows indicate the direction in which V_{G} is scanned. (c) False color Raman G-line image of the sample ($\lambda_{\mathrm{exc}} = 514.5$ nm, 0.5 MW/cm^2), overlaid with a reflection image to obtain the position of electrodes. (d) Raman spectrum of the s-SWCNT taken with the laser spot positioned at the marked region (circle) of (c).

negative voltages and brought back to zero. Due to the hysteresis present in the device, after the performance of this scan, the device remained in the *OFF* state long enough to perform the subsequent measurements. Using the technique outlined in Fig. 5.2, the laser spot was positioned over the tube approximately in the middle of the gap. By using a manual shutter in the laser beam path, the effect of photo-illumination on the current through the tube could be monitored for short laser pulses of intensities varying in the range of 0.5 to 7.5 MW/cm^2. A result of such a measurement is shown in Fig. 5.3(a). It can be observed that the photoresponse is instantaneous within the limits of the measurement speed used. The measured photocurrents are plotted as a function of the incident laser intensity in Fig. 5.3(b), exhibiting a quasi-linear power dependence of the photogenerated current. The slope of the linear fit has been determined to be 0.2 nA/(MW/cm^2) or equivalently 2nS/(MW/cm^2), comparable to the photoresponse

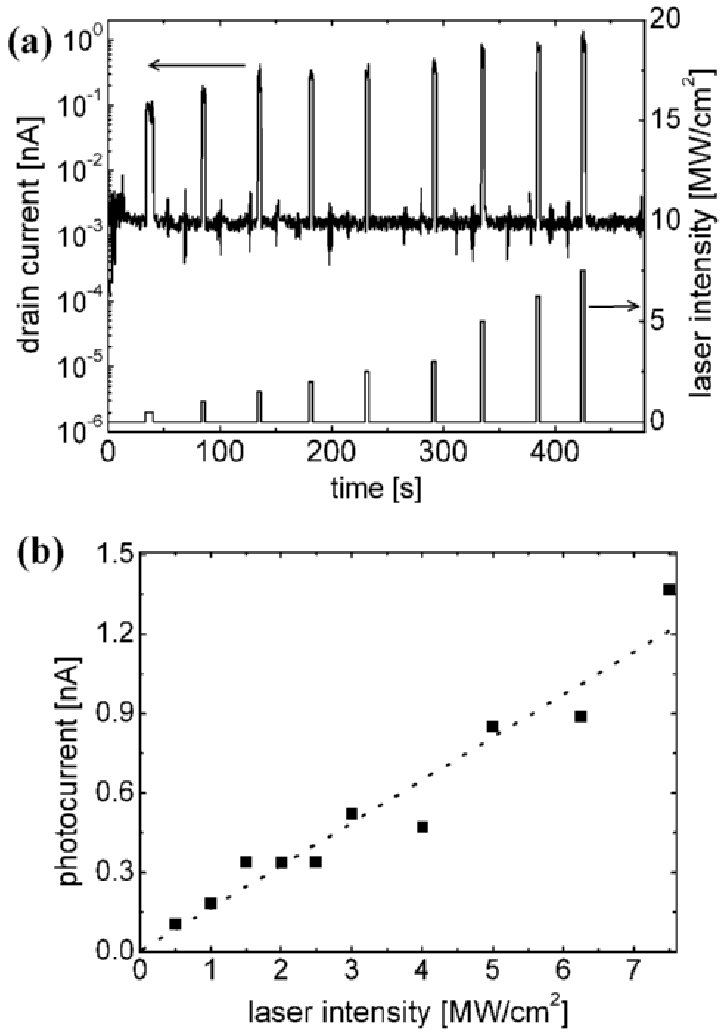

Figure 5.3: Photoconductivity in individual s-SWCNTs: (a) Room temperature currents (plotted in log scale) measured on a single s-SWCNT (V_{ds} = 0.1 V) upon illumination with various laser intensities (λ_{exc} = 514.5 nm) and shutter pulse widths of 3 or 7 s. (b) Dependence of the photogenerated current in (a) plotted as a function of laser intensity. The dotted straight line is a linear fit to the measurement data.

of 3pS/(kW/cm^2) obtained in previous experiments [21]. Noteworthy are the laser intensities used in the present work that fall into the range of 0.5–7.5 MW/cm^2, which is approximately three orders of magnitude larger than that used in Ref. [21].

The linear dependence of the photocurrent on the incident laser intensity is indicative of photogenerated charge carriers in the nanotube being responsible for the current increase. At the high laser intensities and small bias voltages ($\leq$ 0.1 V) used in this work, no alteration in photocurrent was observed when the environment was changed from air to argon, oxygen or water vapor. This result, taken in connection with the use of the green laser line (λ_{exc} = 514.5 nm) as the excitation source supports that the photocurrent does not result from photodesorption [42] of adsorbates like oxygen [31, 104] or water [76], which have been reported to affect the electrical properties of s-

SWCNTs. Furthermore, the photocurrents were one order of magnitude smaller when the samples were illuminated by λ_{exc} = 647.1 nm, as compared to excitation with λ_{exc} = 514.5 nm with the same laser intensity (0.5 MW/cm^2). This difference is expected since the absorption cross-section of the s-SWCNTs is much higher at 514.5 nm, in accordance with the semiconducting interband transitions corresponding to the third van Hove singularties (E_{33}^s) falling close to 2.41 eV for a nanotube with a diameter of $\approx$ 1.3 nm.

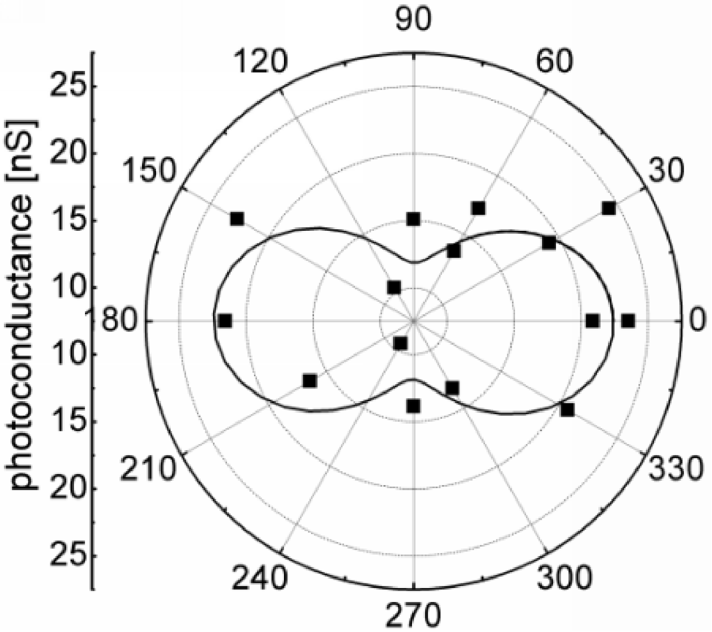

Figure 5.4: Polarization dependence of the photoconductance of a single s-SWCNT under illumination (λ_{exc} = 514.5 nm, 2 MW/cm^2, V_{ds} = 0.1 V).

To gain additional support that optically excited charge carriers in the s-SWCNT are the origin of the current changes observed under illumination, the dependence of photocurrent on the polarization direction of the incident light was studied. The polar plot in Fig. 5.4 illustrates the result of such a measurement, where 0° corresponds to the direction of polarization being parallel to the nanotube axis. It shows clearly that the photocurrent is maximum when the polarization of the incident light is along the tube axis. For the present sample, a polarization ratio of approximately 5:1 is found. The polarization dependence of the photoconductance excludes that photovoltages created at the n^+-Si/SiO$_2$ interface are responsible for the observed current changes.

The effect of the gate voltage on the photocurrent was also investigated during this work, albeit the presence of hysteresis in these samples greatly complicating the interpretation of the obtained results. However, a comparison of the GDC curves in dark and under photo-illumination does give some additional insight into the mechanism of the photocurrent generation, when the gate voltage sweeps performed in only one direction are considered (from $V_G = -10$ V to $V_G = +10$ V). A representative example of such GDC curves obtained with an arc-discharge (Carbolex) sample using both the wavelengths ($\lambda_{\text{exc}} = 647.1$ nm and $\lambda_{\text{exc}} = 514.5$ nm) is displayed in Fig. 5.5. The plots convey a multitude of information. Firstly, the s-SWCNT device exhibits a slightly ambipolar behavior in the dark. Unless specifically treated, for e.g. by annealing [91], as grown s-SWCNT devices exhibit principally a p-type behavior. However, the GDC curves shown in Fig. 5.5 have been obtained after some initial investigations on the sample with the laser beam turned on. Upon photoillumination using such high laser intensities it is very likely that adsorbates like oxygen present on the s-SWCNT are easily desorbed [42], leading to ambipolar transport in the s-SWCNT. When the laser beam is switched off, the desorbed molecules tend to readsorb onto the substrate and the p-type behavior is slowly restored. The GDC curves in the dark shown in Fig. 5.5 correspond to an intermediate state between the ambipolar and p-type behaviour. Secondly, a sizeable photocurrent that is distinguishable from the dark current is only observed for those gate voltages where the s-SWCNT remains in the *OFF* state. Finally, as mentioned before, the photocurrent with $\lambda_{\text{exc}} = 514.5$ nm is one order of magnitude larger than that with a laser wavelength of 647.1 nm, due to the higher optical absorption of this arc-discharge (Carbolex) s-SWCNT at the former wavelength.

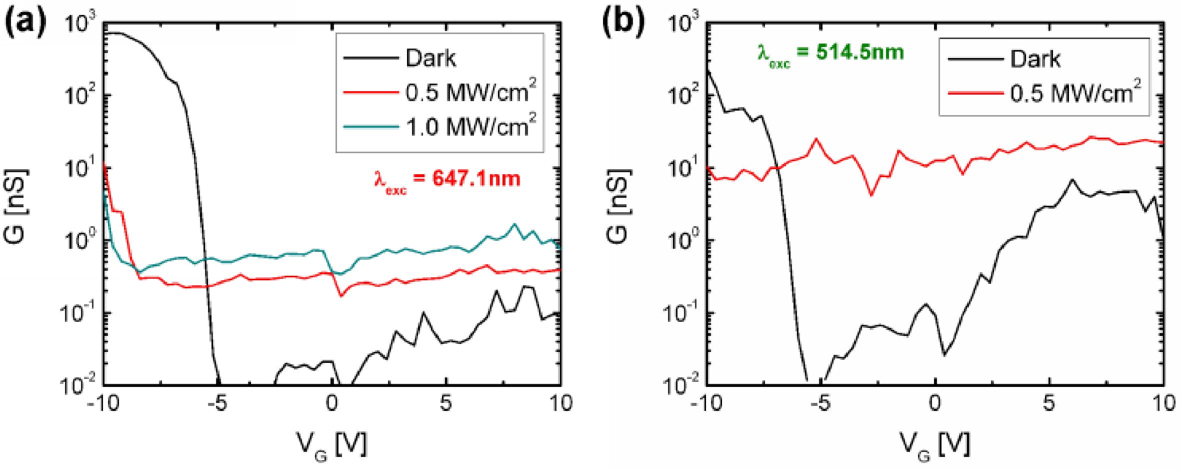

Figure 5.5: Gate dependence of conductance curves of a s-SWCNT device with and without illumination at (a) $\lambda_{\text{exc}} = 647.1$ nm and (b) $\lambda_{\text{exc}} = 514.5$ nm.

5.3.2 Effect of Schottky barriers

To obtain information about the local photoelectronic properties, PET images were obtained on individual s-SWCNTs. A representative PET image of the sample in Fig. 5.2

is presented in Fig. 5.6. In order to highlight the electrode positions, the PET image has been overlaid over a simultaneously taken reflection image. It is apparent that the magnitude of the photocurrent is strongest closest to the upper electrode. This observation is attributed to the generation of an offset photovoltage upon illumination of the Schottky barrier at the contact region. With increasing distance from the contact, the flat band region is reached where the major effect is photogeneration of carriers that experience a much weaker field. Similar observations have been also made on other samples. The absence of a corresponding photocurrent peak close to the other electrode may be explained by the Schottky barrier at the source contact being asymmetric to that at the drain contact.

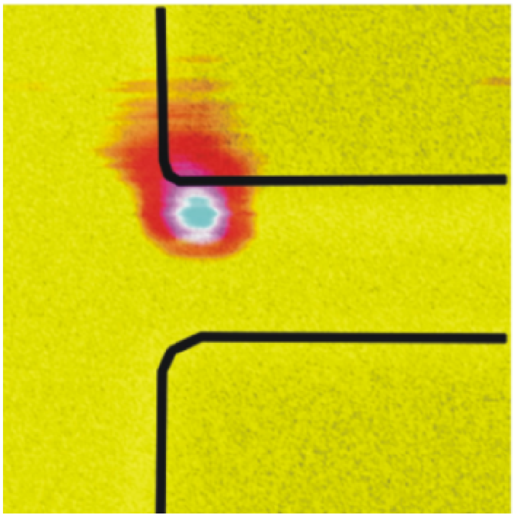

Figure 5.6: Photoelectronic transport image (PETI) of the sample in Fig. 5.2 with a bias voltage of 0.1 V (λ_{exc} = 514.5 nm, 0.5 MW/cm^2). A simultaneously taken reflection image is overlaid to obtain the approximate position of the electrodes, which are shown as black lines. A maximum photocurrent of 0.11 nA is observed at the bright spot close to the upper electrode. The current is maximum at the cyan colored region and goes gradually down to a minimum in the yellow colored region.

Using the results obtained from the experiments described above, a simple model of the photoelectronic transport through s-SWCNTs can be derived, as sketched in Fig. 5.7. Upon bringing the s-SWCNT in contact with the metal (Ti in this case) due to the difference in their work functions charge transfer takes place and the semiconducor band edges are bent leading to the formation of a Schottky barrier. Since the work function of Ti is smaller than that of the s-SWCNT, the band bending is downwards. On the left side of Fig. 5.7(a), the situation is depicted when the flat band region is illuminated by the laser spot under simultaneous application of the bias voltage, while on the right side, the resulting I-V curve is schematically displayed. Under these conditions, electron-hole pairs are created by the incident laser light which relax to the

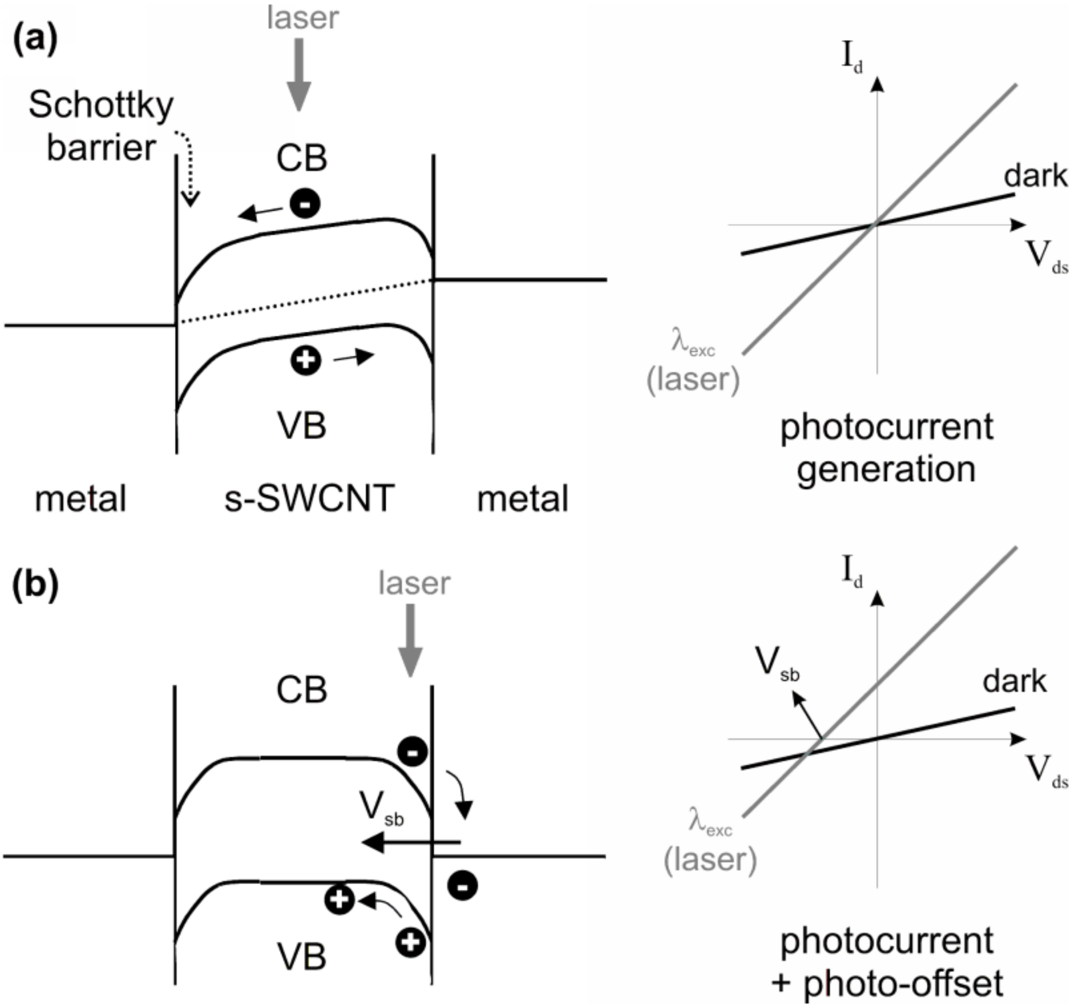

Figure 5.7: A simplified model of photoelectronic transport through s-SWCNTs: (a) Left: Illumination of the s-SWCNT in the middle of the electrode gap leads to the generation of electron-hole pairs which result in a photocurrent upon application of a drain-source bias. Right: Schematic I-V curves showing the dark current and the photocurrent. (b) Left: Photoillumination of the contact region results in the generation of an additional offset voltage (V_{sb}) due to the presence of a Schottky barrier there. Right: Corresponding I-V curves in dark and upon photoillumination showing clearly the photogenerated offset in addition to the photocurrent. Note that for the sake of clarity the band structure in (a) is at $V_{\mathrm{ds}} \neq 0$, while that in (b) is depicted for $V_{\mathrm{ds}} = 0$. CB stands for conduction band and VB for valence band.

band edges and are moved to the electrodes by the electric field gradient resulting in a photocurrent. In comparison, when the laser beam is positioned over the contacts (like the situation depicted on the left side of Fig. 5.7(b)), due to the presence of a Schottky barrier, a separation of the charge carriers results leading to the generation of an offset photovoltage denoted by V_{sb}, in addition to the photogenerated current. This is shown by the I-V curves on the right side of Fig. 5.7(b).

To elucidate this model using experiments on real samples, the mode of recording PET images was slightly modified. The PET image of Fig. 5.6 was obtained by recording

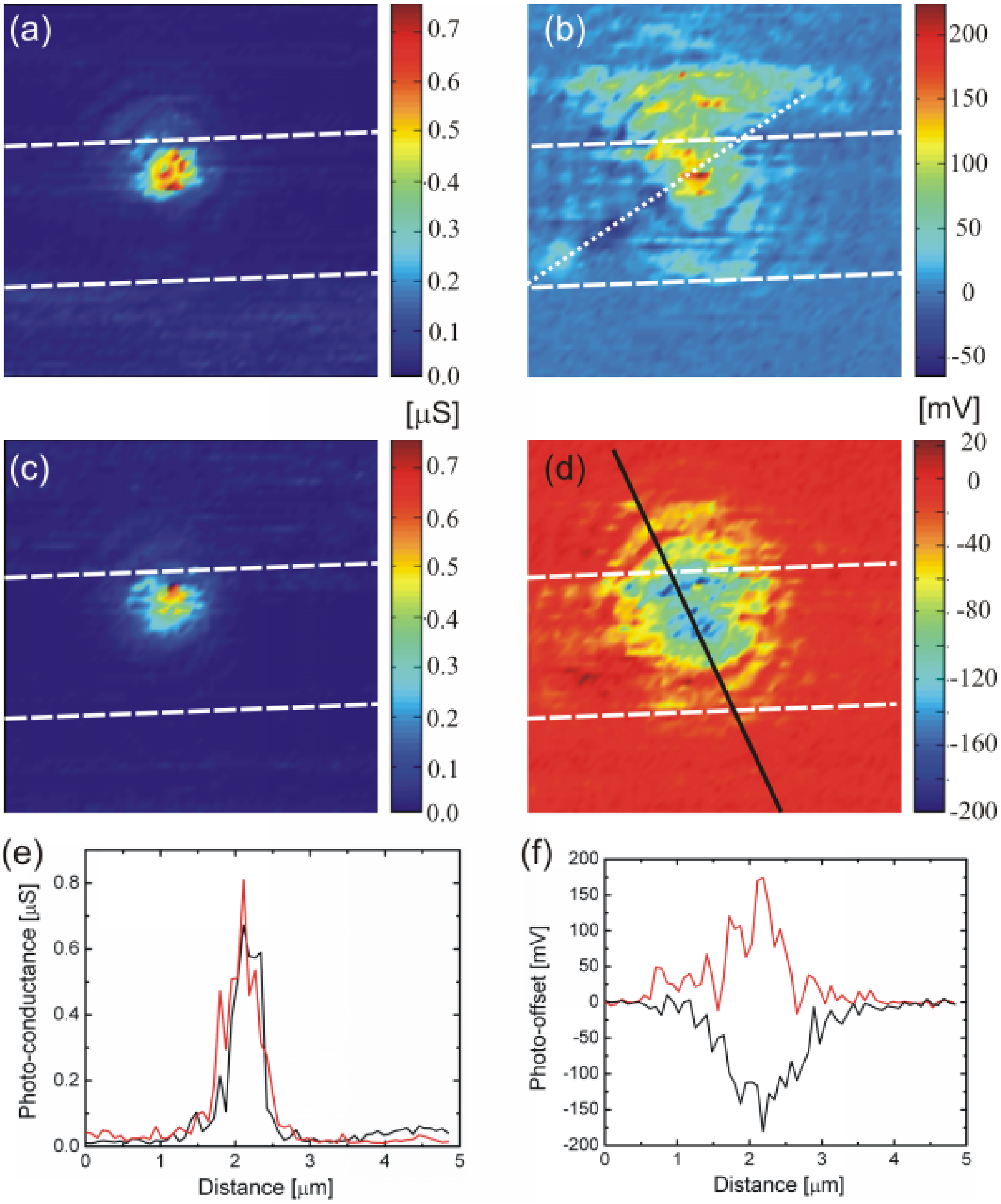

Figure 5.8: (a) Photo-conductance image of an arc-discharge (Carbolex) s-SWCNT contacted by AuPd/Ti electrodes obtained at $\lambda_{\text{exc}} = 514.5$ nm (1 MW/cm^2) in a V_{ds} range of ±50 mV. The electrodes are denoted by white broken lines. (b) Photo-offset image of the same SWCNT under the same conditions as in (a). (c) Photo-conductance and (d) Photo-offset images of the same s-SWCNT with the same parameters except that the source and drain contacts are interchanged. The photo-conductance image and the photo-offset images are obtained by measuring complete I-V curves at every point of photoillumination followed by computing a linear fit and the X-intercept (intercept on the V_{ds} axis) respectively. Photo-conductance (e) and Photo-offset (f) line profiles along the solid black line marked in (d). The red curves correspond to line profiles from (a) and (b), while the black curves correspond to those from (c) and (d). The dotted line in (b) signifies approximately the contacted s-SWCNT.

the current I_d as a function of the position of the laser spot at a fixed drain-source bias of 0.1 V. Under these circumstances, the lobe seen in the PET image close to the top electrode contains the contribution of both the photocurrent and the photo-offset. In the present experiments, using the Leica microscope the acquisition of PET images was made in such a way that complete I-V curves could be measured at every point during the scan of the sample below the laser spot. As a consequence of this, the linear fit of the I-V curves (corresponding to resistance or conductance) and the X-intercept (intercept on the V_ds axis) of I-V curves (corresponding to an offset voltage) could be calculated at every point. This resulted in two PET images – one of them a photo-resistance or photo-conductance image and the other a photo-offset voltage image. The result of such a measurement is summarized in Fig. 5.8. Figs. 5.8(a) and (b) show respectively the photo-conductance (log scale) and the photo-offset images of the sample taken using the resonant laser wavelength of 514.5 nm. Figs. 5.8(c) and (d) are corresponding images obtained by exchanging source and drain under the same conditions. The line profiles in the photo-conductance image of Fig. 5.8(e) show clearly that close to one of the contacts, there is a increase in conductance by around one order of magnitude upon photoillumination. This corresponds to the contribution purely due to photoconductivity in this s-SWCNT. The line profiles along the photo-offset images shown in Fig. 5.8(f) display an offset voltage in the same region close to the electrodes. The change in sign of the photovoltage upon exchange of source and drain leads gives additional support for the creation of a photo-offset voltage across the Schottky barrier. The experimental results presented in Fig. 5.8 are in good agreement with the model outlined in Fig. 5.7.

Although the model explains the creation of photo-offset voltages at the Schottky barriers and the generation of photoconductivity, it does not directly explain the observation of a PETI lobe close to only one of the electrodes in all of the 12 tubes for the contact configuration investigated here. This could be due to a variety of reasons. The SWCNTs obtained from the arc-discharge process are normally coated with a substantial amount of amorphous carbon and are rather inhomogeneous, especially over lengths more than 1 μm. One possibility could be the tube being composed of two different segments of different electrical character, for instance a s-SWCNT connected to a m-SWCNT through a defect site. Another possibility is the creation of asymmetric contacts to the same s-SWCNT as has also been observed in other experiments [107, 108]. In such a configuration, the Schottky barrier on one of the contacts could obscure the effect of the Schottky barrier at the other end, due to a large difference in the barrier heights at the two contacts.

5.4 Photoelectronic transport in metallic SWCNTs

m-SWCNTs represent attractive building blocks for ultra-small electronic devices, such as nanoscale interconnects of high current carrying capability [109]. However, the successful fabrication of such devices still requires a deeper understanding of the local electronic properties of m-SWCNTs and their connection to leads. Various methods have been demonstrated that utilize a probe with dimensions of a few tens of nm to obtain molecular scale electronic structure information along electrically contacted tubes. While resonant electron scattering at defect sites could be observed in m-SWCNTs by varying the local Fermi level through the voltage applied to the AFM tip [86], conducting tip AFM (CT-AFM) proved useful to infer the presence of asymmetric electrical contacts to the same individual SWCNT bundle [107]. In addition, potential variations along a m-SWCNT could be imaged through an electrostatic AFM (EFM) indicating clearly that the voltage drop along the tube occurs precisely at an intrinsic or intentionally introduced defect site [110, 111]. Thus the contacts of the m-SWCNTs to the leads and structural inhomogeneities along them seem to have a strong effect on the electronic transport. In this work, photo-excitation has been used as a probe to gather electronic structure information at a local scale along individual m-SWCNTs. Unlike s-SWCNTs the photoelectronic transport through m-SWCNTs was found to be rather independent of whether AuPd or AuPd/Ti was used as the metal contact. The samples were fabricated using either arc-discharge (Carbolex) or HiPco tubes contacted by electrodes in the 1.3 μm gap architecture. The experiments were performed on a total of 15 m-SWCNTs by obtaining PET images. The images were acquired by recording the drain current (I_d) at zero drain-source bias ($V_\text{ds} = 0$ V), unless otherwise mentioned.

5.4.1 Schottky barriers in m-SWCNT devices

For the results presented here, m-SWCNTs with almost no variation of gate dependence of conductance were used. These samples displayed a GDR less than two (referred to as type I) Fig. 5.9(a) displays the AFM image of a representative sample (HiPco) of type I, comprising an apparently homogeneous nanotube with no discernible structural defect. At high drain-source bias, the dark current through the tube was found to saturate at 25 μA, in accordance with previous observations on individual m-SWCNTs of high structural integrity [112]. Fig. 5.9(b) displays the PET image obtained at zero-bias for this sample. Two oppositely signed lobes can be clearly identified at the contacts, as can also be inferred from the line profiles of the PET image shown in Fig. 5.9(c). To gain more insight into the origin of the two lobes, the source and drain electrodes were

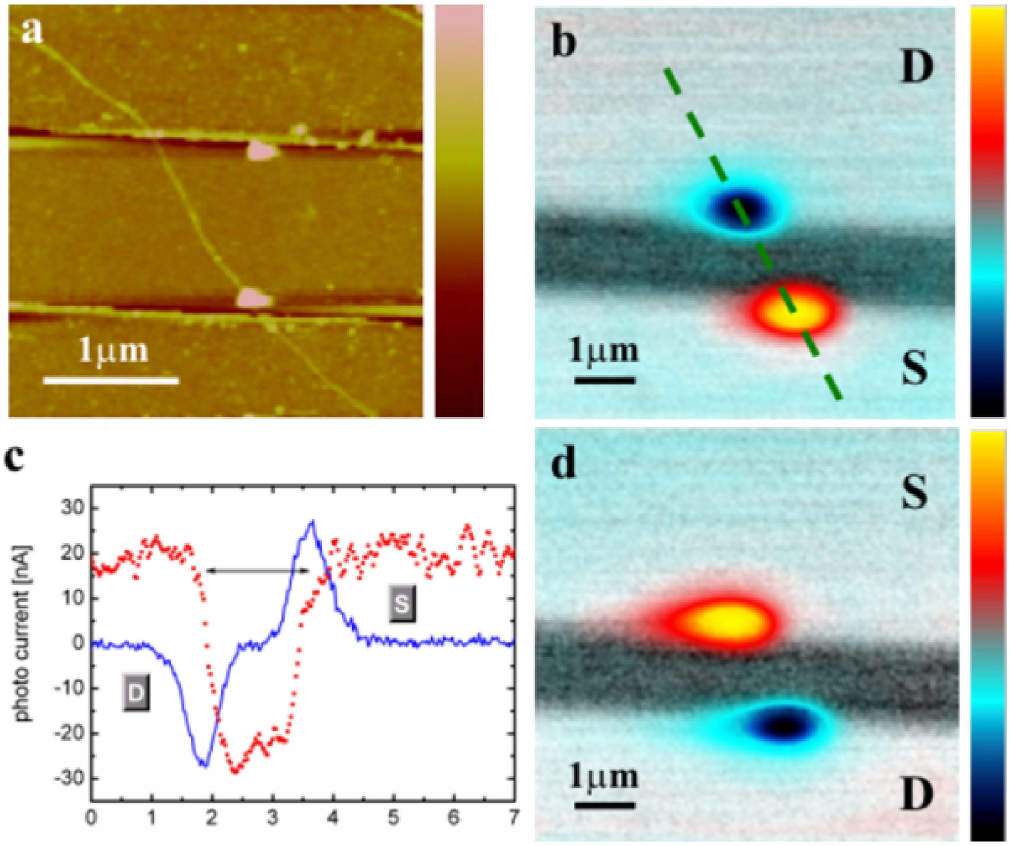

Figure 5.9: Photoelectronic transport (PET) imaging of an individual m-SWCNT: (a) An AFM topograph of the sample with a single HiPco m-SWCNT. The diameter of the tube is ≈ 1.3 nm and its resistance at room temperature in dark is 22 kΩ (conductance ≈ e^2/h). (b) PET image of the same sample obtained by recording the drain current at zero bias overlayed over a simultaneously taken reflection image. (S – source, D – drain, λ_{exc} = 514.5 nm, 50X objective, 0.5 MW/cm^2). (c) The blue solid line and the red dotted line show respectively the line profiles of the photocurrent and the reflection signal along the green line marked in (b). The solid black line with arrows marks the gap region between the electrodes. (d) PET image of the same sample with all parameters identical to that of (b) except that the source and drain electrodes are interchanged. The colorbars show a range of 0 to 25 nm for the AFM image and −27 to 27 nA for the PET images.

interchanged and a PET image was taken with the same parameters. As can be seen from Fig. 5.9(d), the sign of the photocurrent in both lobes has now interchanged. Similar results were obtained on this sample with the red line (λ_{exc} = 647.1 nm, 0.5 MW/cm^2), although in this case the photocurrent was smaller. It is worth mentioning here that the rather instantaneous change in the current and the behavior of the lobes were independent of the environment (ambient or argon or oxygen or water vapor) in which they were measured.

Fig. 5.10 displays the low-bias I-V curves measured while shining laser light at the positions of the two lobes. It is evident from here that the generated short-circuit current originates from an offset voltage. Accounting for the resistance of the tube,

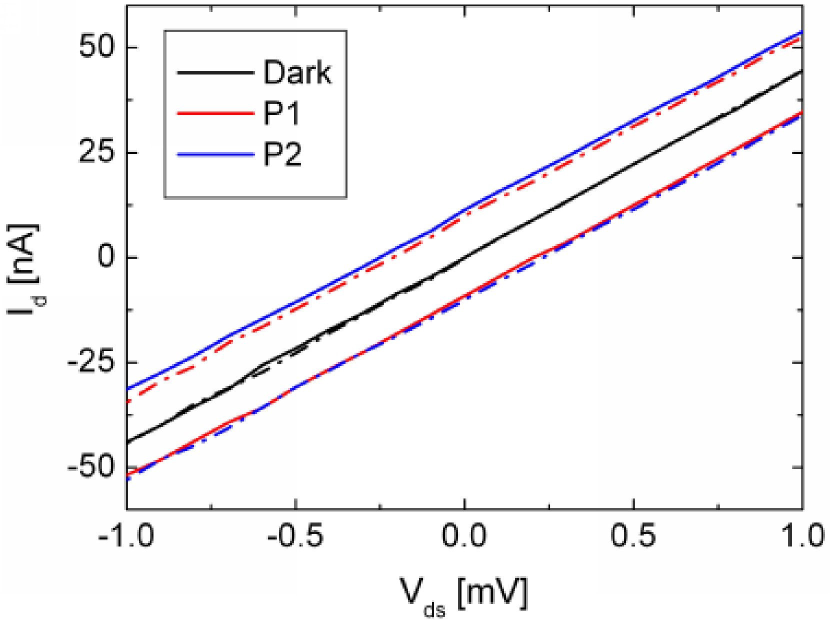

Figure 5.10: Low-bias I-V curves obtained without illumination (black lines), with the laser spot positioned at the top lobe (P1, red lines) and with the laser spot at the bottom lobe (P2, blue line) of the PET image shown in Fig. 5.9. The solid lines are obtained with the top electrode being drain and the bottom electrode being source. The broken lines are obtained upon exchanging source and drain. (λ_{exc} = 647.1 nm, 10X objective, 0.5 MW/cm^2).

the associated photo-offset voltage is calculated to be ≈ 0.2 mV, from the shift of the linear curves. The sign of this offset is found to be opposite for the two lobes, in accordance with the results displayed in Fig. 5.9. In comparison, the photo-offset voltage of ≈ 0.2 mV generated in this m-SWCNT is three orders of magnitude smaller than that observed in s-SWCNTs (≈ 0.2 V).

We interpret the substantial photocurrents generated at the metal contacts to result from local energy barriers introduced when the tube comes in contact with the metal electrode. The nanotube in Fig. 5.9 has a conductance of ≈ e^2/h at room temperature, considerably lower than the value of 4e^2/h expected for ballistic transport through an ideally contacted m-SWCNT with two non-degenerate conductance channels [80]. This difference can be ascribed to the combined effect of scattering by acoustic phonons [83] and reflections by potential barriers at the tube/metal contacts [84]. The importance of the latter is apparent from the fact that the resistance of the tube increased upon cooling the tube to 2K, with the sample exhibiting a suppression of conductance near $V_{\text{ds}} = 0$ and a temperature dependent zero-bias anomaly [85]. In principle, the reduction in conductance from the ideal value could also be partially due to defects along the nanotube. However, a substantial gate dependence of conductance would then be expected [86], which was not observed for this sample. This leads us to conclude that for the present nanotube, the barriers at the contacts restrict the charge transport. Although metallic SWCNTs with nearly perfect contacts have been demonstrated using pure palladium [77], nanotubes contacted with other metals generally exhibit signatures of contact barriers [77, 84, 113]. This barrier formation can be ascribed to band bending as a result of charge transfer due to the equilibration of Fermi levels when the nanotube and the metal electrode are brought in contact [114, 115]. Added to this, the 1D/3D-characteristic of this contact region [85], which differs from a simple 3D/3D-metal interface results in the creation of built-in fields, and the contact region behaves like a Schottky barrier. Based on these arguments, the photo-voltage generation at the metallic nanotube/AuPd interface can be understood to originate from electron/hole-pairs locally created by photo-excitation, followed by the separation of electrons and holes due to the local built-in electric field. In this process, the interband transition between the first van Hove singularities in the m-SWCNT (E_{11}^{m}) provides the necessary absorption cross-section. This is consistent with the observation that the metallic HiPCO tubes showed larger photocurrent signals when illuminated at 514.5 nm than at 647.1 nm under otherwise identical conditions, in accordance with previous reports of stronger optical absorption for the HiPCO tubes at 514.5 nm [116, 117].

When the nanotube is brought in contact with the metal electrode, the internal electric field generated due to charge transfer is directed towards the metal electrode. Seen from the source lead, the electric field at the source contact is oriented opposite to that of the electric field at the drain contact. As a consequence of this, the generated photocurrents are in opposing directions at the two contacts, which explains the opposite signs of the two lobes in the PET image (Fig. 5.9(b)). In all of the measured samples, the photocurrent is negative at the drain electrode (the electron flow is from source to drain), which indicates that the nanotube electronic bands experience an upward bending at the contacts, in agreement with the fact that the work function of the nanotube is smaller than that of AuPd [115]. The identical magnitude of the photocurrents generated at the two contacts of the sample in figure 1 implies the presence of symmetric contact barriers. Some samples, however, displayed considerably different magnitudes of the peak photocurrent at the two electrodes. This finding indicates the formation of asymmetric contacts, similar to observations made on semiconducting nanotubes [107, 108]. With respect to the spatial extent of the barrier region, the fact that the lobes appear slightly elongated only in the scanning direction, but not in the direction along the tube axis, suggests a value of the order of a few nm for the depletion length, far below the resolution of the confocal microscope (≈ 250 nm) [118, 119].

5.4.2 Structural inhomogeneities in m-SWCNTs

m-SWCNT samples of type II exhibited conductances much lower than e^2/h and exhibited GDRs in the range of 3 to 10. Representative of such samples, Fig. 5.11 compares PET images taken on another metallic tube (AFM image in Fig. 5.11(a)) with the 10X and 50X objectives at $\lambda_{exc} = 647.1$ nm. Whereas the 10X magnification image (Fig. 5.11(b)) shows only two lobes at the edges of the electrodes, two additional lobes can be seen in the 50X magnification PET image (Fig. 5.11(c)). In comparison, type I samples such as the one depicted in Fig. 5.9 still display only the two lobes at the contacts even under higher magnification. For the specific case of the nanotube in Fig. 5.11, the series of lobes between the two electrodes shows a pattern of alternating signs. Analogous to the generation of two oppositely signed lobes 1 and 4 at the contacts, the observation of lobes 2 and 3 can be understood to originate from the presence of built-in electric fields in opposing directions at these locations. A plausible assumption is that this tube is composed of a semiconducting segment connecting two metallic segments via defects such as pentagon-heptagon pairs [31, 120]. The two metal-semiconducting junctions would behave like Schottky barriers responsible for the creation of the lobes 2 and 3. Evidence for the existence of segments of varying chirality along individual SWCNTs has recently been gained by Raman spectroscopy [121]. The presence of such structural inhomogeneities along this tube is further solidified by the fact that the tube exhibited a room-temperature conductance much less than e^2/h and a sizeable gate dependence of conductance [86]. Moreover, a closer look at the AFM image (Fig. 5.11(a)) indeed reveals kinks in the nanotube between positions 2 and 3 as

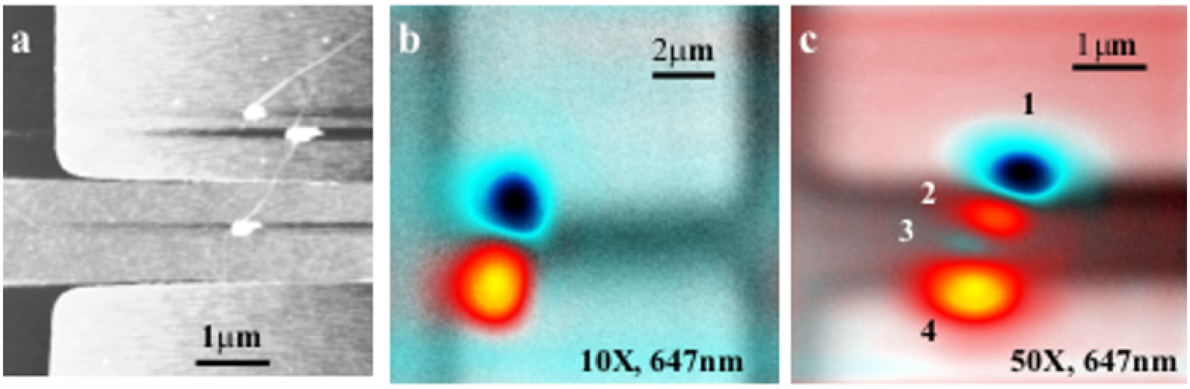

Figure 5.11: PET imaging of a defective m-SWCNT: (a) AFM image of the sample. The diameter of the tube is 0.9 nm close to the lower electrode and 3 nm close to the upper electrode. PET images obtained with a 10X objective at 647.1 nm (b), 50X objective at 647.1 nm (c). Additional lobes in the gap between the electrodes can be identified. The upper lobe 2 can be understood as being created due to the bundle, while the lower weaker lobe 3 can be correlated with the kink in the AFM image.

a possible signature of the two defects. Another noteworthy aspect observable in the AFM image of Fig. 5.11 is the feature in the middle of the contacted tube, which is most likely a catalyst particle, commonly observed in the SWCNT material used in the experiments. From PET images obtained from other samples that show no correlation between the positions of the lobes and the presence of such catalyst particles, it can be excluded that these particles are responsible for the lobes in the PET images.

A simulation of the measured PET images could further corroborate the presence of two localized defect sites. The generation of the PET image was modeled as a linear interaction of the incident laser beam with photoresponsive sites along the tube. Incident beam patterns were generated separately for the 10X and 50X objectives [122]. The photoresponsive sites for the tube in figure 3 were taken to be the center of the lobes 1 to 4. The photo-electronic response is then obtained by a convolution of the beam pattern with each of these point-like photoresponsive sites. Varying interaction strengths were associated with these sites based on their nature as being either a contact site or a defect site. Strong photoresponsive sites 1 and 4 were assigned an equal magnitude of 1 with opposing signs, while comparatively weaker sites 2 and 3 were given a magnitude less than one in addition to having opposite signs. The result of such a simulation is shown in Fig. 5.12. A striking similarity between the simulated and measured PET images is apparent. In particular, the extra lobes visible through the 50X objective have disappeared in the images obtained using the 10X objective. It is worth mentioning that other SWCNTs showed between one and three extra lobes, revealing a variety of patterns with respect to the sign of the photocurrent signal. Further systematic studies on the origin of these presumably defect-induced lobes are under progress.

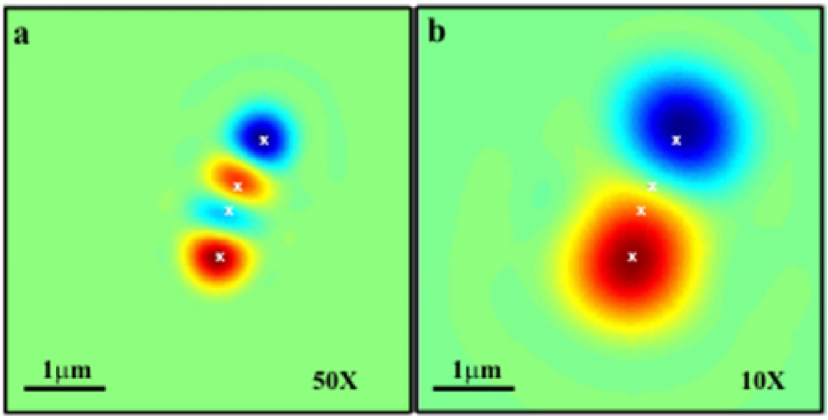

Figure 5.12: Simulated PET images for the sample of Fig.5.11, assuming point-like photoresponsive sites (refer text) at the center of the four lobes 1 to 4, using 50X (a) and 10X (b) objectives. The assumed positions of the sites are overlayed over the images as four crosses. The colormap is the same as that used in Fig.5.11 with an arbitrary range.

5.5 Outlook

The PET measurements on s-SWCNTs have shown that the type of metal used for the contacts and the nature of SWCNT raw material have a strong influence on the electronic transport through SWCNTs. To deepen the understanding of photoelectronic transport in individual s-SWCNTs, nanotubes that retain the same chirality over long distances are essential. On the other hand, the effect of intentionally introduced defect sites on the photoelectronic transport can be followed in a systematic manner. PET imaging could be employed to deliver information about the characteristics of the Schottky barrier formed when s-SWCNTs are contacted by various metals. In the case of m-SWCNTs, an unambiguous association of the lobes in between the electrodes with structural inhomogeneities along the tube requires the use of supplementary techniques such as low-temperature transport measurements and conducting tip AFM. Electrode spacings larger than 1.3 μm may also be explored. Furthermore, the dependence of the intensity of the PETI lobes on the polarization of the incident light needs to be investigated for m-SWCNTs.

The PET imaging technique could be used as a powerful characterization tool to detect the current carrying tubes in an ensemble of connected nanotubes as shown in Fig. 5.13. The PET image in Fig. 5.13(b) displays three sets of lobes of varying intensities corresponding to three different transport channels in the network. More investigations on the exact relation between the type of tube involved in the transport channels and the strength of the lobes are a subject of future work. This would be useful among other aspects in the study of the effect of controlled modification on only one type of tubes in an ensemble. As described in Chapter 4, electrochemical modification has been developed

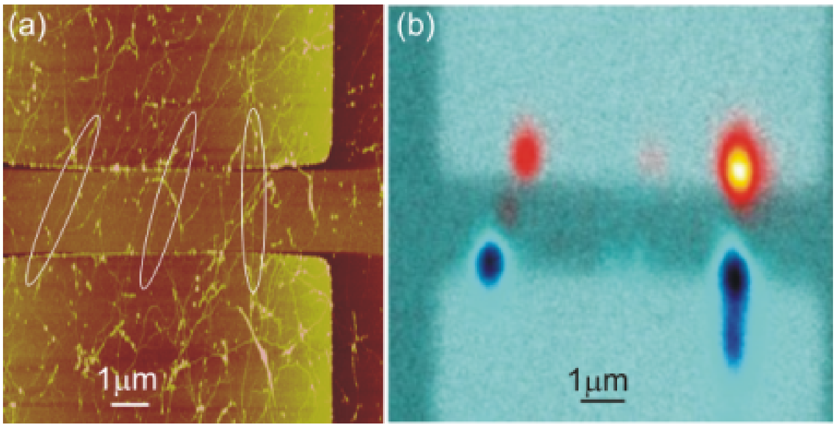

Figure 5.13: Photoelectronic transport imaging of nanotube networks: (a) AFM image of a sample with a network of SWCNTs contacted by electrodes (b) PET image of the sample showing the current carrying tubes in the ensemble.

into a versatile tool for the attachment of desired functional groups onto individual SWCNTs in a covalent or non-covalent manner. The effect of such a modification on the electronic transport could be studied at a local scale with photoillumination as the probe. Obtaining PET images on such modified samples can be expected to deliver useful information about the electronic structure of the modified nanotubes. Moreover, the use of the confocal laser microscope in combination with electronic transport measurements opens up the possibility to perform local photochemistry and photoelectrochemistry on individual SWCNTs, by simultaneously monitoring *in situ* the electronic transport through them. Taken together, the understanding gained from these experiments will have important implications for the fabrication of future optoelectronic and photovoltaic devices.

Chapter 6

Summary and Conclusion

In this thesis, electrochemical modification (ECM) and photoelectronic transport properties of individual SWCNTs have been presented. While the former has enabled the demonstration of a generic route towards fabrication of field-effect transistors, the latter has delivered important results that strengthen the understanding of electronic transport through individual SWCNTs.

ECM of individual nanotubes has been studied using two different coupling schemes. One method was based on the reduction of a highly reactive diazonium salt leading to covalently attached phenyl groups around the SWCNTs. The second scheme utilized the oxidation of a substituted aromatic amine providing a non-covalent coating onto the SWCNTs. The respective covalent and non-covalent characters of the two coupling schemes have been concluded from a combined electronic transport and confocal Raman spectroscopic study of the coated SWCNTs. This study was performed separately with m-SWCNTs and s-SWCNTs. The diazonium coupling to both the types of SWCNTs resulted in an increase of both the resistance and the relative Raman D-line intensity after ECM, which signifies the formation of chemical bonds between the polymer layer and the carbon framework of the nanotube. By contrast, only minor changes in the confocal Raman spectra were detected after oxidative amine coupling on both m-SWCNTs and s-SWCNTs. For this type of coupling, the electrical resistance of the m-SWCNTs remained unchanged, whereas that of s-SWCNTs showed a moderate increase in resistance. This increase in resistance can be understood by the decreased p-doping level of the s-SWCNTs as a result of the electrons accepted during oxidation of the amine. Both the coupling methods can be used to chemically tailor the surface properties of SWCNTs. While the covalent modification enables the alteration of the electronic properties of the SWCNTs persistently, the SWCNTs modified by the oxidative scheme remain mostly unaltered in their electronic structure.

Incorporating the covalent ECM scheme, a generic fabrication route for SWCNT-FETs, which combines electrochemistry and gate-induced modulation of conductivity was demonstrated. It could be shown that the modification of s-SWCNTs can be enabled or blocked by varying the history of the gate potential scans before performing electrochemistry. In this manner, the m-SWCNTs could be exclusively modified and the conduction through only this kind of tubes in a SWCNT ensemble selectively eliminated, resulting in high–performance FETs. The FETs thus obtained displayed room-temperature transconductances of ≈ 10 S/cm, switching ratios of up to 10^6 and hole mobilities of ≈ 1000 cm^2/Vs.

The results presented in this thesis are of importance for both fundamental studies and applications. The study of electrochemical modification of SWCNTs at a *single–tube level* is the first of its kind and represents an important step towards the understanding of the mechanism of chemical attachment of molecular species onto the nanotubes. The use of ECM towards applications was demonstrated by the fabrication of FETs through selective ECM. Chemical and biological sensors with nanotubes coated to detect specific functionalities seem viable using this method.

The photoelectronic transport properties of individual nanotubes were studied using a confocal scanning optical microscope integrated with a setup for electronic transport measurements. The photoexcitation of the carriers was achieved here by the use of a laser spot that is diffraction-limited in size (with a diameter of approximately half of the excitation wavelength). Individual s-SWCNTs were investigated by recording photoconductivity and Raman spectra on the same electrically contacted s-SWCNTs. It was observed that the magnitude of the photocurrent increased linearly with the laser intensity. The photocurrent was found to be maximum for the light polarization being parallel to the tube axis. The small extent of the laser spot generated by the confocal microscope opened up the possibility to record photocurrent signals originating from illumination at different locations along a contacted SWCNT, giving a photoelectronic transport (PET) image. Using such PET images, significant photovoltage generation close to the nanotube–electrode contact could be illustrated, which was attributed to the presence of Schottky barriers there.

This imaging technique was then further applied to the study of the photoelectronic properties of individual m-SWCNTs. The sizeable photocurrent signals observed at the contacts were associated with the formation of depletion regions resulting from the equilibration of the electrochemical potentials at the contact between m-SWCNTs and metal electrodes. In addition, built–in electric fields at structural inhomogeneities were found to effect a separation of photogenerated carriers leading to the creation of a photooffset voltage at these regions. Taken together, it has been demonstrated that spatially resolved photocurrent mapping represents an excellent tool to study the local electronic structure of contact regions and to trace the presence of structural inhomogeneities such as intermolecular junctions within nanotubes. The understanding gained through the experimens performed in this thesis has strong implications for the realisation of future optoelectornic and photonic devices.

Bibliography

[1] *Carbon Nanotubes – Science and Applications*, (Ed.: M. Meyyappan), CRC Press, Boca Raton, **2004**.

[2] J. Aihara, *J. Phys. Chem.* **1994**, *98*, 9773.

[3] K. Balasubramanian, M. Burghard, *Small* **2005**, *2*, 180.

[4] W.P. Hoffman, W.C. Curley, T. Owens, H.T. Phan, *J. Mater. Sci.* **1991**, *26*, 4545.

[5] R.B. Mathur, J. Mittal, O.P. Bahl, N.K. Sandle, *Carbon* **1994**, *32*, 71.

[6] R. Saito, G. Dresselhaus, M.S. Dresselhaus *Physical Properties of Carbon Nanotubes*, (Imperial College Press: London), **1998**.

[7] R. Martel, T. Shmidt, H.R. Shea, T. Hertel, Ph. Avouris, *Appl. Phys. Lett.* **1998**, *73*, 2447.

[8] S.J. Tans, A.R.M. Verschueren, C. Dekker, *Nature* **1998**, *393*, 49.

[9] Ph. Avouris, J. Appenzeller, R. Martel, S.J. Wind, *Proc. IEEE* **2003**, *91*, 1772.

[10] M.S. Fuhrer, B.M. Kim, T. Dürkop, T. Brintlinger, *Nano Lett.* **2002**, *2*, 755.

[11] A. Javey, J. Guo, Q. Wang, M. Lundstrom, H. Dai, *Nature* **2003**, *424*, 654.

[12] D. Chattopadhyay, I. Galeska, F. Papadimitrakopoulos, *J. Am. Chem. Soc.* **2003**, *125*, 3370.

[13] Z. Chen, X. Du, M-H. Du, C.D. Rancken, H-P. Cheng, A.G. Rinzler, *Nano Lett.* **2003**, *3*, 1245.

[14] R. Krupke, F. Hennrich, H.v. Löhneysen, M.M. Kappes, *Science* **2003**, *301*, 344.

[15] M. Zheng, M, A. Jagota, E.D. Semke, B.A. Diner, R.S. McLean, S.R. Lustig, R.E: Richardson, N.G. Tassi, *Nature Materials* **2003**, *2*, 338.

[16] P.G. Collins, M.S. Arnold, Ph. Avouris, *Science* **2001**, *292*, 706.

[17] C.L. Kane, E.J. Mele, *Phys. Rev. Lett.* **2003**, *90*, 207401.

[18] A. Fujiware *et al.*, *Jpn. J. Appl. Phys.* **2001**, *40*, L1229.

[19] Y. Kamada, N. Naka, N. Nagasawa, Z.M. Li, Z.K. Tang, *Physica B* **2002**, *323*, 239.

[20] Y. Zhang, S. Iijima, *Phys. Rev. Lett.* **1999**, *82*, 3472.

[21] M. Freitag, Y. Martin, J.A. Misewich, R. Martel, Ph. Avouris, *Nano Lett.* **2003**, *3*, 1067.

[22] H.W. Zhu, C.L. Xu, D.H. Wu, B.Q. Wei, R. Vajtai, P.M. Ajayan, *Science* **2002**, *296*, 884.

[23] S. Iijima, *Nature* **1991**, *354*, 56.

[24] S. Iijima, T. Ichihashi, *Nature* **1993**, *363*, 603.

[25] D.S. Bethune, C.H. Kiang, M.S. DeVries, G. Gorman, R. Savoy and R. Beyers, *Nature* **1993**, *363*, 605.

[26] J.W. Mintmire, B.I. Dunlap, C.T. White, *Phys. Rev. Lett.* **1992**, *68*, 631.

[27] J.W. Mintmire, D.H. Robertson, C.T. White, *J. Phys. Chem. Solids* **1993**, *54*, 1835.

[28] R. Saito, M. Fujita, G. Dresselhaus, M.S. Dresselhaus, *Phy. Rev. B* **1992**, *46*, 1804.

[29] N.W. Ashcroft, N.D. Mermin *Solid state physics*, (Saunders College Publishing), **1976**.

[30] R. Saito, G. Dresselhaus, M.S. Dresselhaus, *Phys. Rev. B* **2000**, *61*, 2981.

[31] *Carbon Nanotubes: Synthesis, Structure Properties and Applications*, (Ed.: M.S. Dresselhaus, G. Dresselhaus, Ph. Avouris), Springer Verlag: Berlin, **2001**.

[32] S. Frank, P. Poncharal, Y.L. Wang, W.A. deHeer, *Science* **1998**, *280*, 1744.

[33] P. Petit, C. Mathis, C. Journet, P. Bernier, *Chem. Phys. Lett.* **1999**, *305*, 370. .

[34] M.J. O'Connell *et al.*, *Science* **2002**, *297*, 593.

[35] M.S. Dresselhaus, P.C. Eklund, *Adv. Phys.* **2000**, *49*, 705.

[36] H. Kataura, *et al.*, *Synth. Met.* **1999**, *103*, 2555.

[37] E.V. Basiuk, M. Monroy-Pelaez, I. Puente-Lee, V.A. Basiuk, *Nano Lett.* **2004**, *4*, 863.

[38] K. Mylvaganam, L.C. Zhang, *J. Phys. Chem. B* **2004**, *108*, 5217.

[39] Z.F. Chen, W. Thiel, A. Hirsch, *Chem. Phys. Chem.* **2003**, *4*, 93.

[40] H. Hu, P. Bhowmik, B. Zhao, M.A. Hamon, M.E. Itkis, R.C. Haddon, *Chem. Phys. Lett.* **2001**, *345*, 25.

[41] J. Zhao, H. Park, J. Han, J.P. Lu, *J. Phys. Chem. B* **2004**, *108*, 4227.

[42] R.J. Chen, N.R. Franklin, J. Kong, J. Cao, T.W. Tombler, Y. Zhang, H. Dai, *Appl. Phys. Lett.* **2001**, *79*, 2258.

[43] J. Zhang, H. Zou, Q. Qing, Y. Yang, Q. Li, Z. Liu, X. Guo, Z. Du, *J. Phys. Chem. B* **2003**, *107*, 3712.

[44] E. Katz, I. Willner, *Chem. Phys. Chem.* **2004**, *5*, 1085.

[45] K.A.S. Fernando, Y. Lin, Y.P. Sun, *Langmuir* **2004**, *20*, 4777.

[46] M.A. Hamon, J. Chen, H. Hu, Y.S. Chen, M.E. Itkis, A.M. Rao, P.C. Eklund, R.C. Haddon, *Adv. Mater.* **1999**, *11*, 834.

[47] J. Chen *et al.*, *J. Phys. Chem. B* **2001**, *105*, 2525.

[48] J.L. Bahr, J.M. Tour, *J. Mater. Chem.* **2002**, *12*, 1952.

[49] A. Hirsch, *Angew. Chem. Int. Ed.* **2002**, *41*, 1853.

[50] C.A. Dyke, J.M. Tour, *Chem. Eur. J.* **2004**, *10*, 813.

[51] H.F. Bettinger, *Chem. Phys. Chem.* **2003**, *4*, 1283.

[52] V. Georgakilas, D. Voulgaris, E. Vzquez, M. Prato, D.M. Guldi, A. Kukovecz, H. Kuzmany, *J. Am. Chem. Soc.* **2002**, *124*, 14318.

[53] V.N. Khabashesku, W.E. Billups, J.L. Margrave, *Acc. Chem. Res.* **2002**, *35*, 1087.

[54] J.L. Stevens, A.Y. Huang, H.Q. Peng, L.W. Chiang, V.N. Khabashesku, J.L. Margrave, *Nano Lett.* **2003**, *3*, 331.

[55] K. Balasubramanian *et al.*, *Adv. Mater.* **2003**, *15*, 1515.

[56] J.L. Bahr, J. Yang, D.V. Kosynkin, M.J. Bronikowski, R.E. Smalley, J.M. Tour, *J. Am. Chem. Soc.* **2001**, *123*, 6536.

[57] S. Kooi, U. Schlecht, M. Burghard, K. Kern, *Angew. Chem. Int. Ed.* **2002**, *41*, 1353.

[58] G.Z. Chen, M.S.P. Shaffer, D. Coleby, G. Dixon, W: Yhou, D.J. Fray, A:H. Windle, *Adv. Mater.* **2000**, *12*, 522.

[59] M.J. Moghaddam, S. Taylor, M. Gao, S.M. Huang, L.M. Dai, M.J. McCall, *Nano Lett.* **2004**, *4*, 89.

[60] J.B. Cui, M. Burghard, K. Kern, *Nano Lett.* **2003**, *3*, 613.

[61] S. Banerjee, S.S. Wong, *J. Am. Chem. Soc.* **2004**, *126*, 2073.

[62] T.W. Ebbesen, P.M. Ajayan, *Nature* **1992**, *358*, 220.

[63] C. Journet, P. Bernier, *Appl. Phys. A* **1998**, *67*, 1.

[64] http://www.carbolex.com

[65] http://www.mercorp.com

[66] M. Monthioux, B.W. Smith, B. Burteaux, A. Claye, J.E. Fischer, D.E. Luzzi, *Carbon* **2001**, *39*, 1251.

[67] J. Kong, A.M. Cassell, H.J. Dai, *Chem. Phys. Lett.* **1998**, *292*, 567.

[68] Y. Murakami, Y. Miyauchi, S. Chiashi, S. Maruyama, *Chem. Phys. Lett.* **2003**, *374*, 53.

[69] Y. Li, W. Kim, Y. Zhang, M. Rolandi, D. Wang, H. Dai, *J. Phys. Chem. B* **2001**, *105*, 11424.

[70] J. Kong, C. Zhou, A. Morpurgo, H.T. Soh, C.F. Quate, C. Marcus, H.J. Dai, *Appl. Phys. A* **1999**, *69*, 305.

[71] M.J. Bronikowski, P.A. Willis, D.T. Colbert, K.A. Smith, R.E. Smalley, *J. Vac. Sci. Technol. A* **2001**, *19*, 1800.

[72] Ph. Lambin, A. Loiseau, C. Culot, L.P. Biró, *Carbon* **2002**, *40*, 1635.

[73] M. Ouyang, J-L. Huang, C.M. Lieber, *Annu. Rev. Phys. Chem.* **2002**, *53*, 201.

[74] M. Radosavljevic, M. Freitag, K.V. Thadani, A.T. Johnson, *Nano Lett.* **2002**, *2*, 761.

[75] J.B. Cui, R. Sordan, M. Burghard, K. Kern, *Appl. Phys. Lett.* **2002**, *81*, 3260.

[76] W. Kim, A. Javey, O. Vermesh, Q. Wang, Y. Li, H. Dai, *Nano Lett.* **2003**, *3*, 193.

[77] D. Mann, A. Javey, J. Kong, Q. Wang, H. Dai, *Nano Lett.* **2003**, *3*, 1541.

[78] Y. Imry, R. Landauer, *Rev. Mod. Phys.* **1999**, *71*, S306.

[79] S. Datta *Electronic transport in mesoscopic systems*, (University Press: Cambridge), **1995**.

[80] W. Liang, M. Bockrath, D. Boyovic, J. Haffner, M. Tinkham, H. Park, *Nature* **2001**, *411*, 665.

[81] J. Kong, E. Yenilmez, T.W. Tombler, W. Kim, H. Dai, R. Laughlin, L. Liu, C.S. Jayanthi, S.Y. Wu, *Phys. Rev. Lett.* **2001**, *87*, 106801.

[82] Y. Zhang, H. Dai, *Appl. Phys. Lett.* **2000**, *77*, 2015.

[83] S. Reich, C. Thomsen, J. Maultzsch *Carbon Nanotubes: Basic Concepts and Physical Properties*, (Wiley-VCH: Weinheim), **2004**.

[84] M. Bockrath, D.H. Cohen, P.L. McEuen, N.G. Chopra, A. Zettl, A. Thess, R.E. Smalley, *Science* **1997**, *275*, 1922.

[85] Th. Hunger, B. Lengeler, J. Appenzeller, Phys. Rev. B *2004*, **69**, 195406.

[86] M. Bockrath, W. Liang, D. Bozovic, J.H. Hafner, C.M. Lieber, M. Tinkham, H. Park, *Science* **2001**, *291*, 283.

[87] P.L. McEuen, M.S. Fuhrer, H. Park, *IEEE Trans. Nanotech.* **2002**, *1*, 78.

[88] S. Heinze, J. Tersoff, R. Martel, V. Derycke, J. Appenzeller, Ph. Avouris, *Phys. Rev. Lett.* **2002**, *89*, 106801.

[89] J. Appenzeller, J. Knoch, V. Derycke, R. Martel, S. Wind, Ph. Avouris, *Phys. Rev. Lett.* **2002**, *89*, 126801.

[90] C. Zhou, J. Kong, H. Dai, *Appl. Phys. Lett.* **1999**, *76*, 1597.

[91] R. Martel, V. Derycke, C. Lavoie, J. Appenzeller, K.K. Chan, J. Tersoff, Ph. Avouris, *Phys. Rev. Lett.* **2001**, *87*, 256805.

[92] A.M. Rao, E. Richter, S. Bandow, B. Chase, P.C. Eklund, K.A. Williams, *Science* **1997**, *275*, 187.

[93] *Handbook of Microscopy*, (Ed.: S. Amelinckx), xxx, **1997**.

[94] F. Koberling *Ph.D Dissertation: Fluoreszenzmikroskopische Untersuchungen an einzelnen Halbleiter-Nanokristallen*, (Verlag Dr. Hut: München), **2001**.

[95] C. Jiang *et al.*, *Phys. Rev. B* **2002**, *66*, 161404.

[96] A.J. Downard, *Electroanalysis* **2000**, *12*, 1085.

[97] Y. Cui, Q. Wei, H. Park, C.M. Lieber, *Science* **2001**, *293*, 1289.

[98] Y.Chen *et al.*, *J. Mater. Res.* **1998**, *13*, 2423.

[99] M.S. Strano *et al.*, *Science* **2003**, *301*, 1519.

[100] S.J. Wind, J. Appenzeller, R. Martel, V. Derycke, Ph. Avouris, *Appl. Phys. Lett.* **2002**, *80*, 3817.

[101] S.M. Sze *Physics of Semiconductor Devices*, (Wiley: New York), **1981**.

[102] J. Kong, N.R. Franklin, C. Zhou, M.G. Chapline, S. Peng, K. Cho, H. Dai, *Science* **2000**, *287*, 622.

[103] I.A. Levitsky, W.B. Euler, *Appl. Phys. Lett.* **2003**, *83*, 1857.

[104] P.G. Collins, K. Bradley, M. Ishigami, A. Zettl, *Science* **2000**, *287*, 1801.

[105] S.H. Jhi, S.G. Louie, M.L. Cohen, *Phys. Rev. Lett.* **2000**, *85*, 1710.

[106] J. Zhao, J. Han, J.P. Lu, *Phy. Rev. B* **2002**, *65*, 193401.

[107] M. Freitag, M. Radosavljevic, W. Clauss, A.T. Johnson, *Phys. Rev. B* **2000**, *62*, R2307.

[108] K. Balasubramanian *et al.*, *Appl. Phys. Lett.* **2004**, *84*, 2400.

[109] H. Dai, E.W. Wong, C.M. Lieber, *Science* **1996**, *272*, 523.

[110] D. Bozovic, M. Bockrath, J.H. Hafner, C.M. Lieber, H. Park, M. Tinkham, *Appl. Phys. Lett.* **2001**, *78*, 3693.

[111] A. Bachtold, M.S. Fuhrer, S. Plyasunov, M. Forero, E.H. Anderson, A. Zettl, P.L. Mc Euen, *Phys. Rev. Lett.* **2000**, *84*, 6082.

[112] Z. Yao, C.L. Kane, C. Dekker, *Phys. Rev. Lett.* **2000**, *84*, 2941.

[113] A. Bezryadin, A.R.M. Verschueren, S.J. Tans, C. Dekker, *Phys. Rev. Lett.* **1998**, *80*, 4036.

[114] K. Kong, S. Han, J. Ihm, *Phy. Rev. B* **1999**, *60*, 6074.

[115] Y. Xue, M.A. Ratner, *Phys. Rev. B* **2004**, *69*, 161402.

[116] Y. Miyauchi, S. Chiashi, Y. Murakami, Y. Hayashida, S. Maruyma, *Chem. Phys. Lett.* **2004**, *387*, 198.

[117] N. Zheng, X. Bu, B. Wang, P. Feng, *Science* **2002**, *298*, 2366.

[118] M. Freitag, M. Radosavljevic, Y. Yhou, A.T. Johnson, *Appl. Phys. Lett.* **2001**, *79*, 3326.

[119] F. Leonard, J. Tersoff, *Phys. Rev. Lett.* **1999**, *83*, 5174.

[120] A. Rochefort, Ph. Avouris, *Nano Lett.* **2002**, *2*, 253.

[121] C. Jiang, J. Zhao, H.A. Therese, M. Friedrich, A. Mews, *J. Phys. Chem. B* **2003**, *107*, 8742.

[122] R.W. Ditchburn *Light*, (Dover Publications: New York), **1961**.

Publications

Journal Articles

- K. Balasubramanian, M. Friedrich, C. Jiang, Y. Fan, A. Mews, M. Burghard and K. Kern, Electrical transport and confocal Raman studies of electrochemically modified individual carbon nanotubes, *Adv. Mater.* **2003**, *15(18)*, 1515-1518.
- K. Balasubramanian, M. Friedrich, Y. Fan, U. Wannek, A. Mews, M. Burghard and K. Kern, Photoelectronic transport imaging of individual semiconducting carbon nanotubes, *Appl. Phys. Lett.* **2004**, *84(13)*, 2400-2402.
- K. Balasubramanian, R. Sordan, M. Burghard and K. Kern A selective electrochemical approach to carbon nanotube field-effect transistors, *Nano Lett.* **2004**, *4(5)*, 827-830.
- K. Balasubramanian, M. Scolari, A. Mews, M. Burghard and K. Kern, Photocurrent imaging of charge transport barriers in carbon nanotube devices, *Nano Lett.*, accepted.

Review Articles

- K. Balasubramanian, M. Burghard and K. Kern, Carbon Nanotubes: Electrochemical Modification, *Dekker Encyclopedia of Nanoscience and Nanotechnology* **2004**, 507-517.
- K. Balasubramanian and M. Burghard, Funktionalisierte Kohlenstoff Nanoröhren, *Chemie in unserer Zeit* **2005**, *39*, 16-25.
- K. Balasubramanian and M. Burghard, Chemically functionalized carbon nanotubes, *Small* **2005**, *2*, 180-192.

Curriculum vitae

Name:	Kannan Balasubramanian
Date of Birth:	January 4, 1978
Nationality	Republic of India
1994–1998	“Bachelor of Engineering” studies in Computer Science at Birla Institute of Technology & Science, Pilani, India
1998–2000	“Scientist” at DaimlerChrysler Research Centre India, Bangalore, India
2000–2001	“Diplom der Ingenieurwissenschaften” in Elektrotechnik and “Master of Science” in Electrical Communication Engineeering at the University of Kassel, Germany. MS Thesis: “Non-Linear Inverse Scattering Algorithms applied to 2D Scalar Acoustics, Electromagnetics and Elastodynamics”
Nov. 2001–Nov. 2004	PhD student in the group of Prof. Dr. K. Kern at the Max Planck Institute for Solid State Research, Stuttgart, Germany, PhD thesis: “Electrochemical modification & Photoelectronic properties of carbon nanotubes”

Acknowledgements

I am grateful to *Prof. Klaus Kern* for giving me the opportunity to work on my Ph.D. at the Max-Planck Institute for Solidstate Research, one of the prestigious research institutions in the world and for guiding me through the course of this thesis.

I am indebted to *Dr. Marko Burghard* for streamlining my thoughts to work in the right direction, for instilling in me dedication towards every aspect of work however small it might be and for having supported me both technically and personally.

I am thankful to *(Prof.)Dr. Alf Mews* for a fruitful and friendly collaboration enabling me to use the confocal microscope at his group in Mainz, in addition to being helpful in a variety of scientific aspects.

I sincerely acknowledge *Dr. Roman Sordan* for guiding me in aspects of performing electrical transport measurements, and for an informal and friendly atmosphere in the lab.

I am thankful to *Dr. Ralf Vogelgesang* and *(Dr.) Alpan Bek (Kumpel)* for the successful cooperation within the department in matters concerning lasers and optics. I am especially grateful to the latter for the long optical measurements that we have performed during sleepless nights.

I thank *Dr. Yuwei Fan* and *Dr. Alicia Maroto* for help during preparation of samples.

I acknowledge the help of *Wolfgang Heinz, Frank Schartner, Rafael Chaikevitch* for mechanical setups, sample bonding and for electrical instrumentation.

I am indebted to acknowledge the company of my close friends inside the group *(Dr.) Carlos Manzano, Dr. Roman Sordan, (Dr.) Samuel Sarbach, (Dr.) Alpan Bek, Gero Wittich, Manxi Zhu, Diego Repetto, Magalí Lingenfelder, Dr. Thembela Hillie, Dr. Alicia Maroto, Georgios Katsaros* and *Paola Acosta* …

… and my close friends outside the group *Dr. Esther Barrena, (Dr.) Jorge Serrano, Dr. David Quirion, Alicia Nieto, Dimas Feldermann, Ajo, Vladimir Damljanovic, Ioannis Zegkinoglou, Martin Geisler, Julius Reiss* and *Olga Shakuro* for bringing in *life* during my Ph.D. thesis.

I thank my home-zone friends *Shankar Ram Lakshminarayanan, Joe Titus Balt-*

hazar, Vaidy Ramachandran, S P Ganesh, Abhijit Ghose, Devyanee Paul Chauduri, Bijumon Ramachandran, Chandrasekar Krishnamurthy and *Rajan Prasanna* for providing a homely atmosphere during my life at Stuttgart.

I am thankful to the members in my department *Tilman Assmus, (Dr.) Juan Ignacio Paredes, (Dr.) Ulrich Schlecht, Dr. Alex Bittner, Dr. Lucia Vitali* and *all others* for helping me in one way or the other during my thesis.

I am thankful to the group at Mainz *Matteo Scolari, Uli Wannek* and *Marcel Friedrich* for their assistance during the measurements there.

And last but the most important of all, I am grateful to my beloved wife *Alena* and my *parents*, for being always with me and for taking care of me, no matter what their physical condition and coordinates are.